

NUCLEATION AND PROPAGATION OF FRACTURE IN HETEROGENEOUS MATERIALS

A Dissertation

Presented to the Faculty of the Graduate School

of Cornell University

in Partial Fulfillment of the Requirements for the Degree of

Doctor of Philosophy

by

Gabriele Albertini

May 2021

© 2021 Gabriele Albertini
ALL RIGHTS RESERVED

NUCLEATION AND PROPAGATION OF FRACTURE IN HETEROGENEOUS MATERIALS

Gabriele Albertini, Ph.D.

Cornell University 2021

Failure of materials and interfaces is mediated by the propagation of cracks. They nucleate locally and slowly then, as they exceed a critical size, accelerate and reach speeds approaching the speed of sound of the surrounding material. As they propagate, they dissipate energy within a confined region at the crack tip, which approaches a mathematical singularity. As a result, the initiation and propagation of cracks is a spatial and temporal multiscale phenomenon. The framework of linear elastic fracture mechanics captures many aspects related to the dynamic propagation of cracks in homogeneous media. However, the propagation of a crack within a medium with heterogeneous elastic or fracture properties cannot be addressed theoretically. It is in these complex, heterogeneous cases that numerical simulations and experiments shine. The material heterogeneity introduces additional length scales to the problem, which characterize the geometrical properties or spatial correlation of the heterogeneities. The interaction of these geometrical length scales with fracture mechanics related ones is not well understood, but it could provide crucial insights for the design of new materials and interfaces with unprecedented fracture properties.

This thesis investigates different aspects of crack nucleation and propagation in heterogeneous materials and interfaces, including nucleation of mode II ruptures on interfaces with random local properties, dynamic mode II rupture propagation within elastically

heterogeneous media, and dynamic mode I rupture propagation within a material with periodic heterogeneous fracture energy. In this context, when considering mode II dynamic fracture problems, we are making an analogy to frictional interfaces. In fact, the onset of frictional motion is mediated by crack-like ruptures that nucleate locally and propagate dynamically along the frictional interface.

To investigate the complex interaction between fracture mechanics and geometry related length scales we adopt a combined approach using numerical, theoretical, and experimental methods. The numerical simulations consider a continuum governed by the elastodynamic wave equation and allow for a displacement discontinuity (the rupture) along a predefined interface. Depending on the nature of the heterogeneity, the fracture propagation problem is solved using either the finite-element or the spectral-boundary-integral method. Here, we introduce a novel three-dimensional hybrid method, which combines the two former numerical methods to achieve superior computational performance, while allowing modeling of local complexity and heterogeneity. From the experimental side we use state-of-the-art techniques, including ultra-high-speed photography, digital image correlation, and multi-material additive manufactured polymers.

We show that random local strength results in three different nucleation regimes depending on the ratio of correlation length to critical nucleation size. We show that elastic heterogeneity parallel to the fracture interface promotes transition to intersonic crack propagation in mode II cracks by means of reflected elastic waves. Finally, our experimental results of a crack propagating within a material with heterogeneous fracture energy show that the crack abruptly adjusts its speed as it enters a tougher region and allow us to derive an equation of motion of a crack at a material discontinuity.

BIOGRAPHICAL SKETCH

Gabriele Albertini grew up in Poschiavo, Switzerland. He received his scientific education at École Polytechnique Fédérale de Lausanne (EPFL), where he received a M.Sc. and B.Sc. He then started a Ph.D. in Structural Engineering with minors in Computational Science and Engineering, and Solid Mechanics at Cornell University. He will begin a postdoctoral research position at the John A. Paulson School of Engineering and Applied Sciences at Harvard University. Gabriele is a registered Professional Engineer and member of the Society of Engineering Science (SES).

To Thalia & Archimedes

ACKNOWLEDGEMENTS

I would like to thank my advisor, Professor David S. Kammer, for the support, freedom, criticism, and for transmitting to me his passion for scientific research. Special thanks to Dr. Laurent Ponson and Dr. Mathias Lebihain for introducing me to experimental research. Thanks to Dr. Ilya Svetlizky for making me discover the beauty of dynamic fracture and for its physical intuition. Thanks to Professor Gregory C. McLaskey for welcoming me to his group and instilling curiosity about geophysics and earthquakes. Thanks to Professor Jay Fineberg, Professor Ahmed E. Elbanna and Professor Mircea D. Grigoriu for the unique collaboration opportunities. Thanks also to Chun-Yu Ke for the motivation and fruitful discussions.

I also want to thank my loving parents, for giving me opportunity, encouragement and freedom of choosing my own path. Thanks to Archimedes, my loyal companion through the hardship of home office. A special thank to my wife, Thalia, for the incredible support and patience during these years. This thesis would not have been possible without you.

TABLE OF CONTENTS

Biographical Sketch	iii
Dedication	iv
Acknowledgements	v
Table of Contents	viii
List of Tables	ix
List of Figures	xix
1 Introduction	1
1.1 Context	1
1.2 Challenges	3
1.3 Objectives	5
1.4 Approach	6
1.5 Outline of Chapters	8
2 A three-dimensional hybrid finite element – spectral boundary integral method for modeling earthquakes in complex unbounded domains	11
2.1 Introduction	13
2.2 Method	18
2.2.1 Physical Model	18
2.2.2 Finite Element Method (FEM)	20
2.2.3 Spectral Boundary Integral Method (SBIM)	23
2.2.4 Hybrid FEM-SBIM Method	24
2.3 Benchmark problem TPV3: Earthquake rupture in unbounded homogeneous domain	26
2.3.1 Setup	26
2.3.2 Results	28
2.4 Earthquake rupture with LVFZ: pulse-like behaviour	31
2.4.1 Setup	31
2.4.2 Results	32
2.5 Earthquake rupture in a heterogeneous medium: supershear transition	34
2.5.1 Setup	34
2.5.2 Results	35
2.6 Earthquake rupture with step-over faults	37
2.6.1 Setup	37
2.6.2 Results	38
2.7 Discussion	40
2.8 Conclusion	43

3	Off-fault heterogeneities promote supershear transition of dynamic mode II cracks	44
3.1	Introduction	46
3.2	Methods	50
3.3	Effect of off-fault heterogeneities on supershear transition at low pre-stress	54
3.3.1	Illustrative homogeneous and heterogeneous examples	54
3.3.2	Insights into the wave reflection mechanisms	59
3.3.3	Parameter study $\bar{h}_2 = \infty$: effect of wave reflection at closer boundary of inclusion	68
3.3.4	Parameter study $\bar{h}_2 < \infty$: effects of reflection at further boundary of inclusion	73
3.4	Conclusion	78
	Appendices	81
3.A	Reflected S_{rP} wave: derivation of analytical model	81
4	Stochastic Properties of Static Friction	83
4.1	Introduction	85
4.2	Problem Statement	89
4.2.1	Physical Problem	89
4.2.2	Stochastic Properties of Frictional Interface	92
4.2.3	Random Field Samples Generation	94
4.3	Dynamic Simulations	95
4.3.1	Numerical Model	95
4.3.2	Theory for Nucleation of Local Sliding	98
4.3.3	Results	101
4.4	Analytical Monte Carlo Study	104
4.4.1	Monte Carlo Methodology	104
4.4.2	Monte Carlo Results	107
4.5	Discussion	110
4.5.1	Implications of the Physical Problem	110
4.5.2	Interpretation of Numerical Simulations	114
4.5.3	Interpretation of Monte Carlo Study	118
4.5.4	Implications for Earthquake Nucleation	120
4.6	Conclusion	122
	Appendices	124
4.A	Nucleation Criterion	124
4.B	Simplified Statistical Analysis of the Nucleation Strength	126

5	Effective toughness of heterogeneous materials with rate-dependent fracture energy	129
5.1	Introduction	130
5.2	Method	132
5.3	Results	136
5.4	Discussion and Conclusion	142
	Appendices	144
5.A	Supplemental Material	144
5.B	Experimental results	146
5.C	Dynamic crack propagation	148
5.D	Fracture energy based on dynamic stress intensity factor measurements	150
5.E	Equation of motion of a crack	151
5.F	Trapping and untrapping dynamics	155
5.G	Homogenization of fracture energy	156
5.H	Digital Image Correlation analysis	158
5.I	Williams eigenfunctions expansion	161
5.I.1	Near tip fields for in-plane dynamic cracks	163
6	Conclusion	165
	Bibliography	195

LIST OF TABLES

5.A.1 Description of variables used in the study.	144
---	-----

LIST OF FIGURES

2.1	Schematic representation of the physical problem (a), it's representation using a domain-based method such as FE (b), and using the hybrid method (c). The hybrid method couples a domain-based method with a boundary-based method, through the communication of nodal traction τ^{SBI} , displacement \mathbf{u} , and velocity $\dot{\mathbf{u}}$ at the boundaries of the virtual strip, S^\pm	18
2.2	Setup of benchmark problem TPV3. (a) Earthquake rupture in unbounded domain with nucleation over square region of size $a = 3$ km and fault regions of size $L_1^{rpt} = 30$ km and $L_3^{rpt} = 15$ km. (b) Hybrid setup: FE domain with SBI as elastodynamic boundary condition. . . .	27
2.3	Benchmark problem TPV3 solved using hybrid method (blue lines) and using the SBIM (dashed black lines). (a) Contour of rupture front position each 0.5s. (b) Fault shear stress, σ_{12} , and slip rate, \dot{u}_1 , at three stations A, B, and C with position shown in (a).	28
2.4	Benchmark problem TPV3 solved using hybrid method. Velocity magnitude field, \bar{v} , at $t = 3.4$ s. For better visualization we applied a much thicker virtual strip, <i>i.e.</i> , $L_2 = 10$ km instead of $L_2 = 0.2$ km as applied for simulations shown in Fig. 2.3.	29
2.5	Benchmark problem TPV3 solved with hybrid method – mesh convergence study (a) L_2 error as function of mesh size Δx computed over the entire fault at $t = 3$ s. (b) Absolute error as function of time at station C. . . .	30
2.6	Setup of example earthquake rupture in unbounded domain with LVFZ. (a) Fault plane geometry and nucleation patch are analogous to the previous example but with a larger size: $L_1^{rpt} = 60$ km, $L_3^{rpt} = 30$ km, and $a = 3.2$ km. The fault zone region surrounding the fault is more compliant and presents a thickness of $L_{FZ} = 1.6$ km. (b) Hybrid setup: FE virtual strip with $L_2 = 2$ km and with SBI as elastodynamic boundary condition.	32
2.7	LVFZ setup solved using hybrid method with $\Delta x = 100$ m. (a) Contour of rupture front position each 0.5s. (b) Fault shear stress, σ_{12} , and slip rate, $[[\dot{u}_1]]$ at three stations A, B, and C with position shown in (a). At station C the rupture has split into a slip-pulse followed by a crack-like rupture.	33
2.8	Pulse like rupture induced by LVFZ. (a) Space-time diagram of slip rate $[[\dot{u}_1]]$ along the symmetry axis $x_3 = 0$ km. At $t \approx 5$ s, the rupture splits into a slip-pulse, followed by a crack-like rupture. (b) Slip rate $[[\dot{u}_1]]$ at $t = 8$ s shows the spatial extent of the pulse-like and crack-like rupture.	34

2.9	Off-fault low velocity zone setup solved using hybrid method with $\Delta x = 100$ m. (a) Contour of rupture front position each 0.5s. Widely spaced contour lines represent supershear propagation region. (b) Fault shear stress, σ_{12} , and slip rate, $[\dot{u}_1]$ at three stations A, B, and C with position shown in (a).	36
2.10	Supershear transition induced by off-fault low velocity zone. (a) Space-time diagram of slip rate $[\dot{u}_1]$ along the symmetry axis $x_3 = 0$ km. The rupture transitions to supershear at $x_1 \approx 24$ km. (b) Slip rate at $t = 9.25$ s shows the spatial extent of the supershear rupture, just after the transition has initiated.	36
2.11	Setup of example earthquake rupture in unbounded domain with interacting parallel faults with step-over geometry. (a) Setup geometry. Fault zone regions of rectangular size with $L_1^{rpt} = 40$ km and $L_3^{rpt} = 10$ km, with nucleation over a width $a = 20$ km and the entire seismogenic depth, L_3^{rpt} . To the left of the nucleation patch the extent of the primary fault is $L_1^a = 10$ km. The two fault step-over geometry is characterized by $L_{overlap} = 20$ km and $L_{stepover} = 1$ km, shown in (b). The faults are embedded in a homogeneous elastic medium. (b and c) Hybrid setup: FE domain with SBI as elastodynamic boundary condition. The virtual strip width is $L_2 = 1.4$ km.	38
2.12	Results of example earthquake rupture in unbounded domain with interacting parallel faults with dilational step-over setup and spatial discretization $\Delta x = 100$ m. (a) Rupture front contour lines on primary fault, where nucleation occurs over region -40 km $< x_1 < -20$ km (not shown). (b) Rupture front contour lines on secondary fault. Rupture transitions from primary to secondary fault. (c) Fault shear, σ_{12} , and normal, σ_{22} , stress and slip rate, $[\dot{u}_1]$ at three stations A, B, and C with position on the secondary fault shown in (b).	39
2.13	Performance study of FEM and Hybrid method. (a) Computation time, t , of a FEM time step as function of width of the virtual strip, <i>i.e.</i> , number of elements, N_2 . Scaling of computational time is shown for a range of frictional interface discretizations, $N_1 N_3$. The complexity of the FEM time step is linear in N_2 . (b) Computation time of the FEM time step, t , normalized by N_2 (same data and color-code as in (a)). The computation time of a SBIM time step, when computing the elastodynamic boundary condition for the virtual strip, is equivalent to the computation time for one layer of FEM elements. Both, FEM and SBIM computation times are linear in $N_1 N_3$	41

3.1	Setup used for simulations. Central crack of length $2l$ in infinite elastic medium containing a frictional interface (solid line at $y = 0$) and inclusions characterized by the fault distance h_1 , thickness h_2 and velocity ratio c_s^h/c_s . A uniform shear load τ_0 is applied. Only a quarter of the full domain is modeled by applying appropriate boundary conditions at the two anti-symmetry axis (dashed-dotted lines).	52
3.2	Dynamic mode II crack propagation for $S = 2 > S_{\max}$: space-time diagram of normalized tangential traction at frictional interface $\bar{\tau}$. The fractured zone corresponds to the area where $\bar{\tau} = -1$ (dark blue). (a) Homogeneous reference case. As the seed crack reaches $\bar{x} = 1$ it becomes unstable and accelerates towards c_R . A shear stress peak propagates ahead of the rupture front (indicated by dashed black line). (Inset) Close up on process zone at the propagating front. (b) Heterogeneous reference case: $c_s^h/c_s = 0.7$, $\bar{h}_1 = 4$ and $\bar{h}_2 = 10$. Similar to (a) a shear stress peak propagates ahead of the main rupture. Its amplitude grows quicker than in the homogeneous case and reaches the interface strength at $\bar{x} = 34.9$ (inset). A secondary rupture is nucleated and transition to supershear speed occurs.	55
3.3	Effect of reflected waves on dynamic crack propagation and supershear transition. (a) Shear stress peak $\bar{\tau}_w$ as a function of normalized peak position \bar{x}_w . The homogeneous reference case is shown in gray and the heterogeneous reference case in black. The arrival of the reflected S_{rP} wave (red dot), also shown in (b), causes an increased growth rate of $\bar{\tau}_w$ in the heterogeneous case. A second increase, marked by a discontinuity in the position of the shear stress peak, corresponds to the arrival of the reflected S_{rS} wave (green dot). (b) Schematic representation of reflection and transmission of linear elastic waves of the three simplest paths. Dashed lines represent S-waves and continuous lines P-waves. Opacity illustrates the decreased amplitude of the reflected and transmitted waves. The arrival of reflected P-waves at the interface is not shown since no considerable effect has been observed in present simulations, see (a).	56
3.4	Dynamic mode II crack propagation for $S = 2 > S_{\max}$: normalized strain field $\bar{\varepsilon}_{xy}$ at time snapshots of equal crack lengths for homogeneous reference case (left) and heterogeneous reference case (right) with inclusion: $c_s^h/c_s = 0.7$, $\bar{h}_1 = 4$ and $\bar{h}_2 = 10$. Supershear propagation with S-wave Mach cone (bottom right).	60

3.5	Wave reflection model for a S_{rP} wave. (a) Normalized time and position of reflected wavefront arriving at the frictional interface (3.9). (b) Arrival time and position of reflected wavefronts at the interface (3.9) normalized to fracture-mechanics related length scale l_c . Arrival times are shown (in color) for different inclusion distances \bar{h}_1 . The equation of motion of the shear stress peak (3.6) is depicted as dashed line. Red dots (3.11) indicate position where reflected waves start to affect the growth of the shear stress peak.	63
3.6	Effect of reflected waves at varying $\bar{y} = \pm\bar{h}_1$ on $\bar{\tau}_w$ and comparison with analytical model (3.11) for the position of S_{rP} wave arrival \bar{x}_{PS} . (a) Shear stress peak $\bar{\tau}_w$ as function of normalized position \bar{x}_w . Red dots indicate position where heterogeneous setup diverges from homogeneous reference case (gray). Divergence is defined as a relative 0.01% difference in peak stress value. Green dots indicate position of shear stress peak jump due to S_{rS} wave arrival. Transition to supershear $\bar{\tau}_w = S = 2.0$ is indicated by yellow dots. (b) Measured \bar{x}_{PS} (red dots in Figure 3.6 a) are compared with analytical prediction (3.11) (red dots in Figure 3.5 b) for inclusions with various c_s^h/c_s and $\bar{h}_1 = 3.0 - 6.0$	64
3.7	Effect of reflected waves at varying $\bar{y} = \pm\bar{h}_1$ and varying c_s^h/c_s on the shear stress peak at the fault. The shear stress peak difference to the homogeneous reference case $\bar{\tau}_w^h - \bar{\tau}_w^{\text{ref}}$ is shown with renormalized position $\tilde{x}_w - \tilde{x}_{PS}$. (a) Shear stress peak is shown for various \bar{h}_1 and $c_s^h/c_s = 0.5$. S_{rP} wave arrival is marked by red dot. Growth due to S_{rP} is independent of \bar{h}_1 (for $\bar{h}_1 > 2.0$). Arrival of S_{rS} is depicted by green dots. Yellow dots indicate transition to supershear. (b) Contribution of wave reflection on shear stress peak growth for various c_s^h/c_s and $\bar{h}_1 = 5.0$. Growth due to S_{rP} is, similarly to (a), independent of \bar{h}_1 (for $\bar{h}_1 > 2.0$) and is thus representative for various \bar{h}_1 . Curves are partially transparent beyond the arrival of the S_{rS} wave because growth is not independent on \bar{h}_1 for this part.	67
3.8	Influence of $c_s^h/c_s < 1$ and \bar{h}_1 on \bar{x}_{trans} for $S = 2.0$ and $\bar{h}_2 = \infty$. Each point represents a dynamic simulation with domain size $\bar{x}_{\text{max}} = 32$. (a) \bar{x}_{trans} is shown as a function of \bar{h}_1 . (b) \bar{x}_{trans} (color) is shown as function of c_s^h/c_s and \bar{h}_1 . Blank dots show simulation without supershear transition.	68

3.9	Effect of low-velocity inclusions near the interface with $S = 2.0$, $c_s^h/c_s = 0.8$, $\bar{h}_2 = \infty$ and varying \bar{h}_1 . Reference homogeneous case is shown in gray. (a) $\bar{\tau}_w(\bar{x}_w)$ reveals monotonically increasing $\bar{\tau}_w$ for all \bar{h}_1 . (b) Normalized crack propagation velocity as function of normalized crack length \bar{l} shows decreased velocities for $\bar{h}_1 \leq 1$. Sub-Rayleigh equation of motion for homogeneous reference case is shown as red line.	71
3.10	Influence of $c_s^h/c_s > 1$ and \bar{h}_1 on supershear transition for $S = 2.0$ and $\bar{h}_2 = \infty$. (a) $\bar{x}_{\text{trans}}(\bar{h}_1)$ reveals nonlinear trend. (b) \bar{x}_{trans} (color) is shown in dimensionless parameter space as function of c_s^h/c_s and \bar{h}_1 . Blank dots show simulations without transition. For $\bar{h}_1 < \bar{h}_1^{\text{cr}}$, crack propagation exceeds the Rayleigh wave speed of the bulk but not the one of the inclusion.	72
3.11	Various parameter studies considering $S = 2.0$ and $\bar{h}_2 < \infty$. \bar{x}_{trans} (color) is shown as function of \bar{h}_1 , \bar{h}_2 and c_s^h/c_s . Blank dots show simulations without supershear transition within simulated domain. (a) Parameter study $S = 2.0$, $c_s^h/c_s = 0.6$ with varying \bar{h}_1 and \bar{h}_2 . For a given \bar{h}_1 , \bar{x}_{trans} is constant for $\bar{h}_2 > \bar{h}_2^\infty$ and is equivalent to setups $\bar{h}_2 = \infty$ studied in Section 3.3.2. \bar{x}_{trans} increases as $\bar{h}_2^\infty > \bar{h}_2 > \bar{h}_2^{\text{cr}}$. (b) Parameter study $S = 2.0$, $\bar{h}_1 = 1$ with varying c_s^h/c_s and \bar{h}_2 . Similarly as in (a) \bar{x}_{trans} increases as $\bar{h}_2^{\text{cr}} < \bar{h}_2 < \bar{h}_2^\infty$ and converges to a constant value for $\bar{h}_2 > \bar{h}_2^\infty$. (c) Parameter study $S = 2.0$, $\bar{h}_2 = 6.0$ with varying c_s^h/c_s and \bar{h}_1 . For $c_s^h/c_s \leq 0.7$ results are comparable to the configuration with $\bar{h}_2 = \infty$. For $c_s^h/c_s = 0.8$ they differ from the case $\bar{h}_2 = \infty$ (see Figure 3.8).	76
3.12	Effect of thin inclusion on shear stress peak and crack propagation. (a) $\bar{\tau}_w$ for $c_s^h/c_s = 0.6$ and $\bar{h}_1 = 2.0$. $\bar{\tau}_w$ is decreased due to wave reflection at further boundary of inclusion. (b) Crack propagation velocity c_f as function of crack length \bar{l} . Case on the threshold of supershear transition $\bar{h}_2 = 0.5 \lesssim \bar{h}_2^{\text{cr}}$ features a decrease in propagation velocity at $\bar{l} = 20 - 30$	77

4.2.1	<p>Problem statement. (a) A frictional interface (blue line) of strength $\tau_f(\delta, x)$ embedded within two semi-infinite elastic solids, which are periodic in x with period L and infinite in y. A uniform loading $\tau_0(t)$ is applied. (b) The mean interface frictional traction $\langle \tau \rangle(t)$ increases linearly with time t up to the onset of frictional motion when the stress drops from its critical value τ_{cr} to a kinetic level τ_{kin}. (c) The constitutive relation of the frictional interface is a linear slip-weakening law $\tau_f(\delta)$ with random peak strength $\tau_p(x)$ and constant weakening rate W (see Eq. 4.1). (d) $\tau_p(x)$ is a random field with spatial correlation $C(\xi)$ (inset) and probability density function $f(\tau_p)$ (right).</p>	90
4.2.2	<p>Stochastic properties of the random peak strength field $\tau_p(x)$. (a) The random variable τ_p is generated by applying a nonlinear mapping $F^{-1} \circ \Phi(x)$ (Eq. 4.2) onto the Gaussian random variable z. Two colored dots inked by a line represent a (z, τ_p) pair with equal cumulative density $F(\tau_p) = \Phi(z)$, which is the criterion imposed by the nonlinear mapping. (b) Black line is the normalized input spectral density function $g(k)/g(0)$ (Eq. 4.4). Gray line is the empirical spectral density function of $\tau_p(x)$. k is the truncation frequency and $\lambda = 2\pi/\xi_0$ is the cutoff frequency.</p>	93
4.3.1	<p>Representative numerical simulation of the onset of frictional sliding along an interface with random peak strength. (a) Space-time diagram of slip rate along the interface. Time is normalized by the time of friction onset T. Nucleation occurs at $x/L \approx 0.75$. (b-right) Same space-time diagram as in (a) with larger time span. Nucleation is marked by a black dot at $x/L \approx 0.75$ and $t/T = 1$. (b-left) Evolution of average interface stress $\langle \tau \rangle(t)$ normalized by its maximum value τ_{cr}. This corresponds to Fig. 4.2.1b. (c) Stress state $\tau(x)$ at $t/T = 1$ and random profile of peak strength $\tau_p(x)$ for simulation shown in (a-b). The correlation length is $\xi_0/h_n = 0.25$. The size of the critical nucleation patch h_n is marked by black arrows.</p>	96

4.3.2	Verification of nucleation criterion on numerical simulations. (a) The random profile of $\tau_p(x)$ from simulation shown in Fig. 4.3.1 is depicted by dashed gray line. The nucleation stress $\tau_n(x)$ computed from $\tau_p(x)$ by Eq. 4.9 is shown as solid blue line. The point of nucleation given by Eq. 4.10, <i>i.e.</i> , (x_{cr}, τ_{cr}) , is marked by a black dot. (b) Comparison of critical length from theoretical prediction by Eq. 4.10 τ_{cr}^{pred} as shown in (a) with values measured from numerical simulations τ_{cr}^{sim} as illustrated in Fig. 4.3.1. 20 simulations are computed for each ξ_0/h_n value. (c) Comparison of nucleation location from theoretical prediction x_{cr}^{pred} with simulation result x_{cr}^{sim} for the same 60 simulations as shown in (b). (b-c) Gray line indicates slope of 1.	102
4.4.1	Analytical Monte Carlo study. (a) The random local friction strength $\tau_p(x)$ is generated with different correlation lengths ξ_0 . For visual purposes, the same random seed is used for the 4 cases shown. (b) The corresponding local nucleation strength $\tau_n(x)$ is computed using (Eq. 4.9). The probability densities f of the random fields τ_n , $\min(\tau_n)$ and τ_p are reported on the right of (a) and (b), respectively and computed using $N = 10,000$ samples. $f(\min(\tau_p))$ and $f(\tau_n)$ depend on ξ_0 . (c) Probability density of the global friction strength τ_{cr} . (d) Probability density of the position of the critical nucleation patch x_{cr} . Note that the seed is not fixed anymore for the samples used in (c) and (d).	106
4.4.2	Variation of nucleation strength τ_n (a) and effective friction strength τ_{cr} (b) as function of correlation length ξ_0 . Solid lines are the results from the analytical Monte Carlo study with $N = 10,000$ (same data as Fig. 4.4.1). Data-points for $\xi_0/h_n \rightarrow 0$ are based on analytical considerations and connected to the analytical Monte Carlo results by dashed lines. Diamonds are results from 60 dynamic simulations (same data as Fig. 4.3.2).	109
4.B.1	Numerical evaluation of Eq. 4.24. (a) Correlation function. (b) First eigenfunction of the elastic problem. (c) Normalized variance of the nucleation strength τ_n . (d) Zoom over $\xi_0 < h_n$. Dashed line in (c,d) represents approximation Eq. 4.26 for $\xi_0 \ll h_n$	128

- 5.2.1 (a) Model heterogeneous material made of multi-material 3D-printed polymers in a tapered double cantilever beam geometry with applied forces F . The displacement field $\mathbf{u} = (u_x, u_y)$ is measured in the area within the blue box by digital image correlation. (b) Closeup view shows two different materials in a periodic stripe geometry. The transparent material constitutes the matrix with width w^M and the opaque (darker) areas are obstacles of higher fracture energy $\Gamma^O/\Gamma^M \approx 1.3$ with width w^O . (c) Closeup of crack tip at $l \approx 35\text{mm}$ and $v \approx 50\text{m/s}$. The crack interface is slightly visible running from left to center. A random speckle pattern is applied onto the surface, which is compared to its reference pre-cracked configuration to find \mathbf{u} . (d) Infinitesimal strain $\varepsilon_{yy} = \partial_y u_y$ found by differentiating \mathbf{u} . Approaching the crack tip, ε_{yy} diverges. (e) ε_{yy} assuming the Williams eigenfunctions as basis for \mathbf{u} 133
- 5.3.1 (a,b) Experimental results for three specimens with $\Delta l/l_{\text{sys}} = 0.57$. (a) v undergoes abrupt deceleration ($l = \{30, 40, 50\}\text{mm}$) and acceleration ($l = \{35, 45, 55\}\text{mm}$) when the crack front is trapped and untrapped, respectively, at the interface. (b) Discontinuities in Γ occur at trapping and untrapping with higher values within the obstacle. (c) Trapping: speed prior to entering the obstacle v^M is plotted vs. speed immediately after v^O . When the approaching velocity $v^M < v_c \approx 130\text{ m/s}$ the front arrests. (d) Untrapping: speed after exiting the obstacle v^M is plotted vs. speed immediately before exiting v^O . (c,d) Solid black line is the theoretical model (5.2) with $\pm 10\%$ variation in Γ (dotted lines). 135
- 5.3.2 Experimental results for the same specimens shown in FIG. 5.3.1a&b – with same color-code. Data points represent crack speed and fracture energy at the moment of transition of material property. $\Gamma(v)$ is separated in two distinct clusters corresponding to the matrix and obstacle material. Black dashed lines are the average fracture energy measurements based on 30 heterogeneous and 10 homogeneous samples (see Supplemental Material in Appendix 5.A). Solid black lines are the rate-dependent fracture energy law (Scheibert et al., 2010) for the obstacle $\Gamma^O(v)$ and matrix $\Gamma^M(v)$ materials. The transition from one branch to the other is described by $G^S(l)g(v)$ – the equation of the gray arrows (5.1). 138

5.3.3 Homogenization of fracture energy $\bar{\Gamma}$ vs. average velocity, \bar{v} . (a) $\bar{\Gamma}$ assuming the scale separation condition $\Delta l \ll l_{\text{sys}}$. Blue and red dots represent the state of the crack within the two materials, which are related by (5.2) depicted as a gray arrow. The black dot is the corresponding homogenized state $(\bar{\Gamma}, \bar{v})$ computed using (5.6) and (5.7). By varying G^S one can derive the entire homogenized fracture energy law $\bar{\Gamma}(\bar{v})$ (black solid line in a&b). (b) $\bar{\Gamma}(\bar{v})$, measured experimentally using (5.5), is depicted as colored circles for a range of $\Delta l \approx l_{\text{sys}}$. Colored solid lines are the theoretical solution for $\Delta l \approx l_{\text{sys}}$ derived using (5.5), (5.1) (see Supplemental Material in Appendix 5.A)(theory and experiment colors correspond). (a,b) Dash-dotted line and dashed line are $\Gamma^O(v)$ and $\Gamma^M(v)$ from FIG 5.3.2.	141
5.B.1 Supplemental experimental results to FIG. 2. Measurements of crack length vs. time (a) and corresponding crack speed (b) for the same samples as in FIG. 2 and 3. (c) Fracture energy Γ measured by Integrated Digital Image Correlation vs. crack length. (d) $\Gamma(v)$ with average measurements based on 30 heterogeneous and 10 homogeneous samples as black dashed lines. (a,b,c) Gray areas represent obstacles.	147
5.C.1 Universal functions of dynamic fracture mechanics. (a) Experiments are performed at velocities $v < 0.4c_R$ where the contribution of A_I is small. (b, c) Contribution of $k(v)$ is non-negligible for the considered v .	149
5.D.1 Measured $\Gamma(v)$ for the matrix (a) and obstacle (b) materials. Measurements on homogeneous samples are reported as well as for stripes geometry with different stripe widths. The dashed line is a moving average over an interval $\Delta v = 25$ m/s. The solid line is the fracture energy model (5.12). The dash-dotted line is the simplified fracture energy model (5.13). (c) Comparison of $\Gamma(v)$ of both materials with error-band corresponding to standard deviation.	152
5.F.1 Trapping and untrapping dynamics assumptions and parametric study. The solid black line is identical throughout the subplots and represents the solution used for comparison with experiments with parameters based on the material characterization (see FIG. 5.D.1). (a) Reference model (5.18) vs. simplified model (5.19) – dashed line. Dash dotted line assumes rate independent obstacle material ($\alpha^O = 0$). Dotted line assumes rate independent matrix material ($\alpha^M = 0$). (b, c, d) Parametric study for a wide range of parameter space well beyond the uncertainties of the measurements.	157

5.H.1 Digital Image Correlation results. (a) Displacement field u_y measured using the global approach. (b) u_y using integrated approach. (c) Difference in measured displacement between the two methods. (d) Strain field $\varepsilon_{yy} = \partial_y u_y$ computed from the results of the global approach. (e) ε_{yy} from the integrated approach. (f) Difference in strain between the two methods. (g) Singular component of ε_{yy} from the integrated approach. (h) Difference in strain between the global method and the the singular component from the integrated method. 162

CHAPTER 1
INTRODUCTION

1.1 Context

The failure of materials and interfaces is mediated by the propagation of cracks, which nucleate locally and, when they reach a critical size, accelerate and propagate at speeds approaching the speed of sound of the material. Understanding how cracks nucleate and under which conditions they become unstable and propagate dynamically is of great importance for a number of engineering and geophysical applications.

Fracture is the fundamental mechanism governing the failure of materials. Thus, it plays a critical role in the design and assessment of materials and structures. This is particularly important for civil infrastructure because of the high reliability requirements and high consequences of failure, both in terms of human and economic losses. Additionally, fracture is the fundamental mechanism governing many aspects affecting the durability of infrastructure, such as fatigue, and stress corrosion in steel structures and the propagation of cracks in concrete due to corrosion of reinforcement bars or alkali-silica reaction. This is a particularly pressing issue because most of the civil infrastructure in North America and Europe is reaching the end of its service life. Therefore, there is a need to develop automated damage detection techniques and methodologies for evaluating the residual strength of structures.

Interestingly, the propagation of cracks along interfaces within solids is the fundamental problem governing many geophysical systems such as earthquakes, avalanches, and also the stability of slopes and tunnels. In a more general sense, a new paradigm is emerging which is based on the analogy between a slip front and a mode II crack. This allows the study of frictional interfaces using linear elastic fracture mechanics (LEFM) concepts, where the interface is characterized in terms of local fracture energy and peak strength. This approach is particularly powerful because it allows to apply the well developed formalism of LEFM to study friction. For example it allows to formulate an equation of motion for the rupture front in terms of a crack tip energy balance ([Freund, 1990](#); [Svetlizky et al., 2017](#); [Kammer et al., 2018](#)), as well as studying the nucleation phase by means of linear stability analysis ([Uenishi and Rice, 2003](#)). Most importantly, recent experimental evidence has confirmed the friction-fracture paradigm, and showed that the propagation of dynamic shear cracks along frictional interfaces drives the onset of frictional motion ([Svetlizky and Fineberg, 2014](#); [Svetlizky et al., 2020](#)).

Heterogeneity naturally occurs in virtually any material and along any interface. Many biological materials, such as bone, nacre, and tooth, have intricate micro-structures which are responsible for remarkable macroscopic mechanical properties ([Ritchie, 2011](#); [Jackson A. P. et al., 1988](#)). Recent advances in manufacturing techniques allow the control of material microstructure in minute detail. These technological advances allow for designing new materials with unprecedented properties ([Florijn et al., 2014](#); [Blees et al., 2015](#); [Bertoldi et al., 2010](#); [Silverberg et al., 2014](#); [Siéfert et al., 2019](#); [Yin et al., 2019](#); [Chen and Gu, 2019](#)). However, a framework for designing the material microstructure

to achieve advanced *fracture* properties is still missing and experimental observations, which are key for establishing such theoretical knowledge, are scarce.

1.2 Challenges

A great challenge of fracture mechanics is that it is a spatial and temporal multi-scale problem. The fracture mechanics related length scale is the size of the fracture process zone at the crack tip, where the material breaks/yields. Interestingly, in dynamic fracture this length scale is not constant and shrinks as the crack propagation speed increases (Andrews, 1976; Freund, 1990; Svetlizky and Fineberg, 2014). Another length scale is the critical size, L_c , for a crack in a given loading configuration to become unstable, which emerges from the interplay between fracture and elastic properties, and loading configuration. In the small scale yielding limit, and assuming an infinite medium with homogeneous loading τ_0 , the critical nucleation size L_c can be derived by applying the Griffith criterion

$$L_c \sim \frac{\mu\Gamma}{\tau_0}, \quad (1.1)$$

where μ is the shear modulus, and Γ the fracture energy (Andrews, 1976). In the opposite limit, where the size of the process zone spans the whole region where failure has initiated, L_c becomes independent of loading (Uenishi and Rice, 2003)

$$L_c \sim \frac{\mu}{W}, \quad (1.2)$$

where W is the weakening rate, which, assuming a linear cohesive law, takes the form of $W = 2\Gamma D_c^{-2}$, where D_c is the characteristic length of the fracture process.

The time scales over which the crack nucleates are orders of magnitude larger compared to the time taken by the dynamic fracture to propagate. Nucleation time scales are governed by the quasi-static application of boundary conditions and by the chemical processes governing the onset of material failure, which are typically in the range of seconds to hours in lab conditions. However, the dynamic propagation of a rupture is governed by the speed of elastic waves within the material $c \sim 1000$ m/s and, due to the relatively small size of the specimens ~ 1 m, it happens within a few milliseconds.

The additional challenge is that the dynamic propagation of a crack within a finite sample is a transient phenomenon. While there exist analytical solutions ([Freund, 1990](#); [Broberg, 1999](#)) based on the assumption of a steady-state or self-similar crack propagation, the underlying assumptions are too limited to study the more general problem of fracture within a heterogeneous material. However, numerical simulations provide a tool for addressing such problems. Nevertheless, these analytical solutions are extremely useful and provide an analytical benchmark for simulations.

These challenges map directly onto computational and experimental ones. In experiments there is the need to sample information at extremely high frequencies (MHz) and at the same time to deploy a dense array of sensors to capture the propagating front. From a computational perspective, the spatial multi-scale nature of the problem results in a very large number of degrees of freedom. Note that solving the wave equation requires a regular spatial discretization, which needs to be fine enough to represent the smallest length scale of the problem (often this is the process zone) with sufficient accuracy. The temporal multi-scale and transient nature of the problem result in having to solve a very

large number of time steps. This results in particularly expensive computations (especially for three dimensional problems) that require the application of high-performance scientific computing principles.

1.3 Objectives

The main objective of this thesis is to improve our understanding of crack initiation and propagation in heterogeneous media and specifically the interaction between fracture mechanics related length scales and the length scales of the heterogeneity. We will adopt a combination of numerical and experimental methods to investigate these problems. The focus of this thesis is on the following aspects of fracture of heterogeneous materials and interfaces:

Rupture nucleation and the strength of interfaces: Study the nucleation and subsequent onset of instability on interfaces with random local fracture properties. We aim to link the statistical distribution of the macroscopic strength to the stochastic properties of the local random strength.

Rupture propagation within elastically heterogeneous materials but homogeneous fracture energy: Study the effect of inclusions with contrasting elastic properties (which are parallel to the rupture plane) on the dynamic crack propagation speed and transition to different speed regimes. Assess the effect of wave reflection at the boundaries of the inclusions.

Rupture propagation within materials with heterogeneous fracture energy but homogeneous elastic properties: Study the effect of a discontinuity in fracture energy on a dynamically propagating crack. Derive an equation of motion for a crack as it faces discontinuous fracture energy. Derive a homogenization approach for fracture in periodic heterogeneous materials.

A recurring assumption is that failure is confined within a predefined (planar) interface and we consider an elastodynamic material response. Additionally, we consider processes at the continuum scale and neglect the complexity of the microscopic nature of the failure mechanisms. However, we are interested in the emerging laws that matter at the continuous scale, which often means that we will model the complex fracture process with a single parameter, the fracture energy Γ and, if needed¹, we introduce a characteristic length D_c . Therefore, these problems can be addressed with continuum mechanics and more specifically linear elastic fracture mechanics approaches.

1.4 Approach

As stated in the objectives, we consider a continuum representation of dynamic fracture. The problems of interest require solving the elastodynamic wave equation within the (heterogeneous) material and also to allow for a displacement discontinuity, δ , along a predefined interface. The governing equation for the interface is a phenomenological traction separation law $\tau(\delta)$, which properties can be mapped to the relevant fracture

¹often for numerical regularization purposes

mechanics quantity *i.e.*, the fracture energy $\Gamma = \int_0^{D_c} \tau(\delta) d\delta$. Cases that consider elastic heterogeneity will be modeled using the finite-element method with representation of the displacement discontinuity using the traction-at-split-node method. This is implemented on an open-source scientific finite-element library named Akantu (Richart and Molinari, 2015). However, when homogeneous elastic properties are assumed, an explicit representation of the continuum is not necessary and the problem can be addressed using the spectral-boundary-integral method. In the context of this thesis, we developed an open-source spectral-boundary-integral software named Uguca (Kammer et al., 2021) (<https://gitlab.com/uguca/uguca/>). Note that we neglect effects of case specific boundary conditions and assume crack propagation in unbounded domains. Additionally, we develop a new three-dimensional hybrid method for modeling dynamic fracture in complex unbounded domains, by combining the finite-element and the spectral-boundary-integral methods (Albertini et al., 2021).

From the experimental point of view, we use an ultra high speed camera (0.25 MHz) to capture the dynamic crack propagation which will be analyzed using state-of-the-art digital image correlation techniques. The model heterogeneous material is manufactured with multi-material 3D printed polymers, which allows control of geometry and material properties.

1.5 Outline of Chapters

This thesis is organized as follows. Chapter 2 introduces state-of-the-art numerical methods for modeling dynamic fracture along interfaces: the finite-element method (FEM) with a traction-at-split-node technique for modeling the displacement discontinuity and the spectral boundary integral method (SBIM). Both methods have their advantages and shortcomings. The FEM allows modeling heterogeneity in the bulk, nonlinear material behavior and complex geometry, however it is computationally demanding due to the large number of resulting degrees of freedom. On the other hand, the SBIM solves the elastodynamic wave equation in a semi-analytical form, thus, it has higher accuracy than the FEM and is computationally more efficient. However, the applicability of the SBIM is limited to linear elastic materials and planar fracture planes. Here, we introduce a new three-dimensional hybrid method which couples FEM to SBIM by enforcing continuity of displacement and traction at the virtual interface where the FEM is truncated. Thus, the hybrid method combines the advantages of both methods: computational efficiency and flexibility of modeling complex, heterogeneous materials. Finally, we test the developed hybrid method with a benchmark problem from the Southern California Earthquake Center Dynamic Rupture Validation exercises (<https://strike.scec.org/cvws/>) and show its potential for solving dynamic rupture propagation in media with bulk heterogeneity and with multiple possible failure interfaces.

Chapter 3 investigates the effect of inclusions running parallel to a frictional interface with contrasting elastic properties on the propagation speed of a mode II shear rupture using dynamic FE simulations. It focuses on the transition from sub-Rayleigh to su-

pershear (or intersonic) crack propagation, which is a fundamental problem of dynamic fracture mechanics. Interestingly, very few studies focused on the effect of elastic heterogeneity on dynamic fracture. However, they naturally occur in geophysical systems and in composites. Our results show that the presence of inclusions with contrasting wave propagation speed can lead to supershear transition even in low pre-stress cases, where transition would not occur in an equivalent homogeneous setup.

Chapter 4 investigates the origin of variation in static friction on statistically equivalent interfaces. This is motivated by the unusually high variation of static friction strength observed on experimental systems (Rabinowicz, 1992; Ben-David and Fineberg, 2011). We study nucleation of slip patches (mode II ruptures) on slip-weakening frictional interfaces using a combination of SBIM simulation and linear stability analysis (Uenishi and Rice, 2003). We consider random local strength on the frictional interface, which is defined by specific probability density and correlation functions. When the nucleation patch reaches a critical size, it becomes unstable and propagates dynamically, leading to the onset of macroscopic frictional motion. We derive a semi-analytical Monte Carlo model to study the statistics of the force necessary to nucleate a critical patch, *i.e.*, the macroscopic static friction strength. We study the effect of correlation length on the statistical distribution of the macroscopic strength. We find that low correlation length leads to high macroscopic strength. Conversely, large correlation length leads to low macroscopic strength but higher variability.

Chapter 5 investigates dynamic fracture of heterogeneous materials with similar elastic properties and dissimilar fracture energy using state-of-the-art experimental fracture

mechanics techniques. We study the fundamental problem of a crack propagating through a series of periodic obstacles with higher fracture energy. Our model material is manufactured using multi-material 3D printed polymers, which allows us to precisely control the strength and geometry of the material's microstructure. The apparatus comprises a tapered double cantilever beam specimen, an electromechanical testing machine and an ultra high-speed camera. We measure the crack speed and infer the energy dissipation at the crack tip by means of digital image correlation. Our results reveal that the crack speed undergoes large abrupt acceleration/deceleration as the crack leaves/enters a region with higher toughness. Our results also highlight the fundamental role of rate dependence of fracture energy in defining the equation of motion of the crack as it crosses a fracture energy discontinuity.

Finally, Chapter 6 draws conclusions of the various studies on nucleation and propagation of crack or fractures in heterogeneous materials and addresses the potential of the developed hybrid method to tackle complex problems related to friction and fracture mechanics.

CHAPTER 2

A THREE-DIMENSIONAL HYBRID FINITE ELEMENT – SPECTRAL BOUNDARY INTEGRAL METHOD FOR MODELING EARTHQUAKES IN COMPLEX UNBOUNDED DOMAINS

This chapter is drawn from the following article, currently under review:

Albertini, G., Elbanna, A.E. and Kammer, D.S. (2021), ‘A three-dimensional hybrid finite element – spectral boundary integral method for modeling earthquakes in complex unbounded domains’, [arXiv:2102.08756](https://arxiv.org/abs/2102.08756) [math.NA].

We present a 3D hybrid method which combines the Finite Element Method (FEM) and the Spectral Boundary Integral method (SBIM) to model nonlinear problems in unbounded domains. The flexibility of FEM is used to model the complex, heterogeneous, and nonlinear part – such as the dynamic rupture along a fault with near fault plasticity – and the high accuracy and computational efficiency of SBIM is used to simulate the exterior half spaces perfectly truncating all incident waves. The exact truncation allows us to greatly reduce the domain of spatial discretization compared to a traditional FEM approach, leading to considerable savings in computational cost and memory requirements. The coupling of FEM and SBIM is achieved by the exchange of traction and displacement boundary conditions at the computationally defined boundary. The method is suited to implementation on massively parallel computers. We validate the developed method by means of a benchmark problem. Three more complex examples

with a low velocity fault zone, low velocity off-fault inclusion, and interaction of multiple faults, respectively, demonstrate the capability of the hybrid scheme in solving problems of very large sizes. Finally, we discuss potential applications of the hybrid method for problems in geophysics and engineering.

Keywords: Finite Element Method, Spectral Boundary Integral Method, Hybrid Method, Dynamic Fracture, Earthquake Modeling

2.1 Introduction

Earthquakes are a prime example of complex natural processes with far-from-equilibrium nonlinear dynamics at multiple scales. The lack of quantitative data on timescales capturing multiple large earthquake cycles is a fundamental impediment for progress in the field. Physics-based simulations provide the only path for overcoming the lack of data and elucidating the multi-scale dynamics and spatio-temporal patterns that extend the knowledge beyond sporadic case studies and regional statistical laws.

The multiscale nature of the earthquake phenomena is manifested as follows. Spatially, a moderate-size earthquake typically propagates over tens of kilometres. However, the physical processes governing the rupture propagation operates within a narrow region at the rupture tip, called the process zone, which may not exceed a few millimetres in size if realistic laboratory-based friction parameters are used (Noda *et al.*, 2009). Temporally, an earthquake event, where rapid slip occurs, only lasts for few to tens of seconds. However, the time span between successive large earthquakes may be tens to hundreds of years (Lapusta *et al.*, 2000). Thus, there exists approximately a decade of spatial and temporal scales that must be resolved in a target physics-based simulation of earthquakes and aseismic slip. This necessitates innovation in modeling both the fast dynamic rupture with extreme localization and the slow quasi-static slip, during the interseismic period, that exhibits gradual variations. This is a fundamental challenge in earthquake source physics which has been a focus of computational earthquake mechanics over the past four decades.

Historically, numerical methods for simulating earthquakes and aseismic slip may be classified broadly into two categories: boundary-based methods and domain-based methods. The boundary integral formulation enables reducing the spatial dimension of the problem by one, by invoking the representation theorem of linear elastodynamics, transforming 2D problems into 1D and 3D problems into 2D (Cochard and Madariaga, 1994; Geubelle and Rice, 1995). The spectral formulation of the boundary integral equations has been transformative in seismic applications (e.g. Lapusta et al. (2000) and references therein). For example, Lapusta et al. (2000) derived accurate adaptive time-stepping algorithms and truncation of convolution integrals that enabled, for the first time, the consistent elastodynamic simulation of a long sequence of events combining rapid slip during earthquake ruptures and slow deformation during the interseismic periods. Nonetheless, the method is limited to homogeneous linear elastic bulk. While the method may be applied, in principle, to heterogeneous linear elastic materials, the lack of a closed form representation of the Green's function either inhibits the method from providing a well-defined solution to many problems of interest or makes it less computationally attractive. Furthermore, the superior performance of the spectral approach and its computational efficiency is only possible for planar interfaces. This precludes the representation of non-planar faults or direct incorporation of fault zone complexity (e.g. damage, and shear bands).

On the other hand, numerical methods based on bulk discretization such as the finite difference (FD) and finite element methods have been used in simulating earthquake ruptures since mid-1970s and early 1980s with the pioneering works of Boore et al. (1971), Andrews (1976), Das and Aki (1977), Archuleta and Day (1980), Day (1982),

Virieux and Madariaga (1982), and others. These methods are more flexible than the boundary integral approaches in handling heterogeneities, nonlinearities, and fault geometry complexities (see Fig. 5.2.1a&b). In recent years, highly accurate formulations were introduced, including the spectral finite element (Komatitsch and Tromp, 1999; Ampuero, 2002; Festa and Vilotte, 2006; Ma and Archuleta, 2006; Kaneko et al., 2008), the discontinuous Galerkin method (Käser and Dumbser, 2006; Benjema et al., 2007; Puente et al., 2009; Pelties et al., 2012; Tago et al., 2012), and higher-order FD schemes (Cruz-Atienza et al., 2007; Dalguer and Day, 2007; Kozdon et al., 2013). A main computational challenge of these methods is the need to discretize the whole bulk, which increases the computational demand by at least one order of magnitude compared to the boundary integral formulation. Furthermore, the computational domain must be truncated at a sufficient distance from the fault surface such that it would not affect the physical solution. While domain truncation has been achieved by the introduction of several widely-used absorbing boundary conditions such as boundary viscous damping (Lysmer and Kuhlemeyer, 1969), perfectly matching layers (Berenger and others, 1994), and infinite elements (Bettess, 1977), these methods have limitations. Specifically, in all these methods, artificial reflections exist to varying degrees and the absorbing surfaces must be taken sufficiently far from the fault surface to ensure solution accuracy. Moreover, attempts to perform cycle simulations using these volume-based methods are rare and have been restricted mainly to the quasi-dynamic limit (Erickson and Day, 2016). This is partially due to the high spatial discretization cost and the lack of a systematic approach to handle both dynamic and quasi-dynamic calculations in the same framework which is required for simulating both earthquake ruptures and intersesismic slow defor-

mations. Another challenge in these methods is defining fault loading. Currently, this is done by applying displacement-controlled loading at the far boundaries of the simulation box. This, however, makes the fault stressing rate dependent on where the domain is truncated. This problem is solved approximately in the SBI formulation by loading the fault directly through back-slip.

Both bulk and boundary approaches have their merits and limitations. The limitations are evident in 3D simulations where computational complexity grows like the element size to the fourth power rendering high resolution models a computational bottleneck. To that end, this paper proposes a new hybrid numerical scheme, for the full three dimensional elastodynamic problem, that combines the 3D FE method and the 2D SBI equation method to efficiently model fault zone nonlinearities and heterogeneities with high resolution while capturing large-scale elastodynamic interactions in the bulk. The main idea of the method is to enclose the heterogeneities in a virtual strip that is introduced for computational purposes only (see Fig. 5.2.1c). This strip is discretized using a volume-based numerical method, chosen here to be the finite element method due to its popularity and flexibility in handling complex geometry and arbitrary bulk heterogeneities. The top and the bottom boundaries of the virtual strip are handled using the independent SBI formulation (Geubelle and Rice, 1995) with matching discretization. The coupling between the two methods is achieved through enforcing continuity of displacement and traction at the virtual boundaries. The current work extends recent work by the authors and their groups over the past few years which first developed the hybrid scheme for the 2D dynamic anti-plane problem combining finite difference and spectral boundary integral methods (Hajarolasvadi and Elbanna, 2017), and the 2D

dynamic in-plane problem using the finite element method for bulk discretization in the hybrid scheme (Ma et al., 2019). Prior work has demonstrated the accuracy and computational efficiency of the coupled approach and its potential for modeling dynamic ruptures with high resolution fault zone physics (Ma and Elbanna, 2019) as well as extension to the quasi-dynamic limit and cycle simulations (Abdelmeguid et al., 2019). The current extension to the full three dimensional case represents the culmination of these efforts.

The remainder of this paper is organized as follows. In Section 2.2, we describe the physical model (Section 2.2.1), and the numerical methods to solve it, which includes the finite-element method (Section 2.2.2), the spectral boundary integral method (Section 2.2.3), and their coupling – the hybrid method (Section 2.2.4). In Section 2.3, we validate the hybrid method using the benchmark problem TPV3 (Day et al., 2005) of the Southern California Earthquake Center. Next, we demonstrate the capabilities of the new hybrid method on more complex problems. We consider a low velocity fault zone in Section 2.4, a low velocity inclusion at a distance from the fault in Section 2.5, and interacting faults in Section 2.6. Finally, we discuss the advantages of the hybrid method in terms of computational cost in Section 4.5 and draw conclusions in Section 4.6.

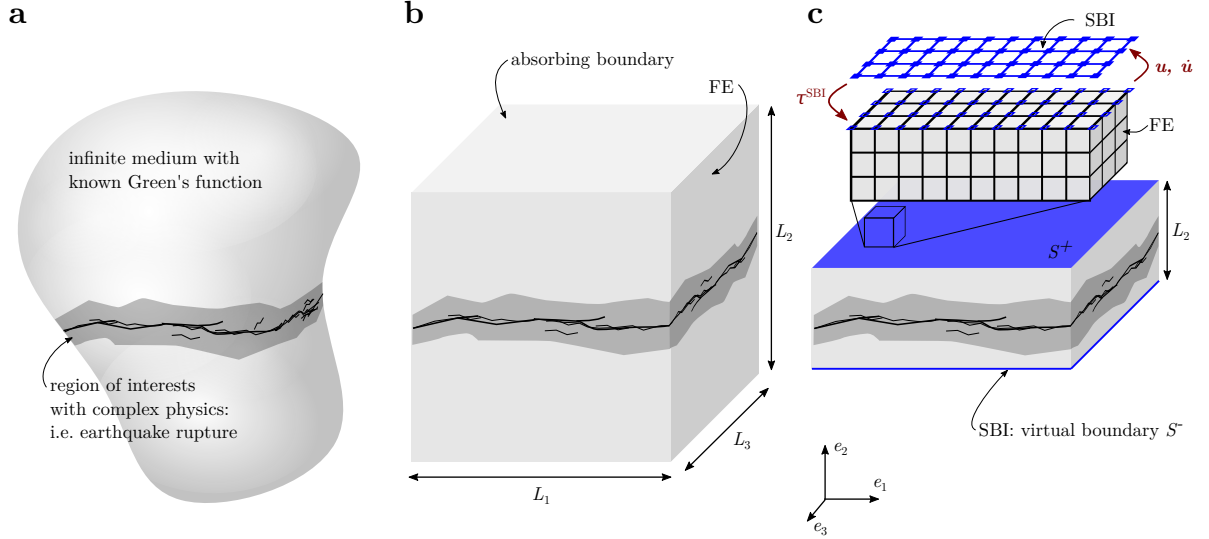


Figure 2.1: Schematic representation of the physical problem (a), its representation using a domain-based method such as FE (b), and using the hybrid method (c). The hybrid method couples a domain-based method with a boundary-based method, through the communication of nodal traction τ^{SBI} , displacement \mathbf{u} , and velocity $\dot{\mathbf{u}}$ at the boundaries of the virtual strip, S^\pm .

2.2 Method

2.2.1 Physical Model

We solve the fully dynamic three-dimensional problem of a rupture propagating along a fault embedded in an elastic solid. The conservation of linear momentum within the elastic domain Ω is given by

$$\rho \ddot{u}_i - \frac{\partial \sigma_{ij}}{\partial x_j} = 0 \quad \text{in } \Omega \quad (2.1)$$

where ρ is the material density, u_i the displacement vector, with the “dot” being the derivative with respect to time t , σ_{ij} the Cauchy stress tensor, and x_j the coordinate

vector. Body forces are neglected. Dirichlet boundary conditions are applied on S_u and Neumann boundary conditions are applied on S_T

$$u_i = \bar{u}_i \quad \text{on } S_u \quad (2.2)$$

$$\sigma_{ij}n_j = \bar{\tau}_i \quad \text{on } S_T, \quad (2.3)$$

where n_i is the normal vector to the surface S_T . Initially, the domain is assumed to be in equilibrium, and, hence, the initial conditions are given by $u_i(0) = u_i^0$ and $\dot{u}_i(0) = 0$.

We assume linear elastic material behavior:

$$\sigma_{ij} = \lambda \delta_{ij} \varepsilon_{kk} + 2\mu \varepsilon_{ij} \quad (2.4)$$

with the infinitesimal strain tensor $\varepsilon_{ij} = (\partial u_i / \partial x_j + \partial u_j / \partial x_i) / 2$ and the Lamé parameters λ, μ describing the elastic properties of the material.

The fault transmits stresses from one half-space to the other through interface tractions. We focus on tangential (friction) interaction and impose non-penetration/non-opening conditions to the normal component of the fault surfaces S_f^\pm . The local slip vector, which corresponds to the tangential fault opening vector, is given by

$$\delta_i = R_{ij}(u_j^+ - u_j^-) \quad \text{on } S_f^\pm, \quad (2.5)$$

where R_{ij} is the global-to-local rotation matrix and $+$ and $-$ indicate the upper and lower fault sides, respectively. Local slip δ is the amplitude of δ_i . The fault is governed by a stick-slip behavior that is described by two states. A sticking section of the fault is described by:

$$\dot{\delta} = 0 \quad \text{and} \quad \tau \leq \tau^s \quad (2.6)$$

where $\dot{\delta}$ is slip rate, τ the amplitude of the fault shear traction vector and τ^s the fault strength. A sliding fault section is described by:

$$\dot{\delta} > 0 \quad \text{and} \quad \tau = \tau^s . \quad (2.7)$$

A constitutive law is applied to model the fault strength evolution. For simplicity, we apply a linear slip-weakening friction law (Ida, 1972), which is given by:

$$\mu(\delta) = \begin{cases} \mu_s - (\mu_s - \mu_k) \delta / \delta_c & \text{for } \delta < \delta_c \\ \mu_k & \text{for } \delta \geq \delta_c \end{cases} \quad (2.8)$$

where μ_s and μ_k are the static and kinetic friction coefficient, respectively, and δ_c is the characteristic slip length to reach residual strength. The fault strength is then given by $\tau^s = \sigma^n \mu(\delta)$, where σ^n is the normal stress. Other friction laws, such as rate-and-state friction (Dieterich, 1979; Ruina, 1983), could also be applied in a similar framework, as shown by Kaneko et al. (2008),

2.2.2 Finite Element Method (FEM)

The finite element method is based on a variational formulation of the governing equation and applies a discretization based on shape functions to find an approximate solution to the physical problem presented in Sec. 2.2.1. A detailed description can be found in standard textbooks (Belytschko et al., 2013). The FEM approach transforms the strong form, *i.e.*, the governing equation (2.1), to the weak form by multiplying it with the test functions $\hat{u}(x)$, integrating it over the domain, and applying Green's identity, which

results in:

$$\int_{\Omega} \rho \ddot{u}_i \hat{u}_i \, d\Omega + \int_{\Omega} \sigma_{ij} \frac{\partial \hat{u}_i}{\partial x_j} \, d\Omega - \int_{S_{\bar{\tau}}} \bar{\tau}_i \hat{u}_i \, dS - \int_{S_f} \tau_i \hat{u}_i \, dS = 0. \quad (2.9)$$

Test functions are chosen smooth enough, such that all steps are well defined and vanish on the Dirichlet boundary. By choosing suitable interpolation functions, $N_I(x_J) = \delta_{IJ}$, and test function $\hat{u}(x) = \sum_I N_I(x) u_I(t)$, where the subscript I represent the node index, $u_I(t)$ becomes the nodal displacements. Using this standard FE approach, the weak form can be expressed as the following matrix equation

$$\mathbf{M}\ddot{\mathbf{u}} + \mathbf{K}\mathbf{u} - \mathbf{f} - \mathbf{B}\boldsymbol{\tau} = \mathbf{0} \quad (2.10)$$

where $\ddot{\mathbf{u}}$ denotes the second time derivative of the displacement vector, \mathbf{M} and \mathbf{K} are the mass and stiffness matrix, respectively, \mathbf{B} is a fault rotation-area matrix, $\boldsymbol{\tau}$ is the fault traction vector, and \mathbf{f} is the force vector from Neumann boundary conditions.

We apply an explicit central-difference time integration formulation with a predictor-corrector formulation. The step-by-step procedure follows:

$$\dot{\mathbf{u}}_{t+1}^{pred} = \dot{\mathbf{u}}_t + \Delta t \ddot{\mathbf{u}}_t \quad (2.11)$$

$$\mathbf{u}_{t+1} = \mathbf{u}_t + \Delta t \dot{\mathbf{u}}_{t+1}^{pred} \quad (2.12)$$

$$\Delta \ddot{\mathbf{u}} = (-\mathbf{K}\mathbf{u}_{t+1} + \mathbf{f} + \mathbf{B}\boldsymbol{\tau}_{t+1}) \mathbf{M}^{-1} - \ddot{\mathbf{u}}_t \quad (2.13)$$

$$\dot{\mathbf{u}}_{t+1} = \dot{\mathbf{u}}_{t+1}^{pred} + \frac{1}{2} \Delta t \Delta \ddot{\mathbf{u}} \quad (2.14)$$

$$t = t + \Delta t \quad (2.15)$$

where the subscript indicates the time step and Δt is the current incremental time step, which is required to satisfy the Courant-Friedrichs-Lewy condition ([Courant et al., 1928](#)).

We apply a lumped mass matrix, which simplifies the computation of the inverse mass matrix and reduces computational cost of the time-integration scheme. The fault rotation matrix is scaled by the fault-surface area associated with each fault-split-node and thus transforms the fault traction vector τ to a nodal force vector.

The fault traction vector τ_{t+1} in Eq. (2.13) is computed by a forward Lagrange multiplier method (Carpenter et al., 1991), which uses a prediction procedure to pre-computes the slip rate for the next time step. A similar approach was applied in spectral-element simulations (Kaneko et al., 2008). We denote a fault discontinuity as $[[A]] = (A_+ - A_-)$ where subscript $+$ and $-$ indicate the upper and lower fault sides, respectively. The predicted slip rate during the next time step if no fault tractions were applied is given by

$$[[\dot{\mathbf{u}}_{t+3/2}]] = [[\dot{\mathbf{u}}_{t+1}^{pred} - \frac{\Delta t}{2}\ddot{\mathbf{u}}_t - \Delta t \mathbf{M}^{-1}(\mathbf{K}\mathbf{u}_{t+1} - \mathbf{f})]]. \quad (2.16)$$

We use the slip-rate predictor $[[\dot{\mathbf{u}}_{t+3/2}]]$ because the no-slip-rate condition $[[\dot{\mathbf{u}}_{t+3/2}]] = 0$ will ensure that the interface remains stuck and hence $[[\mathbf{u}_{t+2}]] = [[\mathbf{u}_{t+1}]]$. Using Eq. (2.16), we can compute the traction required to maintain slip and impose stick condition on the fault by

$$\tilde{\tau}_{t+1} = \frac{1}{2}\mathbf{Z}[[\dot{\mathbf{u}}_{t+3/2}]], \quad (2.17)$$

where \mathbf{Z} is the fault impedance matrix given by $\mathbf{Z}^{-1} = \Delta t (\mathbf{M}_+^{-1}\mathbf{B}_+ + \mathbf{M}_-^{-1}\mathbf{B}_-)/2$ and the following fault traction balance was applied $\tau = -\tau_+ = \tau_-$. The actual fault traction is computed by applying the stick-slip conditions given by Eq. (2.6) and Eq. (2.7):

$$\tau_{t+1} = \begin{cases} \tilde{\tau}_{t+1} & \text{if } \tilde{\tau}_{t+1} \leq \tau_{t+1}^s \quad (\text{stick}) \\ \tau_{t+1}^s & \text{otherwise} \quad (\text{slip}) \end{cases} \quad (2.18)$$

where τ_{t+1} and $\tilde{\tau}_{t+1}$ are individual entries in τ_{t+1} and $\tilde{\tau}_{t+1}$, respectively, and τ_{t+1}^s is the fault strength at each split-node (node indicator is omitted for simplicity) and is governed by Eq. (2.8).

2.2.3 Spectral Boundary Integral Method (SBIM)

Boundary integral methods have the advantage of modeling the wave propagation problem in the entire domain Ω by using an integral relationship (in space and time) between the displacements and the tractions along the boundary of the domain $\partial\Omega$. The advantage lies in reduced computational cost and increased accuracy with respect to a finite-element or finite-difference method. For these reasons, boundary integral methods have been used extensively since the mid-1980s to study crack propagation problems (Das, 1980; Andrews, 1985; Boatwright and Quin, 1986; Das and Kostrov, 1987, 1988; Israil and Banerjee, 1990; Koller et al., 1992; Liu and Rizzo, 1993; Bonnet and Bui, 1993; Cochard and Madariaga, 1994; Andrews, 1994) .

Consider the displacements and tractions at a the boundary of an semi-infinite half space with the boundary lying on the e_1, e_3 plane and the domain being infinite in the e_2 direction. Following the process described in Geubelle and Rice (1995) the elastodynamic response of a 3D elastic half space is given by

$$\tau_i^{\text{SBI}}(x_1, x_3, t) = \tau_i^\infty(x_1, x_3, t) - \eta_{ij} \frac{\mu}{c_s} \dot{u}_j(x_1, x_3, t) + s_i(x_1, x_3, t) , \quad (2.19)$$

where η_{ij} is a diagonal matrix with $\eta_{11} = \eta_{33} = 1$ and $\eta_{22} = c_s/c_p$. c_p and c_s are the longitudinal and shear wave speeds of the material, respectively. Eq. (2.19) states

that the traction at the surface of the half space, τ_i^{SBI} , equals the far field traction, τ_i^∞ , plus a “radiation damping” term, $\eta_{ij} \frac{\mu}{c_s} \dot{u}_j^\pm$, and a spatiotemporal integral term s_i . In this formulation the elastodynamic response is separated between local and nonlocal contributions. s_i represents the nonlocal elastodynamic long-range interaction between different parts of the surface, and the local effect $\eta_{ij} \frac{\mu}{c_s} \dot{u}_j$ represents wave radiation from the surface.

We use the spectral approach ([Breitenfeld and Geubelle, 1998](#)) for computing s_i which involves a Fourier transform in space and a convolutions in time, where the displacement history is convolved with the elastodynamic kernels. Please refer to independent formulation in ([Breitenfeld and Geubelle, 1998](#)) for the derivation of the kernels and details for computing the nonlocal term, s_i .

2.2.4 Hybrid FEM-SBIM Method

The hybrid method consists in coupling the FEM and the SBIM at the boundaries S^\pm , where the FE-domain is truncated (see Fig. [5.2.1c](#)). At S^\pm , which we refer to as the virtual boundary, we apply an exact elastodynamic transparent boundary condition using the SBIM, which accounts for wave propagation in the infinite half-space beyond the FE truncation. Depending on the FE scheme, Neumann or Dirichlet boundary conditions might be more suitable. For example, Dirichlet boundary conditions might result in a more stable algorithm. Here, we present the Neumann approach (for the Dirichlet approach please refer to [Ma et al. \(2019\)](#)). We impose continuity condition at the bound-

aries S^\pm , which results in the FE force \mathbf{f} being equal to the SBI traction τ^{SBI} multiplied by a rotation-area matrix \mathbf{B}^{SBI} .

The Neumann approach consists in solving the boundary integral relation, Eq. (2.19), by using the displacements and velocity computed from the FEM. The resulting traction is then applied as a Neumann boundary condition in the FEM. A time step of the hybrid method is computed as follows:

1. FE compute explicit time integration Eq. (2.12) and predict velocity Eq. (2.11)
2. copy \mathbf{u}_{t+1} and $\dot{\mathbf{u}}_{t+1}^{\text{pred}}$ from FE to SBI
3. SBI compute response of half space, τ^{SBI} , for given displacement history $u(x_1, x_3, t)$ and current velocity prediction $\dot{u}_{t+1}^{\text{pred}}$ Eq. (2.19)
4. apply SBI interface traction as Neumann boundary condition in FE: $\mathbf{f} = \mathbf{B}^{\text{SBI}}\tau^{\text{SBI}}$
5. FE compute friction traction τ_{t+1} using Eq. (2.18)
6. FE compute acceleration increment Eq. (2.13)
7. FE correct velocity Eq. (2.14)

Alternative coupling methods, *e.g.*, Lagrange multiplier, could also be applied. However, as we will show in Sec. 2.3, the simple staggered approach proposed here provides excellent accuracy and is optimal in terms of computational efficiency. Further, in the finite-element domain, we apply 8-node linear hexagonal elements in a regular mesh in all presented problems.

2.3 Benchmark problem TPV3: Earthquake rupture in unbounded homogeneous domain

2.3.1 Setup

We verify the hybrid method with the benchmark problem TPV3 from the SCEC Dynamic Rupture Validation exercises (<https://strike.scec.org/cvws/>). The problem considers a planar fault, governed by linear slip-weakening friction, embedded in a homogeneous linear elastic bulk (see Fig. 2.2a). The elastic bulk has a density of $\rho = 2670 \text{ kg/m}^3$, pressure wave speed $c_p = 6000 \text{ m/s}$, and shear wave speed $c_s = 3464 \text{ m/s}$. The friction properties are uniform and characterized by $\mu_s = 0.677$, $\mu_k = 0.525$ and $d_c = 0.4 \text{ m}$. A uniform background shear, $\tau_0 = 70 \text{ MPa}$, and normal stress, $\sigma_0 = 120 \text{ MPa}$, are applied. The rupture is nucleated at the center of the fault over a square patch of size a^2 by instantaneously increasing the shear stress to a value higher than the static friction. After nucleation, the rupture quickly propagates across the entire fault.

Note that this problem does not present any off-fault non-linearities and the fault is planar. Hence, the hybrid method is not required for this particular problem, which could be solved solely by the SBIM. However, we use this problem to verify the hybrid method by comparing the results with the reference solution of the SBIM. Additional examples, which do include non-linearities that require the hybrid method, will be presented in the following sections.

Additionally, in this example (as well as in Sec. 2.4 and 2.5) the fault (*i.e.*, the 13 plane) represented a symmetry plane. The implication of this are twofold: (i) the normal stress on the fault remains constant throughout the simulation and so do the peak and residual friction strengths (ii) there is no need of explicitly modelling the bottom half space of the simulation domain (*i.e.*, $x_2 < 0$), which is taken into account for when applying the frictional traction on the fault by enforcing $[[u_2]] = 0$ and $\sigma_{22} = const.$ Note that, by applying the hybrid method, we model the entire top (*i.e.*, $x_2 > 0$) half space. However, there are two additional symmetry planes: the 12 plane and the 23 plane. Thus, the FE computational domain could be further reduced by using the appropriate boundary conditions.

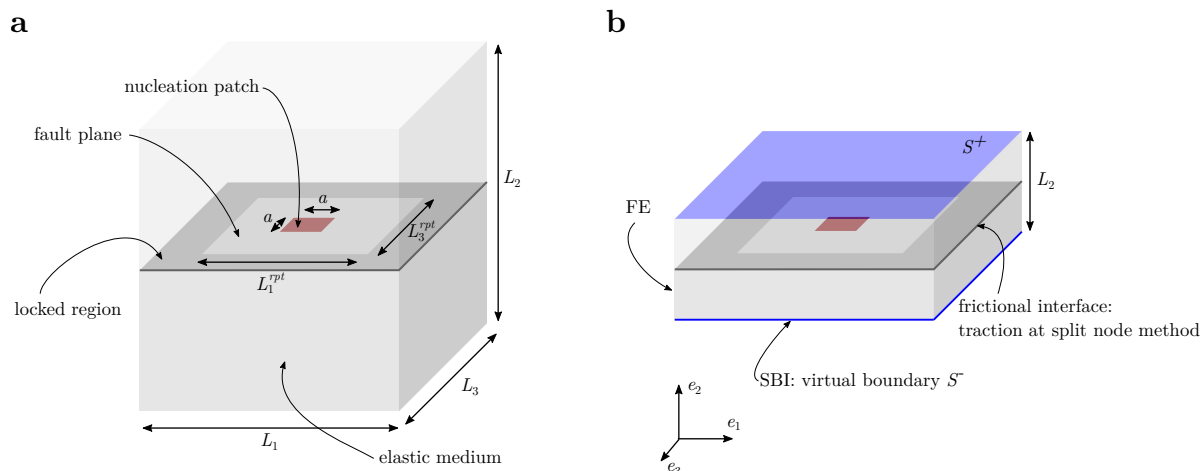


Figure 2.2: Setup of benchmark problem TPV3. (a) Earthquake rupture in unbounded domain with nucleation over square region of size $a = 3$ km and fault regions of size $L_1^{rpt} = 30$ km and $L_3^{rpt} = 15$ km. (b) Hybrid setup: FE domain with SBI as elastodynamic boundary condition.

2.3.2 Results

We present the results of the hybrid method with a virtual strip width $L_2 = 4\Delta x$ (see Fig. 2.2b) and compare it with the reference solution. For both methods we use the same spatial discretization with $\Delta x = 50$ m. Rupture front position (see Fig. 2.3a), and stress and slip time history at three stations (see Fig.2.3b) show excellent agreement between the hybrid method and the SBIM. Fig. 2.4 shows the shear stress σ_{12} field on one quadrant of the virtual strip. The rupture front is characterized by an abrupt change from peak to residual strength. The excellent agreement with the reference solution (Fig. 2.3) demonstrates that the the elastodynamic boundary condition enforced on the planes S^\pm does not cause any artificial wave reflection even though the virtual strip is extremely thin.

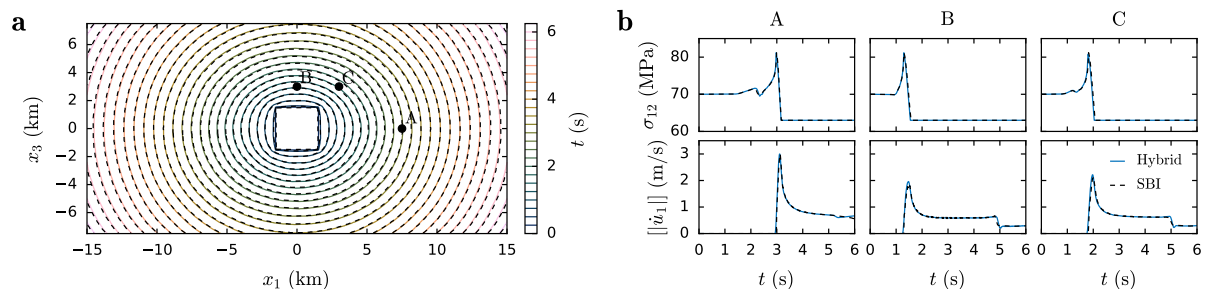


Figure 2.3: Benchmark problem TPV3 solved using hybrid method (blue lines) and using the SBIM (dashed black lines). (a) Contour of rupture front position each 0.5s. (b) Fault shear stress, σ_{12} , and slip rate, \dot{u}_1 , at three stations A, B, and C with position shown in (a).

We perform a mesh convergence study of the hybrid method and show that the L_2 norm of the error, computed using a reference solution with $\Delta x = 25$ m, decreases linearly (see Fig. 2.5a). The hybrid method combines linear finite elements with a higher preci-

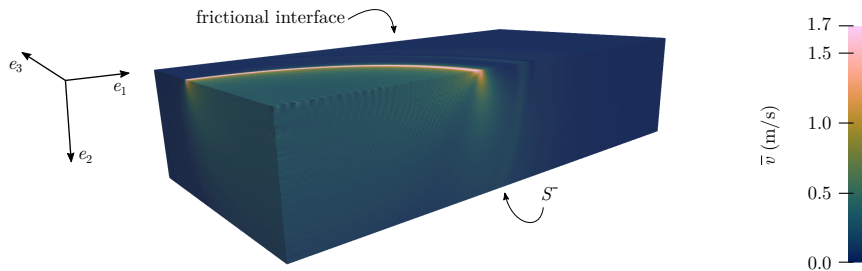


Figure 2.4: Benchmark problem TPV3 solved using hybrid method. Velocity magnitude field, \bar{v} , at $t = 3.4$ s. For better visualization we applied a much thicker virtual strip, *i.e.*, $L_2 = 10$ km instead of $L_2 = 0.2$ km as applied for simulations shown in Fig. 2.3.

sion spectral boundary method. Therefore, the convergence rate of the hybrid method corresponds to the rate of the least accurate of the methods it combines, *i.e.*, the linear finite element method. Hence, the hybrid method does not lose any accuracy compared to a fully FEM model.

Since we are dealing with a dynamic problem, we also show the temporal evolution of the error at station C (see Fig. 2.5b). The error is initially zero because the waves and the rupture have not reached the station yet. At $t \approx 1.8$ s, the rupture reaches the station (see also Fig. 2.3b) and hence the error increases rapidly. It then remains approximately constant while the fault continues to slide until reflected waves from the boundary between rupture region and locked region (not the virtual boundary) reach the station. At this point, we notice a temporary drop in the error before it increases again to the same level of error observed before. Overall, we find that the error remains mostly constant over the duration of the simulation and decreases with mesh refinement.

Even though this benchmark problem is linear elastic and does not necessitate the use of the hybrid method, it illustrates its capability of efficiently and accurately truncating

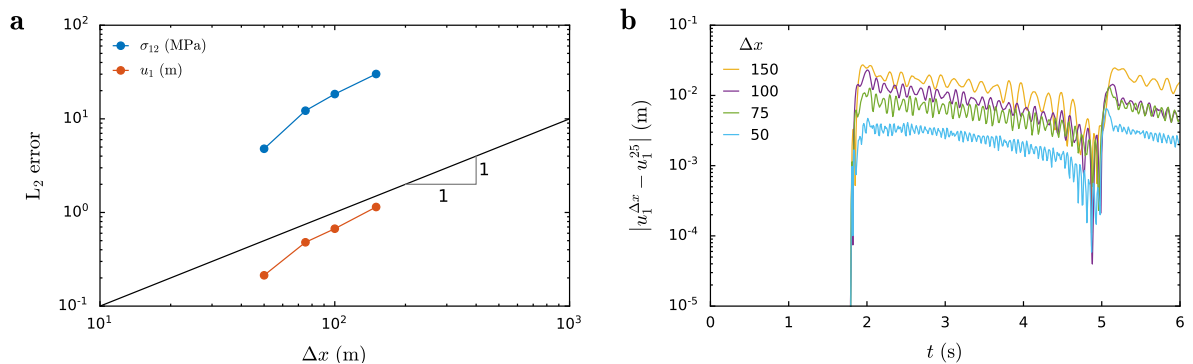


Figure 2.5: Benchmark problem TPV3 solved with hybrid method – mesh convergence study (a) L_2 error as function of mesh size Δx computed over the entire fault at $t = 3$ s. (b) Absolute error as function of time at station C.

elastic waves in the vicinity of the fault with no artificial reflections from the virtual boundaries, S^\pm , which were only two elements away from the fault. In more complex scenarios, this virtual strip might need to be larger in order to fully describe the source of non-linearities or heterogeneity. Nevertheless, this efficient near-field truncation algorithm enables us to decrease the domain of finite-element discretization, compared to a fully FEM model, and apply a volumetric mesh only in a narrow strip around the fault, which results in considerable savings in terms of both computational time and memory, as we will discuss further in Sec. 4.5.

2.4 Earthquake rupture with LVFZ: pulse-like behaviour

2.4.1 Setup

The previous example was a benchmark problem and could have been solved by a boundary-element approach without any discretization of the bulk. Hence, the hybrid method was not required. In the following, we will consider more complex problems, which require volumetric discretization. First, we consider a slip-weakening fault with a low velocity fault zone (LVFZ). LVFZ are found in most mature faults, where the near fault rock is considerably damaged and, as a consequence, has a reduced wave speed ranging from 20% to 60% with respect to the host rock (Ma and Elbanna, 2015; Huang and Ampuero, 2011; Huang et al., 2014, 2016; Albertini and Kammer, 2017). In 2D setups, when the reduction is high enough, the rupture behaves like a pulse. The results presented here will confirm this behavior on a 3D setup.

We consider a velocity reduction of 20% with respect to the surrounding host rock, which has the same elastic properties as in Sec. 2.3. The fault geometry is given in Fig. 2.6, and is governed by linear slip-weakening friction with $\mu_s = 0.677$, $\mu_k = 0.564$, and $d_c = 0.2$. The fault is subjected by a uniform background shear $\tau^0 = 27.5$ MPa and normal $\sigma^0 = 44$ MPa stress. We nucleate the fault rupture over a square region of size a^2 by instantaneously applying a loading traction of 31 MPa, which locally exceeds the peak friction strength.

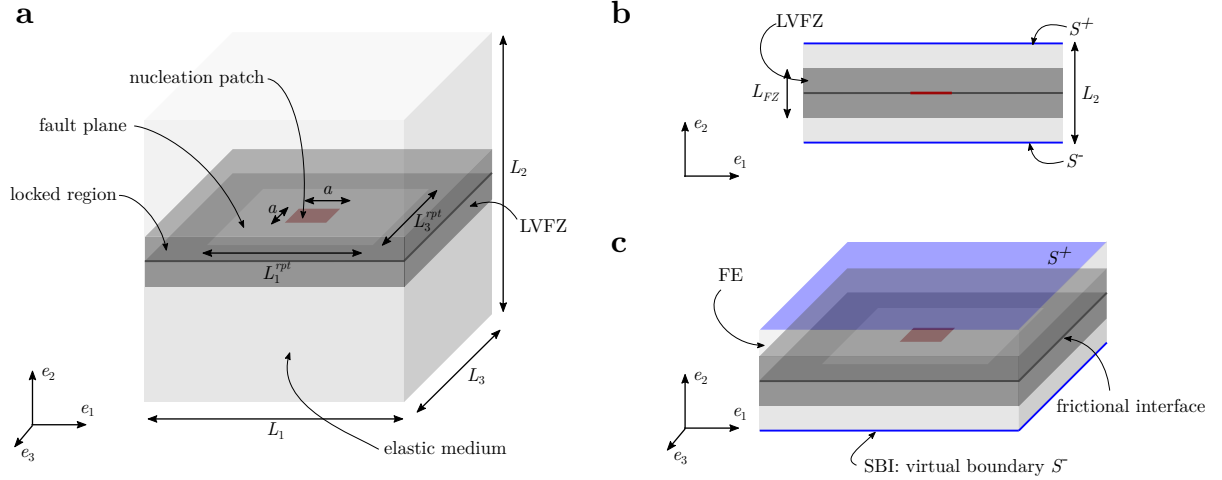


Figure 2.6: Setup of example earthquake rupture in unbounded domain with LVFZ. (a) Fault plane geometry and nucleation patch are analogous to the previous example but with a larger size: $L_1^{rpt} = 60$ km, $L_3^{rpt} = 30$ km, and $a = 3.2$ km. The fault zone region surrounding the fault is more compliant and presents a thickness of $L_{FZ} = 1.6$ km. (b) Hybrid setup: FE virtual strip with $L_2 = 2$ km and with SBI as elastodynamic boundary condition.

2.4.2 Results

As a result of the nucleation procedure, the rupture front quickly propagates radially and eventually spans the entire fault (see Fig. 2.7). When a dynamic rupture propagates, it radiates elastic waves, which are then reflected at the boundary of the LVFZ (Albertini and Kammer, 2017). Depending on the incident angle, the reflected wave can have an inverted polarization and cause unloading of the fault and generate a slip pulse. This effect is also observed in our 3D simulations and is shown in Fig. 2.7b, station C, and in Fig. 2.8. The reflected wave causes the rupture to split into a pulse-like rupture, followed by a crack-like rupture.

The rapid acceleration and deceleration of a slip pulse are a source of high frequencies (see Fig. 2.9b Station C) and cause oscillations in slip velocity, trailing the rupture front (see Fig. 2.8). These oscillations do not affect the rupture propagation and disappear with further mesh refinement and regularized friction laws (Kammer et al., 2014). Additionally, numerical damping, which is not used here, is often applied to minimize such high frequencies. Since this problem cannot be solved with the SBI method, we validate the results of the hybrid method by varying the width of the virtual strip, L_2 , and confirm that the solution is independent on the location of the elastodynamic boundary condition.

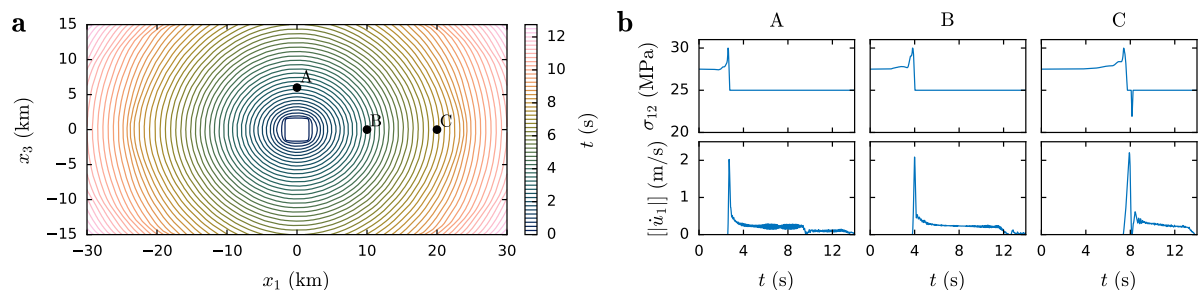


Figure 2.7: LVFZ setup solved using hybrid method with $\Delta x = 100$ m. (a) Contour of rupture front position each 0.5s. (b) Fault shear stress, σ_{12} , and slip rate, $[\dot{u}_1]$ at three stations A, B, and C with position shown in (a). At station C the rupture has split into a slip-pulse followed by a crack-like rupture.

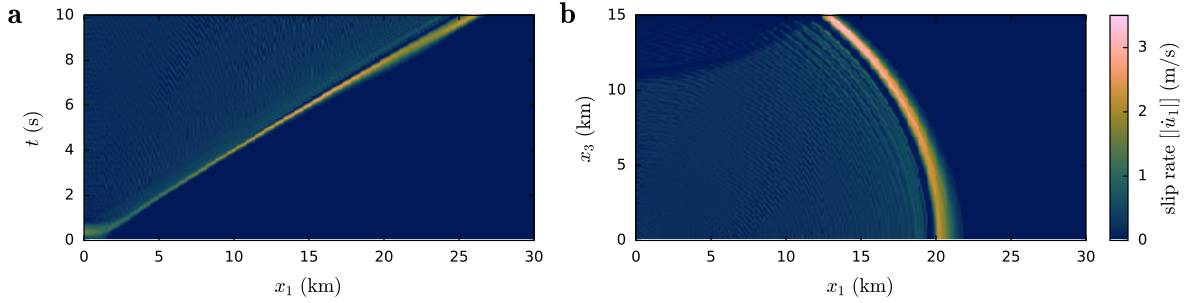


Figure 2.8: Pulse like rupture induced by LVFZ. (a) Space-time diagram of slip rate $[|\dot{u}_1|]$ along the symmetry axis $x_3 = 0$ km. At $t \approx 5$ s, the rupture splits into a slip-pulse, followed by a crack-like rupture. (b) Slip rate $[|\dot{u}_1|]$ at $t = 8$ s shows the spatial extent of the pulse-like and crack-like rupture.

2.5 Earthquake rupture in a heterogeneous medium: superhear transition

2.5.1 Setup

The second showcase example, presented in this section, is similar to the previous example but with the more compliant material being the one at a distance from the fault. We consider a slip-weakening fault with an off-fault low velocity zone. This case could occur when a fault ruptures and interacts with the LVFZ of a nearby mature fault (Ma and Elbanna, 2015; Albertini and Kammer, 2017). We use the same geometry, friction and elastic properties, and nucleation procedure as in Section 2.4 but consider the fault to be embedded in the reference material, while beyond a distance $L^{FZ}/2$ from the fault plane the material has a 20% velocity reduction.

2.5.2 Results

Similar as in the LVFZ setup of Sec. 2.4, elastic waves are reflected at the boundary of the low velocity inclusion and affect the shear stress at the interface. However, the reflected waves have the same polarity as the incident ones and, hence, increase the shear stress in front of the propagating rupture front (see Fig. 2.9b). This increasing shear stress peak eventually causes the rupture to transition from subRayleigh to supershear velocities (see Fig. 2.9a and Fig. 2.10). SubRayleigh propagation occurs when the rupture speed is lower than the Rayleigh wave speed, $c_R \approx 0.9c_s$, and can be observed at stations A and B in Fig. 2.9. Supershear propagation, however, refers to ruptures propagating faster than c_s and their speed can approach the limiting speed, c_p (Freund, 1979; Kammer et al., 2018). In our simulations, supershear rupture occurs within the domain surrounding station C in Fig. 2.9a.

In this 3D simulation, we observe a supershear transition through the Burridge-Andrews mechanism (Burridge, 1973; Andrews, 1976), where a shear stress peak in front of the existing crack nucleates the supershear rupture (see Fig. 2.9b, station B and Fig. 2.10). In contrast to 2D setups (Ma and Elbanna, 2015; Albertini and Kammer, 2017), the extent of the supershear rupture is confined to a triangular shaped region, which surrounds station C. Additionally, the transition occurs progressively: first at $x_3 = 0$ km at $t \approx 7$ s, then it expands towards the $\pm e_3$ direction, and finally, at $t \approx 12$ s it spans the entire seismogenic depth.

This example illustrates the ability of the hybrid method of successfully truncating the shear Mach front, radiated from the supershear rupture, without artificial reflections. Which allows us place the virtual boundary S^\pm at only $2\Delta x$ from the the boundary of the low velocity inclusion. As in the previous problem, we validate the results of the hybrid method by varying the width of the virtual strip, L_2 . The solution is found to be independent on L_2 .

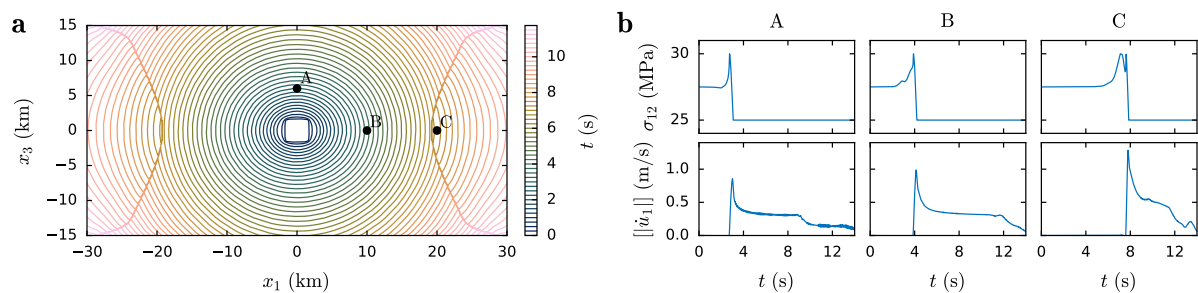


Figure 2.9: Off-fault low velocity zone setup solved using hybrid method with $\Delta x = 100$ m. (a) Contour of rupture front position each 0.5s. Widely spaced contour lines represent supershear propagation region. (b) Fault shear stress, σ_{12} , and slip rate, $[\dot{u}_1]$ at three stations A, B, and C with position shown in (a).

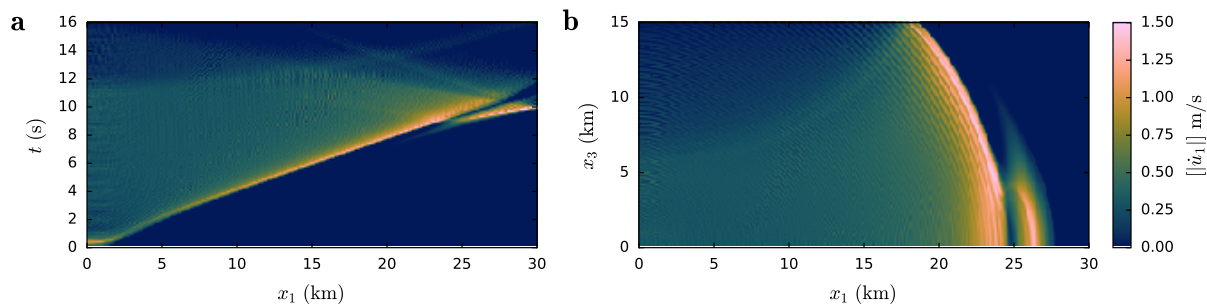


Figure 2.10: Supershear transition induced by off-fault low velocity zone. (a) Space-time diagram of slip rate $[\dot{u}_1]$ along the symmetry axis $x_3 = 0$ km. The rupture transitions to supershear at $x_1 \approx 24$ km. (b) Slip rate at $t = 9.25$ s shows the spatial extent of the supershear rupture, just after the transition has initiated.

2.6 Earthquake rupture with step-over faults

2.6.1 Setup

Finally, we present an example of interaction between nearby faults, *i.e.* two fracture planes side-by-side. We consider a dilational step-over geometry with a system of two faults that overlap each other (see Fig. 2.11). The dilational step-over implies that the location of the secondary fault with respect to the primary one is such that the rupture propagation on the primary fault will cause a temporary reduction in normal stress. The faults have uniform friction properties, $\mu_s = 0.677$, $\mu_k = 0.373$ and $d_c = 0.5$ m, except on the top 1 km of the seismogenic zone, where a slip-strengthening condition is imposed. At the bottom, *i.e.*, $x_3 < L_3^{rpt}$, we consider a no slip boundary condition and the nucleation is achieved by an instantaneous reduction of the friction strength over a region of size $a \times L_3^{rpt}$ to its kinetic value. This setup is analogous to a recent study by [Bai and Ampuero \(2017\)](#). The elastic properties are the same as in Section 2.3. We choose a seismogenic depth, $L_3^{rpt} = 10$ km and uniform background shear $\tau_0 = 71.2$ MPa and normal stress $\sigma_0 = 150$ MPa. Hence, the strength ratio is $S = (\mu_s \sigma_0 - \tau_0) / (\tau_0 - \mu_k \sigma_0) = 1.75$, and the condition for the rupture to jump from one fault to the adjacent one is satisfied ([Bai and Ampuero, 2017](#)).

Note that in this example there are no symmetries. In contrast to the previous examples where the fault plane represented a symmetry axis. As a result of the slip propagation on the primary fault, the normal stress on the secondary fault is not constant.

The change in normal stress can reduce or increase the friction strength on the secondary fault, depending on their relative position. Thus, it can hinder or promote the rupture to jump between faults.

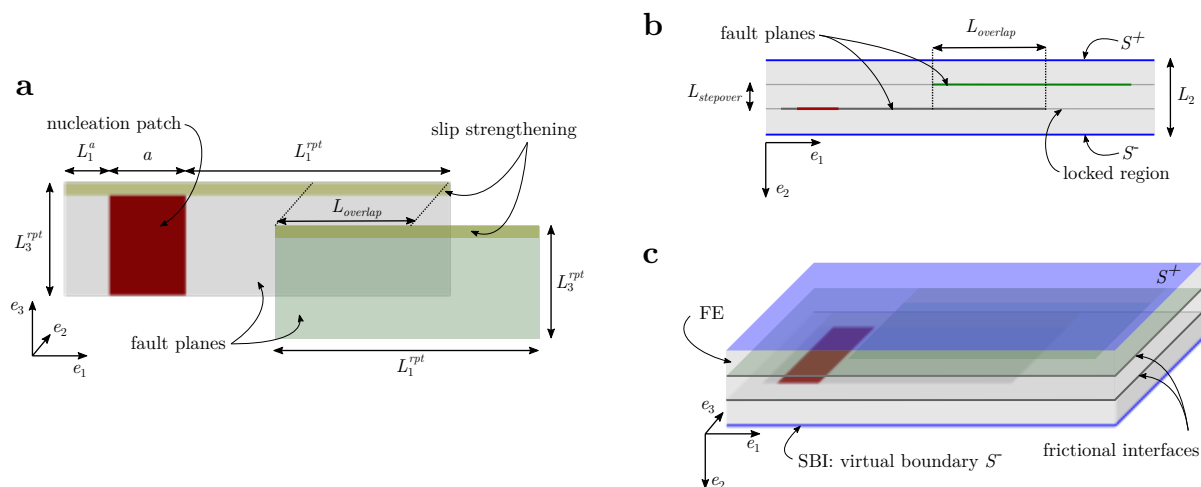


Figure 2.11: Setup of example earthquake rupture in unbounded domain with interacting parallel faults with step-over geometry. (a) Setup geometry. Fault zone regions of rectangular size with $L_1^{rpt} = 40$ km and $L_3^{rpt} = 10$ km, with nucleation over a width $a = 20$ km and the entire seismogenic depth, L_3^{rpt} . To the left of the nucleation patch the extent of the primary fault is $L_1^a = 10$ km. The two fault step-over geometry is characterized by $L_{overlap} = 20$ km and $L_{stepover} = 1$ km, shown in (b). The faults are embedded in a homogeneous elastic medium. (b and c) Hybrid setup: FE domain with SBI as elastodynamic boundary condition. The virtual strip width is $L_2 = 1.4$ km.

2.6.2 Results

Using the hybrid method, we can successfully reproduce the results of [Bai and Ampuero \(2017\)](#) (see Fig. 2.12): after nucleation, the rupture propagates over the primary fault with a nearly vertical front, then the rupture jumps to the secondary fault and, as a consequence of the no-slip boundary condition beyond the depth L_3^{rpt} , the rupture be-

comes a slip pulse. The wave emitted by the primary rupture successfully nucleates a large rupture on the secondary fault in the forward direction. This example illustrates the ability of the hybrid method to efficiently solve a large and complex simulation and efficiently truncate all incident waves without any artificial reflections. To validate the results of the hybrid method we vary the width of the virtual strip, L_2 , and find that also for this example L_2 does not affect the solution.

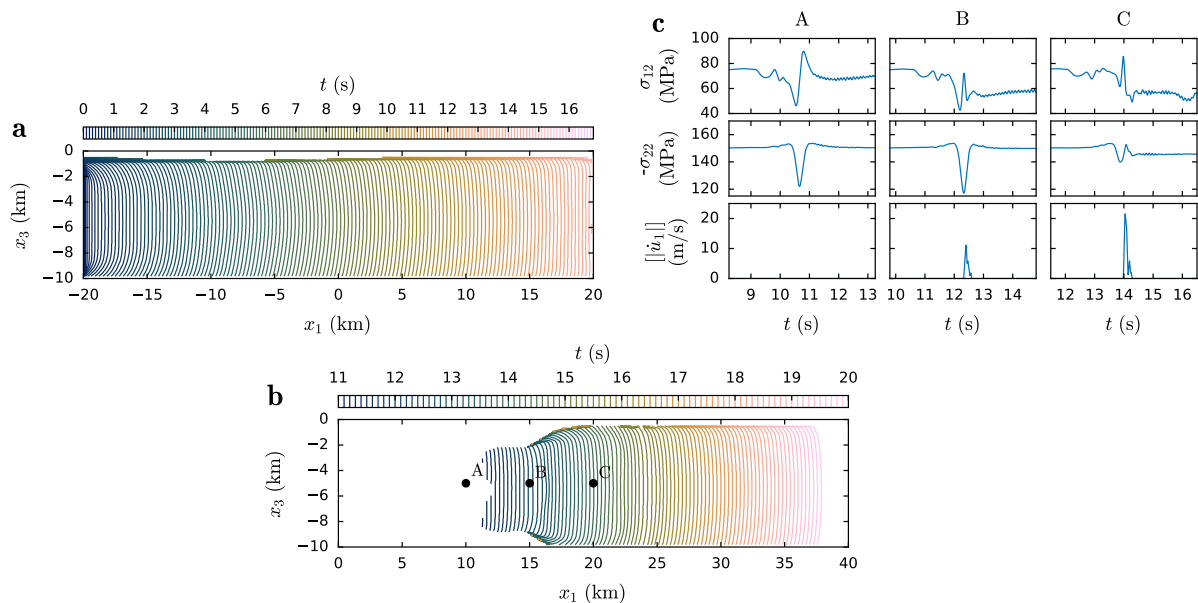


Figure 2.12: Results of example earthquake rupture in unbounded domain with interacting parallel faults with dilational step-over setup and spatial discretization $\Delta x = 100$ m. (a) Rupture front contour lines on primary fault, where nucleation occurs over region $-40 \text{ km} < x_1 < -20 \text{ km}$ (not shown). (b) Rupture front contour lines on secondary fault. Rupture transitions from primary to secondary fault. (c) Fault shear, σ_{12} , and normal, σ_{22} , stress and slip rate, $||\dot{u}_1||$ at three stations A, B, and C with position on the secondary fault shown in (b).

2.7 Discussion

We used a SCEC benchmark problem to validate the hybrid method and then demonstrated its flexibility and superior performance on more complex and heterogeneous problems. The proposed hybrid method takes its flexibility to deal with nonlinearities or bulk heterogeneities from the FEM and its computational efficiency from the SBIM. In particular, since the SBIM provides a perfect wave absorption algorithm there is no artificial wave reflection at the virtual boundary. Thus, one can reduce the width of the FEM domain arbitrarily close to the nonlinear or heterogeneous region, as long as the constitutive relation of the bulk beyond the virtual strip can be assumed to be linear.

The computational savings of using the hybrid method – instead of a traditional FEM – can be assessed by considering the complexity of both FEM and SBIM. The complexity of an explicit FEM time step is proportional to the number of degrees of freedom of the FEM problem, *i.e.*, $\mathcal{O}(N_1 N_2 N_3)$, where N_i is the number of elements in the i -direction and we assume a regular mesh of hexagonal elements. Similarly, the complexity of an SBIM time step scales with its number of degrees of freedom $\mathcal{O}(N_1 N_3)$. We measured the computation time for a range of simulations with different discretizations and domain sizes, which confirms the linear relationship between computational cost and the number of degrees of freedom (see Fig. 2.13). The computational saving of the hybrid method compared to a standard FEM lies in the reduction of N_2 due to the truncation of the FE domain. Moreover, the added overhead cost of the SBI as wave absorption algorithm is in the same order of magnitude of only one layer of FE elements (see Fig. 2.13b). Therefore, it is practically negligible.

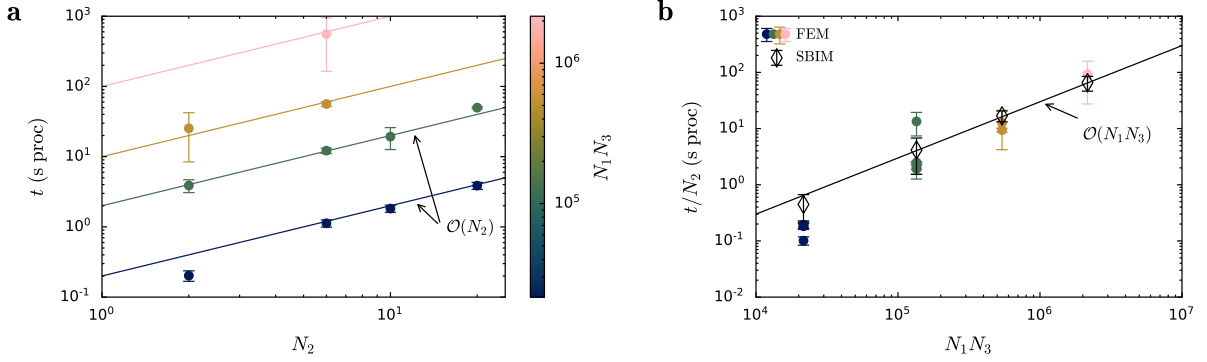


Figure 2.13: Performance study of FEM and Hybrid method. (a) Computation time, t , of a FEM time step as function of width of the virtual strip, *i.e.*, number of elements, N_2 . Scaling of computational time is shown for a range of frictional interface discretizations, $N_1 N_3$. The complexity of the FEM time step is linear in N_2 . (b) Computation time of the FEM time step, t , normalized by N_2 (same data and color-code as in (a)). The computation time of a SBIM time step, when computing the elastodynamic boundary condition for the virtual strip, is equivalent to the computation time for one layer of FEM elements. Both, FEM and SBIM computation times are linear in $N_1 N_3$.

For example, for a full FE simulation, L_2 must be in the order of L_1 to prevent artificial reflections at the domain boundary. However, using the hybrid method the domain size can be truncated up to the extent of the nonlinear region or the extent of the elastic heterogeneity, which are usually one to two orders of magnitude smaller than L_1 (Ma and Elbanna, 2015). Assuming a regular spatial discretization, the domain truncation results in a reduction of N_2 by one order of magnitude and so will the computational cost. The savings may be even higher in other applications.

All our simulations were performed using distributed memory parallel computing with 48 threads and for the largest simulations 96 threads. Therefore, in Fig. 2.13, we report the computational time multiplied by the number of parallel processes. However, the SBIM library that we are using also supports shared memory parallelism and it is

designed to be easily coupled to any FEM library written in C++. The only requirement is that the FEM mesh at the virtual boundary S^\pm is a regular grid, due to the spectral representation of the boundary integral equations.

These computational savings represent an important step towards feasible modelling of complex temporal and spatial multi-scale 3D problems such as earthquake cycle simulations with near field heterogeneities, nonlinear material behavior and plasticity, as well as a networks of interacting faults, including fault branches and non-planar fault geometry. The major challenge of earthquake cycle simulations is that they involve very long interseismic loading time (years) while the dynamic rupture happens extremely rapidly (seconds). An advantage of the hybrid method is that the SBIM is already capable of absorbing elastic waves in the dynamic as well as in the quasi-dynamic limit and these approaches can be combined in a variable time stepping scheme, introduced by [Lapusta et al. \(2000\)](#). Such a temporal multi-scale simulation couples a quasi-dynamic SBIM with an implicit FEM during the slow loading phase and, once the ruptures become dynamic, it switches to a dynamic SBIM coupled with an explicit FEM – as considered in the current study. This variable time-stepping hybrid method was introduced in a 2D antiplane framework ([Abdelmeguid et al., 2019](#)) and will be extended to 3D in future work.

Another advantage of the hybrid method is that it could be implemented with any volume based method. For example, if the fault plane is not known a priori, one could use discretization techniques with embedded discontinuities, such as the XFEM ([Liu and Borja, 2009](#)) or the discontinuous Galerkin ([Pelties et al., 2012](#)).

2.8 Conclusion

We developed a three dimensional hybrid method combining the finite-element method with the spectral boundary-integral method. We validated the hybrid method using a benchmark problem and illustrated its potential for solving complex earthquake propagation on various example problems including near systems with field heterogeneity and multiple interacting faults. The hybrid method is suitable for cases where the spatial extent of near field nonlinearity and heterogeneity is too large to be lumped into an effective fault constitutive law, but is still considerably smaller than the domain of interest for the wave propagation. In these cases, the hybrid method allows for a reduction of computational cost by at least one order of magnitude with respect to a full finite-element implementation, while maintaining the same level of accuracy. The high accuracy and computational efficiency of the hybrid method enable the investigation of complex failure problems such as multi-physics fault zone problems.

CHAPTER 3

OFF-FAULT HETEROGENEITIES PROMOTE SUPERSHEAR TRANSITION OF DYNAMIC MODE II CRACKS

This chapter is drawn from the following peer-reviewed journal article:

Albertini, G. and Kammer, D. S. (2017) , ‘Off-fault heterogeneities promote supershear transition of dynamic mode II cracks’, *Journal of Geophysical Research: Solid Earth* **122**(8), 2017JB014301.

The transition from sub-Rayleigh to supershear propagation of mode II cracks is a fundamental problem of fracture mechanics. It has extensively been studied in homogeneous uniform setups. When the applied shear load exceeds a critical value, transition occurs through the Burridge-Andrews mechanism at a well-defined crack length. However, velocity structures in geophysical conditions can be complex and affect the transition. Damage induced by previous earthquakes causes low-velocity zones surrounding mature faults and inclusions with contrasting material properties can be present at seismogenic depth. We relax the assumption of homogeneous media and investigate dynamic shear fracture in heterogeneous media using two-dimensional finite-element simulations and a linear slip-weakening law. We analyze the role of heterogeneities in the elastic media, while keeping the frictional interface properties uniform. We show that supershear transition is possible due to the sole presence of favorable off-fault heterogeneities. Sub-critical shear loads, for which propagation would remain permanently sub-Rayleigh in an equivalent homoge-

neous setup, will transition to supershear as a result of reflected waves. P-wave reflected as S-waves, followed by further reflections, affect the amplitude of the shear stress peak in front of the propagating crack, leading to supershear transition. A wave reflection model allows to uniquely describe the effect of off-fault inclusions on the shear stress peak. A competing mechanism of modified released potential energy affects transition and becomes predominant with decreasing distance between fault and inclusions. For inclusions at far distances, the wave reflection is the predominant mechanism.

Keypoints:

- Off-fault heterogeneities cause supershear transition for sub-critical pre-stress.
- P-waves reflected as S-waves start promoting transition, other waves follow.
- Competing mechanism of reduced released potential energy can delay transition.

3.1 Introduction

Earthquakes are generally modeled as frictional mode II ruptures of tectonic faults. The majority of such ruptures propagate at speeds c_f below the Rayleigh wave speed c_R . However, under particular circumstances supershear (also called intersonic in fracture mechanics literature) propagation might occur, where fracture propagates between the shear wave speed c_s and the longitudinal wave speed c_p . Supershear propagation is fundamentally different from sub-Rayleigh propagation because S-wave radiated by the supershear crack tip coalesce into a S-wave Mach cone, which transports high stresses and particle velocities far away from the weak interface (Dunham and Archuleta, 2005; Bernard and Baumont, 2005; Bhat et al., 2007). Growing geophysical evidence shows that supershear propagation is possible and has been inferred for several earthquakes (Spudich and Cranswick, 1984; Archuleta, 1984; Olsen et al., 1997; Bouchon et al., 2002; Bouchon and Vallée, 2003; Dunham and Archuleta, 2004; Wang et al., 2012; Yue et al., 2013; Zhan et al., 2014).

Early theories of dynamic fracture mechanics suggested that c_R constitutes an upper limit for shear crack propagation (Freund, 1972, 1979). Further considerations, taking into account the process zone at the crack tip provide analytical solutions for cracks propagating at varying supershear speeds (Broberg, 1989; Huang and Gao, 2001, 2002). These analytical models define an energetically inadmissible velocity domain $c_R < c_f < c_s$, where mode II crack propagation cannot exist in a uniform and homogeneous setup. An analytical self-similar model (Burridge, 1973) as well as remarkable numerical simulations (Andrews, 1976) found a mechanism (known as the Burridge-Andrews mechanism)

allowing transition from sub-Rayleigh to supershear propagation. As a shear crack becomes dynamic it accelerates quickly and approaches, asymptotically c_R . A shear wave is generated during the acceleration process resulting in a shear stress peak τ_w propagating at c_s ahead of the sub-Rayleigh rupture front. The amplitude of τ_w is growing with increasing propagation distance. If the applied shear load τ_0 exceeds a critical value, τ_w eventually reaches the interface strength and nucleates a secondary supershear rupture $c_f > c_s$. Shortly after, the main crack and the secondary rupture coalesce and continue propagation at supershear speed. The growth of τ_w was shown to scale with the critical half-length l_c (Andrews, 1976; Svetlizky et al., 2016), which is defined for a plane-strain central crack by:

$$l_c = \frac{2\mu}{\pi(1-\nu)} \frac{\Gamma}{(\tau_0 - \tau_r)^2} \quad (3.1)$$

where μ and ν are the material's shear modulus and Poisson's ratio, respectively, and Γ the fracture energy. Therefore, the normalized position of supershear transition x_{trans}/l_c is uniquely defined for a given dimensionless strength $S = (\tau_p - \tau_0)/(\tau_0 - \tau_r)$, where τ_p and τ_r are the peak and residual shear strength. However, if the applied load is sub-critical (i.e., $S > S_{\text{max}}$) the shear stress peak will never reach the interface strength and no transition to supershear occurs at any length. S_{max} was analytically derived from a self-similar model (Burridge, 1973). Very high pre-stress values (i.e., $S < S_{\text{min}}$) induce a direct supershear transition, with crack propagation speed continuously accelerating through the inadmissible velocity domain (Bizzarri and Das, 2012; Liu et al., 2014; Payne and Duan, 2015).

Experimental evidence of supershear crack propagation in homogeneous condition has first been observed at frictional interfaces on Homalite plates, where the S-wave Mach

cone was revealed through photo-elasticity (Rosakis et al., 1999; Xia et al., 2004). Stick-slip experiments on crustal rock also showed supershear propagation (Passelègue et al., 2013). Supershear transition mechanism has been recently observed on PMMA interfaces illustrating explicitly the growth of τ_w and its link to the nucleation of a secondary supershear crack (Svetlizky et al., 2016).

Other mechanism causing supershear transition have been numerically studied for various setups considering heterogeneities along the weak interface, such as differences in fracture energy (Dunham et al., 2003), patches of higher pre-stress and pre-existing sub-critical cracks (Liu and Lapusta, 2008) and patches of higher normal load (Weng et al., 2015). The knowledge gained in these idealized cases is valuable to understand more complex setups, such as interaction between multiple faults (Harris et al., 1991; Hu et al., 2016).

Velocity structures can be complex at the proximity of faults. Damage causes seismic velocity reduction up to 60% over a distance of hundreds of meters surrounding the fault (Huang et al., 2014). Low-velocity fault zones are common in many mature faults such as the San Andreas (Lewis and Ben-Zion, 2010; Li et al., 2006), San Jacinto (Lewis et al., 2005; Yang and Zhu, 2010), Landers (Li et al., 2007; Peng et al., 2003), Hector Mine (Li et al., 2002), Calico (Cochran et al., 2009; Yang et al., 2011), Nojima (Mizuno et al., 2008) and Anatolian (Ben-Zion et al., 2003) faults. Ruptures propagating within the low-velocity zone feature a pulse-like behavior and can transition to supershear propagation (Huang and Ampuero, 2011; Huang et al., 2014, 2016). Ruptures along bi-material interfaces are affected by dynamic changes in normal stress and present various com-

plex propagation behavior, e.g. wrinkle-like pulses (Harris and Day, 1997; Ben-Zion and Huang, 2002; Brietzke and Ben-Zion, 2006; Barras et al., 2014; Xu et al., 2015).

However, limited attention has been given to setups featuring low-velocity inclusions at a distance from the fault. Such cases could be encountered when a rupture on a fault interacts with a damaged zone of a nearby fault network (and the low-velocity zone surrounding the fault itself has not developed yet). For instance, high definition seismic tomography of the San Jacinto Fault zone, reveal complex velocity structures with contrast up to 20% at seismogenic depth in areas of the Hot Spring and Trifurcation (Allam and Ben-Zion, 2012; Allam et al., 2014; Zigone et al., 2015). Parts of the San Andreas Fault in the Mojave section show multiple parallel faults (e.g. the 1857 and currently active rupture trace and the long-term San Andreas Fault trace) and asymmetric damage zones (Rempe et al., 2013). Ruptures on the active, more recent fault would be affected by the damaged zone of the preexisting older fault. The Kunlun Fault in the Tibetan Plateau, which experienced a supershear earthquake in 2001 (Bouchon and Vallée, 2003), features a mid-crustal low-velocity zone (Le Pape et al., 2012; Li et al., 2012; Yang et al., 2012; Jiang et al., 2014; Li et al., 2014) where velocity contrast up to 16% is present at seismogenic depth. In these conditions, ruptures could either propagate at the bi-material interface or on faults at a distance from the low-velocity zone. Previous studies suggest that off-fault heterogeneities can affect dynamic crack propagation and the position of supershear transition (Huang and Ampuero, 2011; Ma and Elbanna, 2015; Huang et al., 2016). However, the underlying mechanisms are not well understood yet.

By considering a uniform loading and uniform frictional interface properties, we investigate the effects of heterogeneities in the elastic medium on supershear transition, using dynamic 2D finite-element simulations and a linear slip-weakening law. Considering low loading conditions $S > S_{\max}$, such that transition would not occur in homogeneous cases, we show that the sole presence of such inclusions can trigger supershear transition. By the means of parameter studies, we assess under which circumstances transition can occur, and identify the role of geometry and material properties. Supported by an analytical wave reflection model, we identify the important role of reflected S-waves, which is the major mechanism promoting supershear transition. A competing mechanism of reduced available elastic energy is identified and becomes predominant when the wave reflection length scale is lower than a critical value. Hence, two distinct regimes are identified: one mainly governed by wave reflections at the boundaries of the heterogeneities and a second where the elastic field of the inclusions combined with wave reflections affect dynamic crack propagation.

3.2 Methods

We consider a central mode II crack expanding in both directions in infinite elastic media as shown in Figure 3.1. A plane-strain linear elastic material law is considered. Let a Cartesian coordinate system x, y be defined, with origin at the center of the crack and with the abscissa superposing the interface. Off-fault inclusions are introduced at a distance h_1 on each side of the fault. They are parallel to the interface and have thickness h_2 . For

simplicity, the inclusions are of infinite length (in x direction) and the symmetry of the setup avoids dynamic changes in normal stress at the interface. Stress concentrations at the ends of shorter inclusions would cause non-uniform stress at the interface and affect the transition length. Effect of non-uniform stress on supershear transition was studied by [Liu and Lapusta \(2008\)](#). The infinite length allows us to eliminate this effect and focus on the dynamic contribution of the off-fault inclusions. Once transition has occurred, supershear propagation continues regardless of further extension of the inclusion ([Ma and Elbanna, 2015](#)).

The elastic properties of the bulk material are defined by the shear modulus μ , Poisson's ratio ν and density ρ . Given the plane-strain setup and $\nu = 0.25$, the relevant dimensionless material property is given by the ratio $k = c_s/c_p = \sqrt{(1 - 2\nu)/2(1 - \nu)} = 1/\sqrt{3}$. Therefore, the critical load for supershear transition is $S_{\max} = 1.77$. The inclusions have a different shear modulus μ^h and consequently a contrasting S-wave speed c_s^h , while ν and ρ are kept unchanged. Hence, the elastic properties of the inclusions are solely characterized by velocity ratio c_s^h/c_s .

The friction properties are uniform along the interface and are modeled by a linear slip-weakening law. The interface strength is defined as function of slip δ :

$$\tau_{\text{st}}(\delta) = \begin{cases} \tau_p + (\tau_r - \tau_p)(\delta/\delta_c) & \text{for } \delta < \delta_c \\ \tau_r & \text{for } \delta \geq \delta_c \end{cases} \quad (3.2)$$

where δ_c is the critical slip distance. Neither healing, nor regularization are applied. The resulting fracture energy Γ of the interface is given by

$$\Gamma = (\tau_p - \tau_r)\delta_c/2 . \quad (3.3)$$

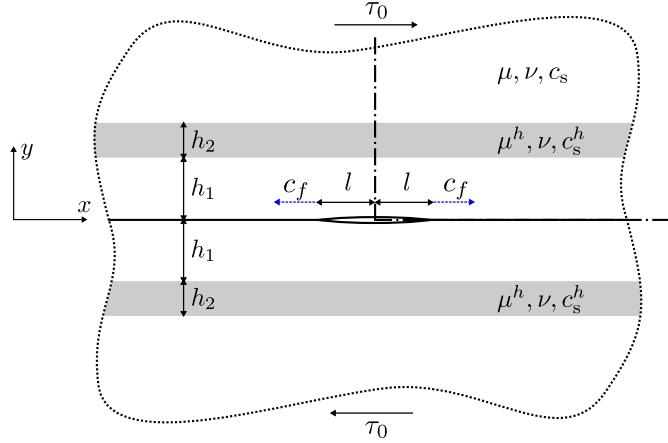


Figure 3.1: Setup used for simulations. Central crack of length $2l$ in infinite elastic medium containing a frictional interface (solid line at $y = 0$) and inclusions characterized by the fault distance h_1 , thickness h_2 and velocity ratio c_s^h/c_s . A uniform shear load τ_0 is applied. Only a quarter of the full domain is modeled by applying appropriate boundary conditions at the two anti-symmetry axis (dashed-dotted lines).

We apply the following normalization for space $\bar{x} = x/l_c$, time $\bar{t} = c_s t/l_c$ and friction traction $\bar{\tau} = (\tau - \tau_0)/(\tau_0 - \tau_r)$. Thus, the setup is general to different length scales and is characterized uniquely by S , k and, in the heterogeneous case, by \bar{h}_1 , \bar{h}_2 and c_s^h/c_s .

The initial condition for the dynamic simulations is given by the static solution for a setup containing no crack under a uniform stress τ_0 . A seed crack is nucleated by locally weakening the strength of the interface. We apply this strength reduction from τ_p to τ_r linearly over time, over a slowly growing area, which leads to a seed crack propagating at a rate of $c_f \approx 0.1c_R$. This smooth nucleation procedure was shown to produce elastic waves as observed in experiments by Svetlizky et al. (2016) and that are equivalent to the waves created by the smooth nucleation applied by Liu and Lapusta (2008).

The dynamic simulations are based on the finite-element method (Belytschko et al., 2013). First order quadrangular elements and a regular mesh of size 3200×1600 are used, which corresponds to a resolution of $\Lambda_0/\Delta x = 23.1$, where Λ_0 is the static process zone size given by (Palmer and Rice, 1973; Rice, 1980):

$$\Lambda_0 = \frac{9\pi}{32(1-\nu)} \frac{\mu\delta_c}{(\tau_p - \tau_r)}. \quad (3.4)$$

Key simulations, which include cases with high material contrasts, were repeated with a finer mesh (6400×3200) to verify mesh convergence. The Newmark- β time integration is implemented through an explicit scheme ($\beta = 0, \gamma = 0.5$). Numerical stability is assured by imposing a Courant-Friedrichs-Lewy condition with a time-step factor of 0.1. A traction-at-split-node technique is used to apply the tractions at the frictional interface. The system we study has two anti-symmetry axis (dash-dotted lines on Figure 3.1). In order to reduce computational cost, anti-symmetry boundary conditions are applied to the frictional interface ($y = 0$) and to the vertical axis ($x = 0$). From anti-symmetry, we have that $u_x(x, y) = -u_x(x, -y) = u_x(-x, y)$ and $u_y(x, y) = u_y(x, -y) = -u_y(-x, y)$, where u_x, u_y are the displacement fields in the x and y direction, respectively. This allows us to simplify the governing equations and compute the relative fields by considering only the elements on one side of the anti-symmetry axis. The boundary conditions are $\sigma_{xx}(0, y) = 0$, $u_y(0, y) = 0$, $\sigma_{yy}(x, 0) = 0$ and $\delta = 2u_x(x, 0)$, where σ is the stress tensor. Hence, only the upper right quarter of the domain is simulated ($x > 0, y > 0$). The infinite domain assumption is assured by limiting the region of interest to areas unaffected by wave reflection at the left and upper boundaries of the simulation domain. Simulations with larger domain have been performed to validate and identify the region of interest.

3.3 Effect of off-fault heterogeneities on supershear transition at low pre-stress

3.3.1 Illustrative homogeneous and heterogeneous examples

We first present two reference cases illustrating the effect of off-fault heterogeneities on the dynamic crack propagation. The propagation of a shear crack in a homogeneous medium is shown in Figure 3.2 (a). After the slowly extending seed crack reaches its critical length ($\bar{x} = 1$) it accelerates and asymptotically approaches the Rayleigh wave speed, following the equation of motion predicted by linear elastic fracture mechanics (Svetlizky et al., 2017).

Ahead of the rupture, a shear stress peak is radiated from the propagating front (indicated by dashed black line Figure 3.2 a). As was originally shown numerically by Andrews (1976) and experimentally confirmed by Svetlizky et al. (2016), the amplitude of the shear stress peak $\bar{\tau}_w$ continues to grow as a consequence of the acceleration process. The low pre-stress applied here results in a sub-critical loading $S = 2 > S_{\max} = 1.77$ and thus $\bar{\tau}_w$ will never reach the interface strength as predicted by the self-similar solution (Andrews, 1976; Burridge, 1973). Thus, no supershear transition can occur at any crack length for this setup. $\bar{\tau}_w$ has a central role in the dynamic crack propagation and underlines the non-steady nature of the observed phenomena.

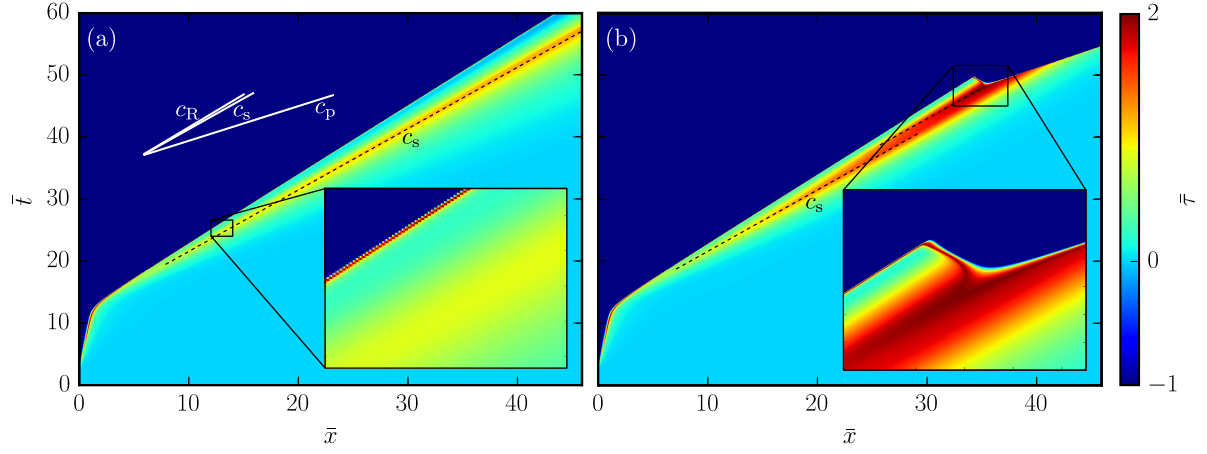


Figure 3.2: Dynamic mode II crack propagation for $S = 2 > S_{\max}$: space-time diagram of normalized tangential traction at frictional interface $\bar{\tau}$. The fractured zone corresponds to the area where $\bar{\tau}_r = -1$ (dark blue). (a) Homogeneous reference case. As the seed crack reaches $\bar{x} = 1$ it becomes unstable and accelerates towards c_R . A shear stress peak propagates ahead of the rupture front (indicated by dashed black line). (Inset) Close up on process zone at the propagating front. (b) Heterogeneous reference case: $c_s^h/c_s = 0.7$, $\bar{h}_1 = 4$ and $\bar{h}_2 = 10$. Similar to (a) a shear stress peak propagates ahead of the main rupture. Its amplitude grows quicker than in the homogeneous case and reaches the interface strength at $\bar{x} = 34.9$ (inset). A secondary rupture is nucleated and transition to supershear speed occurs.

Figure 3.2 (b) presents the propagation of a shear crack in a heterogeneous setup. Aside from the inclusion, which is characterized by $\bar{h}_1 = 4$, $\bar{h}_2 = 10$ and $c_s^h/c_s = 0.7$, the setup corresponds exactly to the homogeneous reference case shown in Figure 3.2 (a). This illustrative heterogeneous case is representative for inclusions satisfying $\bar{h}_1 > 2$, $\bar{h}_2 \gg \bar{h}_1$ and $c_s^h/c_s < 1$. Up until position $\bar{x} \approx 10$ the rupture dynamics are equivalent for the homogeneous and the heterogeneous cases. Beyond this point, $\bar{\tau}_w$ presents a higher growth rate of its amplitude in a heterogeneous setup. At $\bar{x} = 34.9$ it reaches the interface strength $\bar{\tau}_w = S$ and nucleates a secondary rupture in front of the main crack (see also inset Figure 3.2 b). The secondary crack propagates immediately at supershear speed.

Nucleation of the secondary crack needs to be sustained until it reaches a critical length, which is friction-law dependent (Dunham, 2007). A single supershear crack is formed through the merging of the primary and secondary cracks. This transition mechanism is similar to the Burridge-Andrews mechanism (Burridge, 1973; Andrews, 1976). However, it occurs under particularly low pre-stress $S > S_{\max}$, for which no transition would occur in a homogeneous setup. The favorable effect of the off-fault heterogeneities is thus the cause for supershear transition.

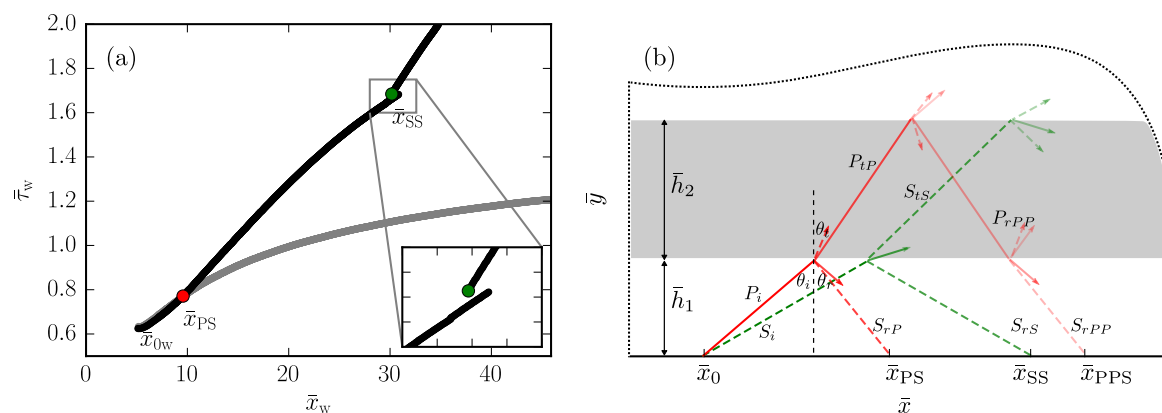


Figure 3.3: Effect of reflected waves on dynamic crack propagation and supershear transition. (a) Shear stress peak $\bar{\tau}_w$ as a function of normalized peak position \bar{x}_w . The homogeneous reference case is shown in gray and the heterogeneous reference case in black. The arrival of the reflected S_{rP} wave (red dot), also shown in (b), causes an increased growth rate of $\bar{\tau}_w$ in the heterogeneous case. A second increase, marked by a discontinuity in the position of the shear stress peak, corresponds to the arrival of the reflected S_{rS} wave (green dot). (b) Schematic representation of reflection and transmission of linear elastic waves of the three simplest paths. Dashed lines represent S-waves and continuous lines P-waves. Opacity illustrates the decreased amplitude of the reflected and transmitted waves. The arrival of reflected P-waves at the interface is not shown since no considerable effect has been observed in present simulations, see (a).

As illustrated in Figure 3.2, supershear transition can occur in the heterogeneous case because of a higher growth rate of $\bar{\tau}_w$. In Figure 3.3, we compare $\bar{\tau}_w$ for both cases. The reported $\bar{\tau}_w$ is defined as the local maximum in tangential interface traction ahead of the rupture. Initially both cases result in the same growth, as was also observed in Figure 3.2. Beyond \bar{x}_{PS} , growth is accelerated through waves that are reflected at the inclusions. In the remaining part of this section we provide a qualitative description of the various waves affecting $\bar{\tau}_w$. In Section 3.3.2, a predictive model is developed and used for a quantitative study of the wave reflection mechanism.

When the shear crack becomes unstable, it emits dynamic waves into the surrounding medium (Figure 3.4). The origin of these waves, which is marked as \bar{x}_0 in Figure 3.3 (b), is discussed in Section 3.3.2. Any elastic wave (longitudinal or shear) reaching the boundary of the heterogeneity is transmitted and reflected as longitudinal and shear waves. The relevant angles θ are determined by Snell's law (Aki and Richards, 2009) as

$$\sin \theta_i/c_i = \sin \theta_r/c_r = \sin \theta_t/c_t \quad (3.5)$$

where the subscript i, r and t represents the incident, reflected and transmitted waves, respectively. The first wave arriving at the interface is the P-wave reflection of the P-wave. However, we do not observe any relevant effects on the shear stresses along the interface (see Figure 3.3 (a) $\bar{x}_w < 10$). Therefore, we focus on the effects of reflected S-waves. The first wave affecting $\bar{\tau}_w$ is the S-wave reflection of the P-wave, which starts modifying $\bar{\tau}_w$ starting from \bar{x}_{PS} (S_{rP} in Figure 3.3 b).

The second wave shown in Figure 3.3 (b) is the S_{rS} , which is the S-wave reflection of the S-wave. As this reflected wave propagates at the same speed, i.e., shear wave

speed, as the interface shear stress peak over its entire longer path (triangle inequality), it cannot reach $\bar{\tau}_w$. However, it is strong enough to cause a new shear stress peak ahead of the propagating rupture but behind the original stress peak. This is marked by the second black dashed line in Figure 3.2 (b) and is the cause for the jump in \bar{x}_w observed in Figure 3.3 (a) (inset). Another S-wave affecting $\bar{\tau}_w$ is the S_{rPP} , which is the P-wave that is transmitted as P-wave at the lower inclusion boundary, reflected as P-wave at the upper boundary and transmitted as a S-wave at the lower boundary again. For setups with $\bar{h}_2 \gg \bar{h}_1$ the effect of S_{rPP} reaches the interface only after supershear transition (see Section 3.3.4 for study of reflection at \bar{h}_2). Additional insights on shear stress transient can be gained by studies considering a slip pulse on bi-material interfaces (Weertman, 2014) and in low-velocity fault zones (Huang et al., 2014).

In addition to wave reflection, modified elasticity in the near-tip field can affect crack propagation and transition. However, for configurations with $\bar{h}_1 > 2$ the rupture dynamics is mainly affected by wave reflection at the inclusions. Examples with lower inclusion distances $\bar{h}_1 < 2$ present generally lower propagation speed due to lower effective stiffness, which is illustrated in more details in Section 3.3.3.

Figure 3.4 shows the strain field from the dynamic simulations at increasing crack lengths. The heterogeneities, being more compliant, present larger strain compared to the bulk. The crack tip is characterized by the dark blue lobe. The difference in $\bar{\tau}_w$ is clearly visible (snapshots 2 & 3 in Figure 3.4). Snapshot 4 right shows the rupture after supershear transition. In this case a S-wave Mach cone is trailing from the supershear crack tip. The Mach cone represents a discontinuity in the velocity field and transports

high particle velocities and stresses far away from the fault (Dunham and Archuleta, 2005). After supershear transition, a stress concentration is visible at the sub-Rayleigh front, as observed experimentally and numerically by Mello et al. (2016).

3.3.2 Insights into the wave reflection mechanisms

In the previous section, we described the wave reflections qualitatively and marked in Figure 3.3 (a) the arrival of reflected waves at the stress peak. Here, we develop a quantitative model, which enables us to specifically determine the effect of each incident wave. For simplicity, we reduce this model to reflections at the lower boundary of the inclusions (i.e., $h_2 = \infty$). The additional effects of the upper boundary are presented in the parametric study in Section 3.3.4.

Determining the position and time that a reflected wave starts to affect $\bar{\tau}_w$ depends on the geometry of their paths as well as the duration it takes them to follow this path. $\bar{\tau}_w$ propagates along the interface at shear wave speed. Its equation of motion, shown as black dashed line in Figure 3.5 (b), is given by

$$\bar{x}_w(t) = \bar{x}_{0w} + (\bar{t} - \bar{t}_{0w}) \quad (3.6)$$

where \bar{x}_{0w} and \bar{t}_{0w} represent the origin in space and time, respectively, of the shear stress peak. The physical origin of $\bar{\tau}_w$ is closely related to the acceleration of the rupture at the moment it becomes unstable, i.e., at approximately $\bar{x} = 1$ but is difficult to determine exactly as the crack grows and $\bar{\tau}_w$ has to build up. For this reason, we define the origin as $(\bar{x}_{0w}, \bar{t}_{0w}) = (5.21, 16.9)$, which is the first point where the shear stress peak is separated

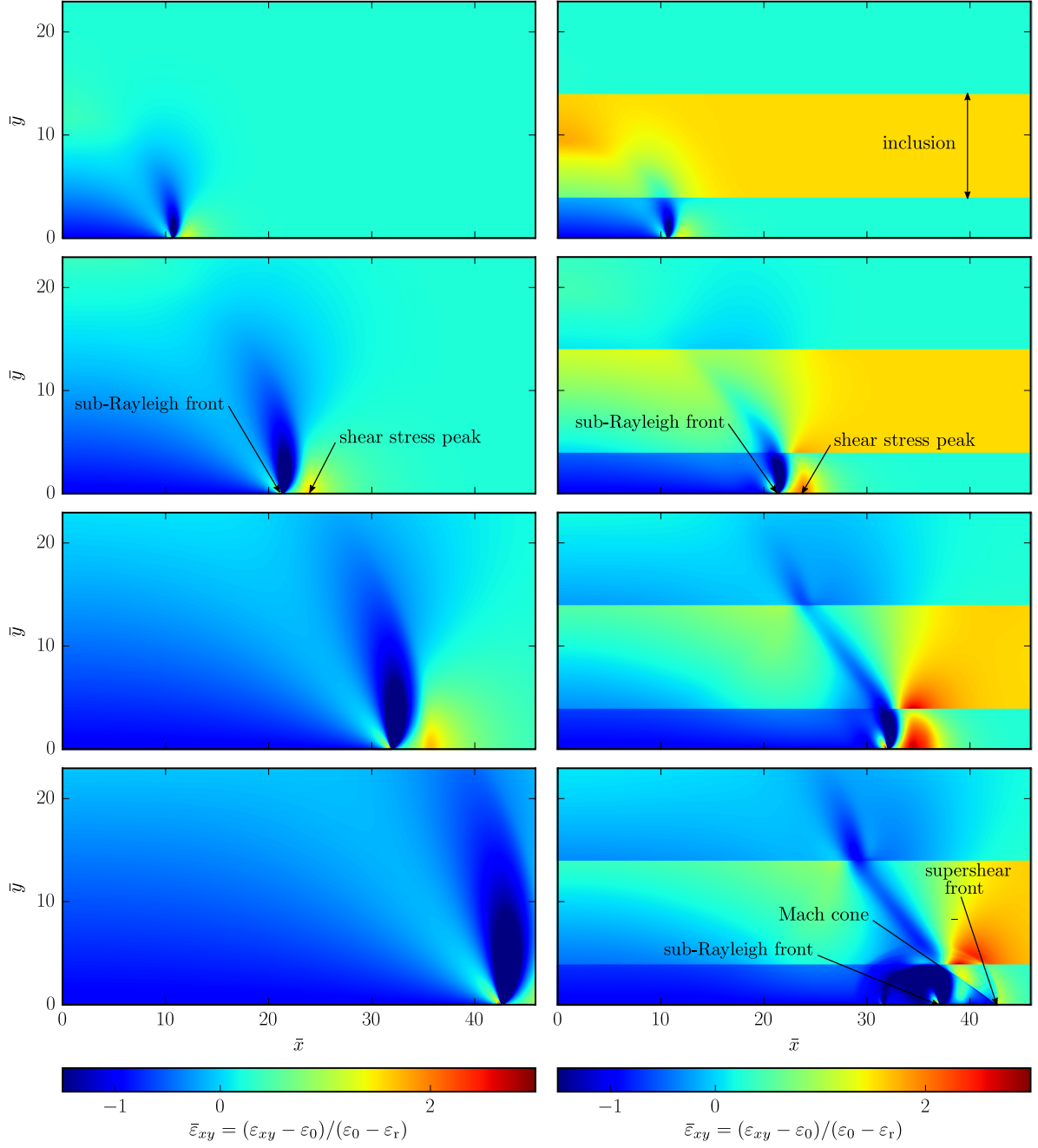


Figure 3.4: Dynamic mode II crack propagation for $S = 2 > S_{\max}$: normalized strain field $\bar{\varepsilon}_{xy}$ at time snapshots of equal crack lengths for homogeneous reference case (left) and heterogeneous reference case (right) with inclusion: $c_s^h/c_s = 0.7$, $\bar{h}_1 = 4$ and $\bar{h}_2 = 10$. Supershear propagation with S-wave Mach cone (bottom right).

enough from the crack tip singularity to be observable (see Figure 3.3 a). Even though this is not physically the origin of the shear stress peak, it is well defined, easily detectable and, as x_w scales with l_c , unique for all configurations.

The path of $\bar{\tau}_w$ along the interface encounters the path of the reflected S_{rP} wave, which we formulate as follows. We consider a cylindrical P-wave emitted from the crack tip at the instant when the dynamic fracture is onset. The origin of the considered wave is derived from the homogeneous reference case and corresponds to $\bar{x}_0 = 1$ and $\bar{t}_0 = 12.0$. The incident P-wavefront reaches the inclusion at position $(x_0 + x_i(t), h_1)$, where a P-wave and a S-wave are reflected. The travel time of the wavefront from its origin to the boundary of the inclusion is defined as t_i . The reflected S-wave reaches the fault at position $(x_{PS}(t), 0)$ after an additional time t_r . The length scale of the wave reflection problem h_1 leads to the following normalization: $\tilde{x} = x/h_1$ and $\tilde{t} = c_s t/h_1$. The projection of the incident and reflected waves path on the abscissa gives

$$\tilde{x}_{PS}(\tilde{t}) - \tilde{x}_0 = \tilde{x}_i + \tilde{x}_r \quad (3.7)$$

where \tilde{x}_i and \tilde{x}_r are the contribution of the incident and reflected waves, respectively. Similarly, the total travel time \tilde{t} , can be separated into the contribution from the incident wave \tilde{t}_i and reflected wave \tilde{t}_r :

$$\tilde{t} - \tilde{t}_0 = \tilde{t}_i + \tilde{t}_r \quad (3.8)$$

Note that the cylindrical nature of the emitted P-wave source implies that for all time $\tilde{t} > k + 1$ there will be a reflected S-wave reaching the frictional interface at position $\tilde{x}_{PS}(\tilde{t})$. From geometric considerations and using Snell's law (3.5), while assuming plane

wave reflection, a solution of the wave reflection problem can be derived and is given by:

$$\tilde{x}_{\text{PS}}(\tilde{t}) = \tilde{x}_0 + \sqrt{\tilde{t}_i^2/k^2 - 1} + \sqrt{(\tilde{t} - \tilde{t}_0 - \tilde{t}_i)^2 - 1} \quad (3.9)$$

where $\tilde{t}_i(\tilde{t})$ is the root of $F(\xi)$, such that $k \leq \xi < \tilde{t} - \tilde{t}_0 - 1$ and $\xi \in \mathbb{R}$. $F(\xi)$ is given by

$$F(\xi) = -\tilde{t} + \tilde{t}_0 + \xi + \frac{1}{\sqrt{1 - k^2 + k^4/\xi^2}}. \quad (3.10)$$

The complete derivation of (3.9) and (3.10) is given in Appendix 3.A.

The arrival time of the reflected S-wave from an incident P-wave S_{rP} along the interface is shown in Figure 3.5 (a). The normalized relation is general for any inclusion off-fault distance h_1 . Given that the propagation of the shear stress peak along the interface scales with the fracture-mechanics-related length scale l_c , we need to renormalize the solution of the reflected waves. The arrival time for various \bar{h}_1 is shown in Figure 3.5 (b). The positions at which the reflected waves start to affect the shear stress peak are marked by red dots and correspond to

$$\tilde{x}_{\text{PS}}(\tilde{t})h_1/l_c = \bar{x}_w(\tilde{t}). \quad (3.11)$$

As expected, the positions increase for increasing \bar{h}_1 . For $\bar{h}_1 \leq 2$, the reflected wavefront reaches the fault before the shear stress peak has separated from the crack singularity.

The effect of the reflected waves on the normalized growth of $\bar{\tau}_w$ is shown in Figure 3.6 (a) for numerical simulations with various off-fault inclusion distances \bar{h}_1 . The growth is initially equal for all shown cases, but once the first reflected wave reaches the interface, growth increases significantly. By comparing with the reference case, we measure the point of divergence (marked by red dots in Figure 3.6 a). The divergence

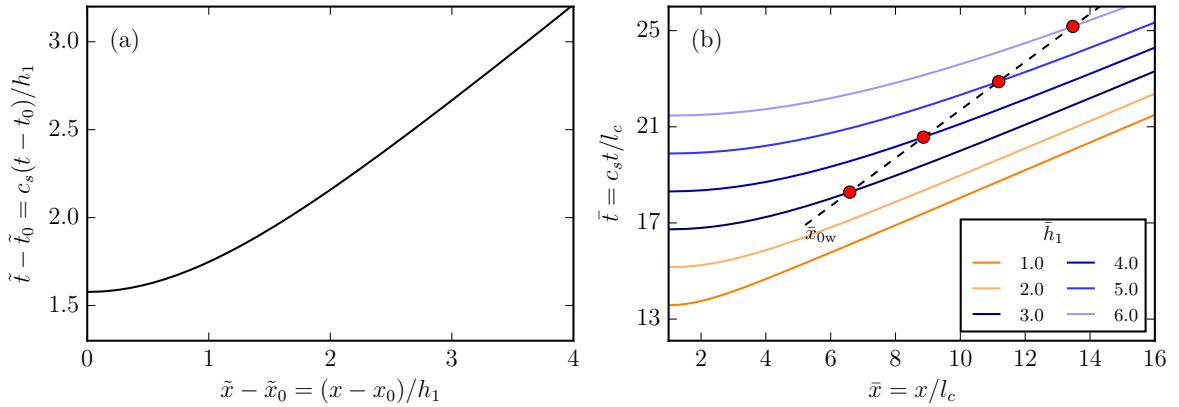


Figure 3.5: Wave reflection model for a S_{rP} wave. (a) Normalized time and position of reflected wavefront arriving at the frictional interface (3.9). (b) Arrival time and position of reflected wavefronts at the interface (3.9) normalized to fracture-mechanics related length scale l_c . Arrival times are shown (in color) for different inclusion distances \bar{h}_1 . The equation of motion of the shear stress peak (3.6) is depicted as dashed line. Red dots (3.11) indicate position where reflected waves start to affect the growth of the shear stress peak.

point moves away from the nucleation point with increasing \bar{h}_1 , which is intuitive and consistent with the analytical solution. At a later point, S_{rS} arrives at the interface and causes an additional increase in $\bar{\tau}_w$ (marked by green dots) as discussed in Section 3.3.1. Similar to the S_{rP} wave, the incident point of S_{rS} is further away from the origin as \bar{h}_1 increases.

How good is the estimate of the reflected wave arrival based on the analytical solution? The application of Snell's law for the reflection at the inclusion is based on the assumption of an incident plane wave, which is a simplification of the actual cylindrical wave. The validity of this assumptions improves with increasing radius of the wave, i.e., increasing \bar{h}_1 , and with shorter wavelengths of the incident wave. A comparison of the predicted

arrival position \bar{x}_{PS} (red dots in Figure 3.5 b) and the numerically measured values (red dots in Figure 3.6 a) is shown in Figure 3.6 (b) for $0.5 \leq c_s^h/c_s \leq 1.5$ and $3.0 \leq \bar{h}_1 \leq 6.0$. The prediction is quantitatively precise for all cases with a slight underestimation for $\bar{h}_1 = 3.0$. The plane wave assumption for small radii of the cylindrical wave is the probable cause for this deviation. Nevertheless, theory also predicts that the S_{rP} wave reaches the interface for $\bar{h}_1 \leq 2.0$ before the shear stress peak has separated from the crack singularity (Figure 3.5 b), which is numerically confirmed by the limiting case of $\bar{h}_1 = 3.0$ in Figure 3.6 (a), which is at the limit of detectability (see Figure 3.9 for cases with $\bar{h}_1 \leq 2.0$).

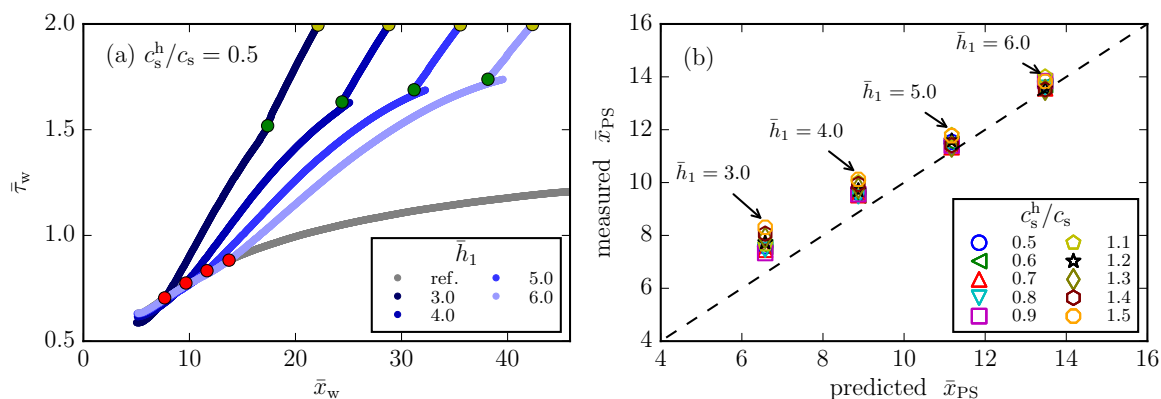


Figure 3.6: Effect of reflected waves at varying $\bar{y} = \pm\bar{h}_1$ on $\bar{\tau}_w$ and comparison with analytical model (3.11) for the position of S_{rP} wave arrival \bar{x}_{PS} . (a) Shear stress peak $\bar{\tau}_w$ as function of normalized position \bar{x}_w . Red dots indicate position where heterogeneous setup diverges from homogeneous reference case (gray). Divergence is defined as a relative 0.01% difference in peak stress value. Green dots indicate position of shear stress peak jump due to S_{rS} wave arrival. Transition to supershear $\bar{\tau}_w = S = 2.0$ is indicated by yellow dots. (b) Measured \bar{x}_{PS} (red dots in Figure 3.6 a) are compared with analytical prediction (3.11) (red dots in Figure 3.5 b) for inclusions with various c_s^h/c_s and $\bar{h}_1 = 3.0 - 6.0$.

For more insight into how the reflected waves affect the evolution of the shear stress peak, we plot in Figure 3.7 (a) the difference between the heterogeneous and homogeneous case $\bar{\tau}_w^h - \bar{\tau}_w^{\text{ref}}$ for the same simulations shown in Figure 3.6 (a) with renormalized position. The effect of the reflected waves appears to be independent of the off-fault distance within the renormalized reference frame. Small differences are observed for $\bar{h}_1 = 3.0$, which we attribute to the plane wave assumption that holds less for small \bar{h}_1 . The reflection model for linear elastic plane waves (Aki and Richards, 2009) states that the amplitude of the reflected wave, depends on the incident angle θ_i^{PS} and on c_s^h/c_s . Our simulations show that the θ_i^{PS} is only very weakly dependent on \bar{h}_1 and c_s^h/c_s with $\theta_i^{PS} \approx 56.3^\circ - 61.5^\circ$ for cases shown in Figure 3.7 (a) and (b). While the θ_i^{PS} remains constant for different c_s^h/c_s , the amplitude of the reflected wave is affected. Figure 3.7 (b) illustrates the relative shear stress peak growth for various material contrasts. Low-velocity inclusions lead to an increase in the shear stress peak due to the S_{rP} and S_{rS} waves, which promote early supershear transition. High-velocity inclusions, however, observe an initial decrease of the shear stress peak due to the S_{rP} wave before the S_{rS} wave arrives and increases the stress peak. Depending on the loading configuration, the effect of the opposed signs can either result in delaying or promoting early transition to supershear. Even though the shear stress peak growth shown in Figure 3.7 (b) is specifically for $\bar{h}_1 = 5.0$, the contribution of the S_{rP} wave is general for $\bar{h}_1 > 2.0$ as the θ_i^{PS} is insensitive to \bar{h}_1 . The influence of the S_{rS} (shown partially transparent in Figure 3.7 b), however, does depend on \bar{h}_1 and cannot be used as a generalization.

Note the generality of the derived wave reflection model. Given that the sub-Rayleigh crack dynamics, once expressed in dimensionless form (\bar{x}, \bar{t}) , are independent of S (Fre-

und, 1990; Svetlizky et al., 2016), the normalized wave reflection $\bar{\tau}_w^h - \bar{\tau}_w^{\text{ref}}$ (Figure 3.7 b) can be combined with $\bar{\tau}_w^{\text{ref}}$ (gray line in Figure 3.6 a) in order to infer supershear transition length for a variety of different setups, considering different loading conditions S , length-scales l_c and inclusion properties $c_s^h/c_s < 1$, \bar{h}_1 and $\bar{h}_2 = \infty$. A different imposed S would thus lead to a different scaling, given that the normalization (i.e., l_c) is related to S , but the dimensionless model remains valid and useful to determine x_{trans} .

The monotonic growth of $\bar{\tau}_w^h - \bar{\tau}_w^{\text{ref}}$ for cases of low-velocity inclusions (Figure 3.7 b) suggests that a maximum S for supershear transition in heterogeneous setups might not exist, even at moderate velocity contrast (e.g. 20%). Hence, the spatial extent in the fault-parallel direction would be the relevant limiting factor in geophysical settings.

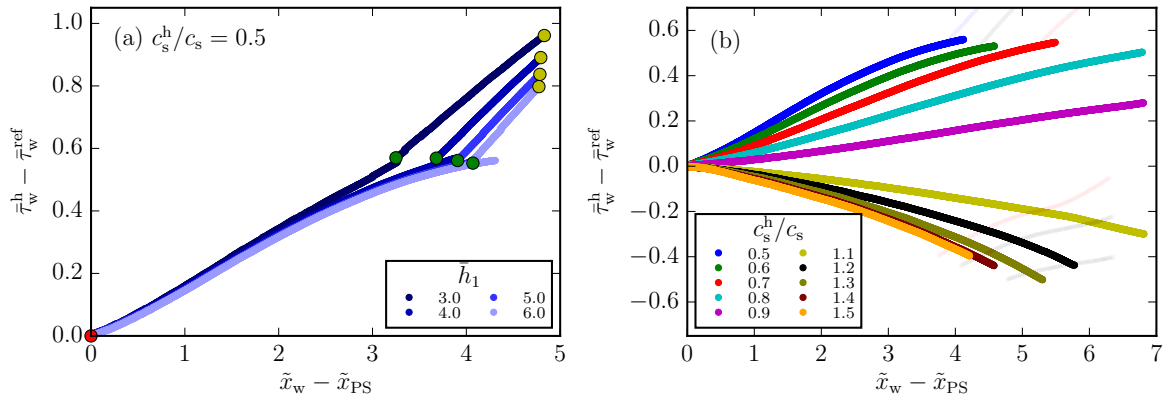


Figure 3.7: Effect of reflected waves at varying $\bar{y} = \pm \bar{h}_1$ and varying c_s^h/c_s on the shear stress peak at the fault. The shear stress peak difference to the homogeneous reference case $\bar{\tau}_w^h - \bar{\tau}_w^{ref}$ is shown with renormalized position $\tilde{x}_w - \tilde{x}_{PS}$. (a) Shear stress peak is shown for various \bar{h}_1 and $c_s^h/c_s = 0.5$. S_{rP} wave arrival is marked by red dot. Growth due to S_{rP} is independent of \bar{h}_1 (for $\bar{h}_1 > 2.0$). Arrival of S_{rS} is depicted by green dots. Yellow dots indicate transition to supershear. (b) Contribution of wave reflection on shear stress peak growth for various c_s^h/c_s and $\bar{h}_1 = 5.0$. Growth due to S_{rP} is, similarly to (a), independent of \bar{h}_1 (for $\bar{h}_1 > 2.0$) and is thus representative for various \bar{h}_1 . Curves are partially transparent beyond the arrival of the S_{rS} wave because growth is not independent on \bar{h}_1 for this part.

3.3.3 Parameter study $\bar{h}_2 = \infty$: effect of wave reflection at closer boundary of inclusion

We investigate the transition position for setups with $S = 2.0$, $\bar{h}_2 = \infty$ and varying c_s^h/c_s and \bar{h}_1 by performing a parameter study. The results of dynamic simulations are shown in dimensionless parameter space for low-velocity and high-velocity inclusions in Figure 3.8 and 3.10, respectively, where supershear transition and transition length vary as a function of c_s^h/c_s and \bar{h}_1 . In this work, we focus on the mechanism leading to the nucleation of the secondary rupture. We define the location of supershear transition \bar{x}_{trans} as the position where $\bar{\tau}_w$ reaches $\bar{\tau}_p \equiv S$.

Low-velocity inclusions with $\bar{h}_2 = \infty$

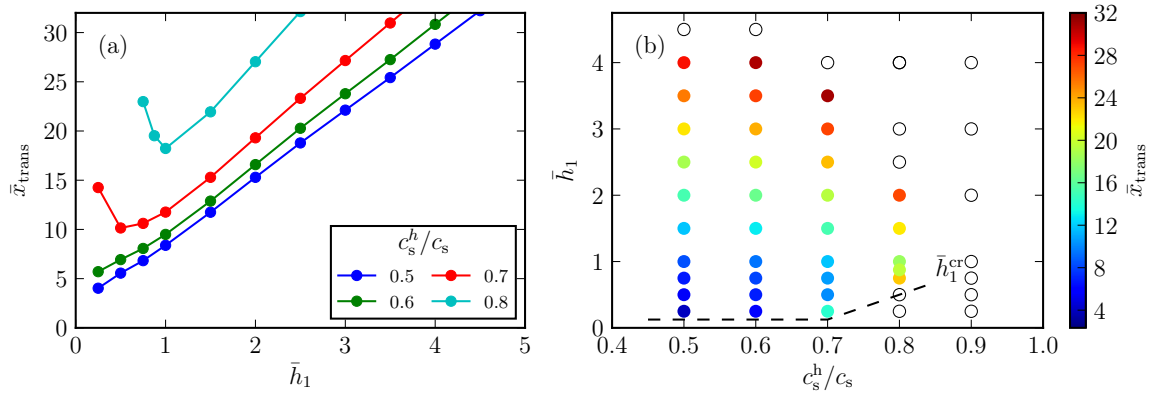


Figure 3.8: Influence of $c_s^h/c_s < 1$ and \bar{h}_1 on \bar{x}_{trans} for $S = 2.0$ and $\bar{h}_2 = \infty$. Each point represents a dynamic simulation with domain size $\bar{x}_{\text{max}} = 32$. (a) \bar{x}_{trans} is shown as a function of \bar{h}_1 . (b) \bar{x}_{trans} (color) is shown as function of c_s^h/c_s and \bar{h}_1 . Blank dots show simulation without supershear transition.

Figure 3.8 (a) shows results of a parameter study for low-velocity inclusions $c_s^h/c_s < 1$. Relevant velocity contrast at seismogenic depth are up to 20% (Tape et al., 2010; Allam et al., 2014; Zigone et al., 2015), for generality, stronger velocity contrasts are included. For a given c_s^h/c_s and $\bar{h}_1 \geq 2$, \bar{x}_{trans} is a linear function of \bar{h}_1 . Simulations for $\bar{h}_1 = 5, 6$ have been run on larger domains and confirm the linear trend, which is intrinsic to the wave reflection model. For $\bar{h}_1 < 2$, however, the linear trend is not maintained and longer \bar{x}_{trans} are observed. This can be explained by the interaction between the crack propagation speed, the shear stress peak growth and the wave reflection. For cases with inclusions particularly close to the fault, a reduced effective stiffness prevents the crack to approach the Rayleigh wave speed of the bulk, as shown in Figure 3.9 (b), and limits its propagation velocity at an effective Rayleigh wave speed of the heterogeneous setup. This is similar to lower propagation velocities observed by Huang and Ampuero (2011) in low-velocity fault zones. Simultaneously, when $\bar{h}_1 < 1$ the critical nucleation length is also decreased, but only slightly.

As a consequence of low-velocity inclusions close to the interface, two competing mechanisms affect the growth of the shear stress peak. While the lower effective stiffness leads to less released potential energy and thus lower growth, wave reflection at the inclusion increases the growth. This is well observed for $\bar{h}_1 = 0.25, 0.5$ in Figure 3.9 (a), where initial growth is considerably increased due to reflected waves but much lower growth occurs for $\bar{x}_w > 10$ due to lower effective stiffness. The effect of the reduced effective stiffness becomes negligible for setups with $\bar{h}_1 \geq 2$, as can be observed by the rupture speed in Figure 3.9 (b) that follows the linear elastic fracture mechanics prediction (Freund, 1990; Svetlizky et al., 2017) based on the bulk material properties. This is

consistent with observations based on the analytical model in Section 3.3.2. The effect of the inclusion proximity on the potential energy, affecting dynamic fracture, depends on the wavelength of the emitted dynamic source. This effect could be addressed in a perspective of dynamic homogenization and are topics of future work.

Figure 3.8 (b) shows the results of the parameter study in a dimensionless parameter space with simulations presenting sub-Rayleigh propagation as blank dots. For the considered domain size, supershear transition (color dots) occurs for $\bar{h}_1 > \bar{h}_1^{\text{cr}}$ and $c_s^{\text{h}}/c_s < 0.9$. Transition length increases for increasing \bar{h}_1 and c_s^{h}/c_s and the upper limit of the supershear region is due to finite domain size \bar{x}_{max} . Therefore, supershear transition is likely to occur for all $\bar{h}_1 > \bar{h}_1^{\text{cr}}$. At the lower boundary of the supershear region in Figure 3.8 (b), we observe either transition at short propagation distances (just above \bar{h}_1^{cr}) or no transition. This could mistakenly be interpreted as a physical limitation to potential supershear transition in this sub-domain. As it can be seen for $c_s^{\text{h}}/c_s = 0.7, 0.8$ in Figure 3.8 (a), the slope of \bar{x}_{trans} for varying \bar{h}_1 is steep and supershear transition could still occur for lower \bar{h}_1 but beyond the simulated domain. The reduced shear stress peak growth observed for $\bar{h}_1 = 0.25, 0.5$ in Figure 3.9 (a) does not necessarily mean that supershear transition will not occur at greater distances. Thus, our simulations do not suggest that \bar{h}_1^{cr} represents a physical limitation to supershear transition.

High-velocity inclusions with $\bar{h}_2 = \infty$, i.e. low-velocity fault zone

Figure 3.10 shows results of parameter study for high-velocity inclusions $c_s^{\text{h}}/c_s > 1$ and $\bar{h}_2 = \infty$, which is equivalent to setups of low-velocity fault zones (where the fracture

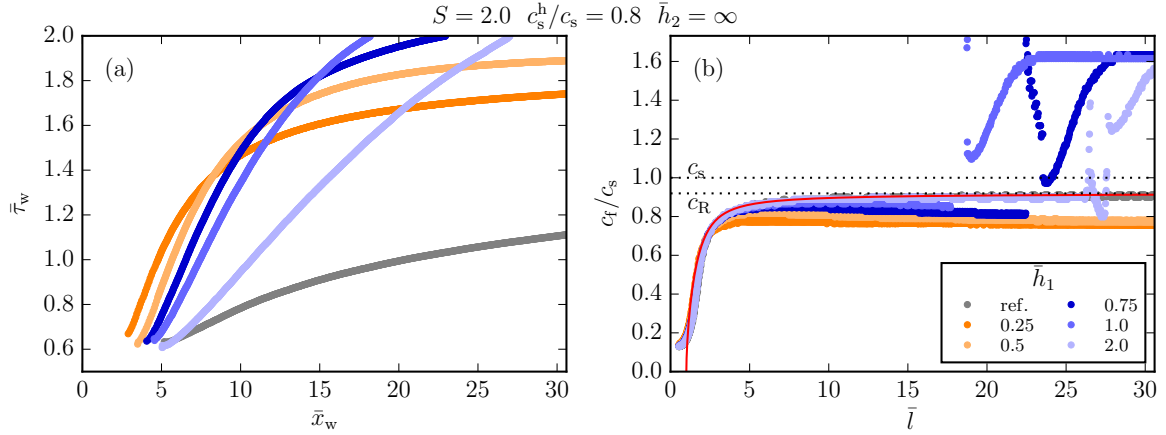


Figure 3.9: Effect of low-velocity inclusions near the interface with $S = 2.0$, $c_s^h/c_s = 0.8$, $\bar{h}_2 = \infty$ and varying \bar{h}_1 . Reference homogeneous case is shown in gray. (a) $\bar{\tau}_w(\bar{x}_w)$ reveals monotonically increasing $\bar{\tau}_w$ for all \bar{h}_1 . (b) Normalized crack propagation velocity as function of normalized crack length \bar{l} shows decreased velocities for $\bar{h}_1 \leq 1$. Sub-Rayleigh equation of motion for homogeneous reference case is shown as red line.

propagates within the more compliant medium) as considered in previous studies by Huang and Ampuero (2011); Huang et al. (2014, 2016). Material contrast relevant at seismogenic conditions can reach 60% (Huang et al., 2014). For consistency with the previous part, we consider velocity contrast up to 50%.

Supershear transition occurs for inclusions located relatively close to the frictional interface $\bar{h}_1 < 2.0$. Transition position for a given c_s^h/c_s increases with \bar{h}_1 and follows a non-linear trend (Figure 3.10 a). After the transition, crack propagation approaches c_p of the material embedding the fault. Generally, for high-velocity inclusions an inverse phenomenon to the one observed for low-velocity inclusions occurs: more potential energy can be released to the crack tip due to the high stiffness of the inclusion, while at the same time the reflection of negative $S_{r,P}$ waves decreases $\bar{\tau}_w$, as shown in Figure 3.7 (b).

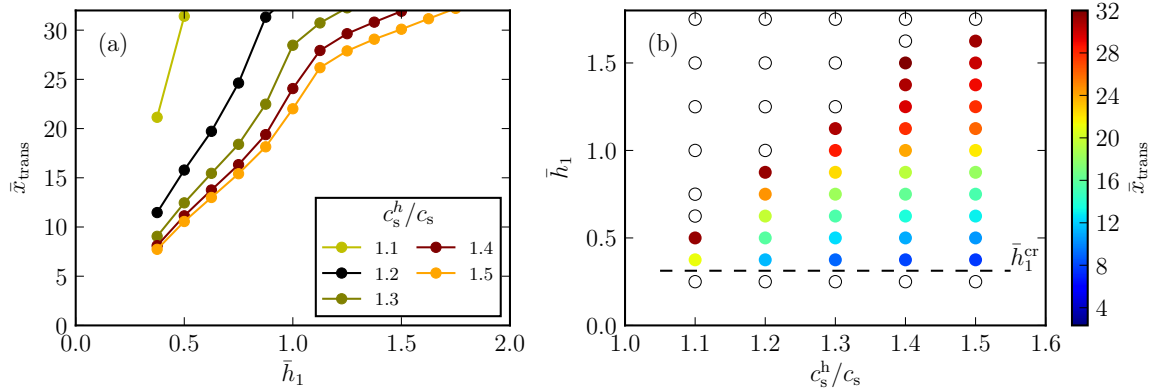


Figure 3.10: Influence of $c_s^h/c_s > 1$ and \bar{h}_1 on supershear transition for $S = 2.0$ and $\bar{h}_2 = \infty$. (a) $\bar{x}_{\text{trans}}(\bar{h}_1)$ reveals nonlinear trend. (b) \bar{x}_{trans} (color) is shown in dimensionless parameter space as function of c_s^h/c_s and \bar{h}_1 . Blank dots show simulations without transition. For $\bar{h}_1 < \bar{h}_1^{\text{cr}}$, crack propagation exceeds the Rayleigh wave speed of the bulk but not the one of the inclusion.

The effect of the equivalent Rayleigh wave speed (which is greater than the Rayleigh wave speed of the bulk) causes a faster acceleration, up to the point that for $\bar{h}_1 = 0.25 < \bar{h}_1^{\text{cr}}$ and $c_s^h/c_s > 1.1$ the crack propagation speed exceeds c_R by continuously accelerating through the energetically inadmissible domain for homogeneous setups $c_R < c_f < c_s$. However, it never exceeds c_R^h and no Burridge-Andrews mechanism is observed. This represents a case ($\bar{h}_1 < \bar{h}_1^{\text{cr}}$), where crack propagation is considered supershear for the bulk material and sub-Rayleigh for the inclusion and is similar to the observations on low-velocity fault zone by [Huang and Ampuero \(2011\)](#). Additionally, head-waves are present and affect the crack dynamics inducing oscillations depending on the length scale of the reflected waves interacting with the fracture mechanics related length scale, as discussed by [Huang et al. \(2014\)](#). The lack of supershear transitions for simulations with $\bar{h}_1 > 2.0$ (upper boundary of supershear domain in Figure 3.10 b) can be explained by considering $\bar{\tau}_w$ for

$\bar{h}_1 > 2.0$ shown in Figure 3.7 (b), where configurations with $c_s^h/c_s > 1$ show an initial decrease in shear stress peak due to the S_{rP} wave reflection and only after the arrival of S_{rS} the stress peak increases. Thus, for $\bar{h}_1 > 2.0$ and high-velocity inclusions supershear transition would occur beyond the simulated domain boundaries.

3.3.4 Parameter study $\bar{h}_2 < \infty$: effects of reflection at further boundary of inclusion

In the following section we introduce a further length scale to our setup by considering $\bar{h}_2 < \infty$. Based on the insights gained in the previous section we focus on the effect of the reflection at the further boundary of the inclusion at distance $\bar{h}_1 + \bar{h}_2$ from the frictional interface.

Figure 3.11 (a) shows the results of the parameter study for $S = 2.0$ and $c_s^h/c_s = 0.6$ with varying \bar{h}_1 and \bar{h}_2 . Sub-Rayleigh propagation is observed for $\bar{h}_2 < \bar{h}_2^{cr}$. No transition is observed for $\bar{h}_1 > 4.25$ because of limited domain size. For a given \bar{h}_1 , \bar{x}_{trans} decreases with increasing \bar{h}_2 until reaching a constant value for $\bar{h}_2 > \bar{h}_2^\infty$. Thus, setups with $\bar{h}_2 > \bar{h}_2^\infty$ behaves as if $\bar{h}_2 = \infty$, being equivalent to cases analyzed in Section 3.3.2. Similar behavior is observed for configurations with constant $\bar{h}_1 = 1$ and varying \bar{h}_2 and c_s^h/c_s shown in Figure 3.11 (b): for a given c_s^h/c_s , as \bar{h}_2 increases \bar{x}_{trans} decreases and converges to a constant value for $\bar{h}_2 > \bar{h}_2^\infty$. Figure 3.11 (c) shows \bar{x}_{trans} for the cases of a constant $\bar{h}_2 = 6$ and varying \bar{h}_1 and c_s^h/c_s . Notice the similarity with the previously discussed parameter study considering an $\bar{h}_2 = \infty$ (see Figure 3.8). In fact, for the

chosen $\bar{h}_2 = 6$, the infinite thickness assumption is valid for all $c_s^h/c_s \leq 0.7$. However, for $c_s^h/c_s = 0.8$ it is not the case ($\bar{h}_2 < \bar{h}_2^\infty$) and transition is delayed compared with the case of infinite \bar{h}_2 , discussed in Section 3.3.2.

Figure 3.12 shows the effects of $\bar{h}_2 < \bar{h}_2^\infty$ in more details for configurations with $c_s^h/c_s = 0.6$, $\bar{h}_1 = 2.0$. This gives further insights on the mechanisms behind the two boundaries \bar{h}_2^∞ and \bar{h}_2^{cr} observed in both Figure 3.11 (a) and (b). Figure 3.12 (a) shows the evolution of $\bar{\tau}_w$. For cases with $\bar{h}_2 \geq \bar{h}_2^\infty$ transition length has converged to values observed in the infinite thickness configuration because the wavefronts reflected at the further boundary of the inclusion reach the frictional interface only after transition has occurred. This underlines the importance and generality of the cases with $\bar{h}_2 = \infty$, discussed in Section 3.3.2, which are useful to describe setups with $\bar{h}_2 > \bar{h}_2^\infty$

When $\bar{h}_2 < \bar{h}_2^\infty$, $\bar{\tau}_w$ is decreased due to the negative effect of waves reflected at the further boundary of the inclusion, which cause a delay in supershear transition (see $\bar{h}_2 < 3 \approx \bar{h}_2^\infty$ on Figure 3.12). For cases where the inclusion thickness is below a critical value ($\bar{h}_2 = 0.5 < \bar{h}_2^{\text{cr}}$) transition does not occur anymore. As $\bar{\tau}_w$ reaches a local maximum at $\bar{x}_w = 28.2$ for $\bar{h}_2 = 0.5$, supershear transition might never occur for this setup. Instead, a propagation speed reduction is observed (see $\bar{h}_2 = 0.5$ at $\bar{l} = 20 - 30$ on Figure 3.12 b), possibly due to the arrival of a negative wave reflected at the further boundary of inclusion. Note that the observed phenomena (temporary speed reduction and concave $\bar{\tau}_w$) in Figure 3.12 with $c_s^h/c_s = 0.6$ and $\bar{h}_1 = 2.0$ are representative for all $\bar{h}_2 \lesssim \bar{h}_2^{\text{cr}}$ with any $c_s^h/c_s < 0.9$. Therefore, the effect of the heterogeneity thickness \bar{h}_2

and the resulting wave reflection at the further boundary of the inclusion, tends to delay $(\bar{h}_2^\infty < \bar{h}_2 < \bar{h}_2^{\text{cr}})$ or even prevent $(\bar{h}_2 < \bar{h}_2^{\text{cr}})$ supershear transition.

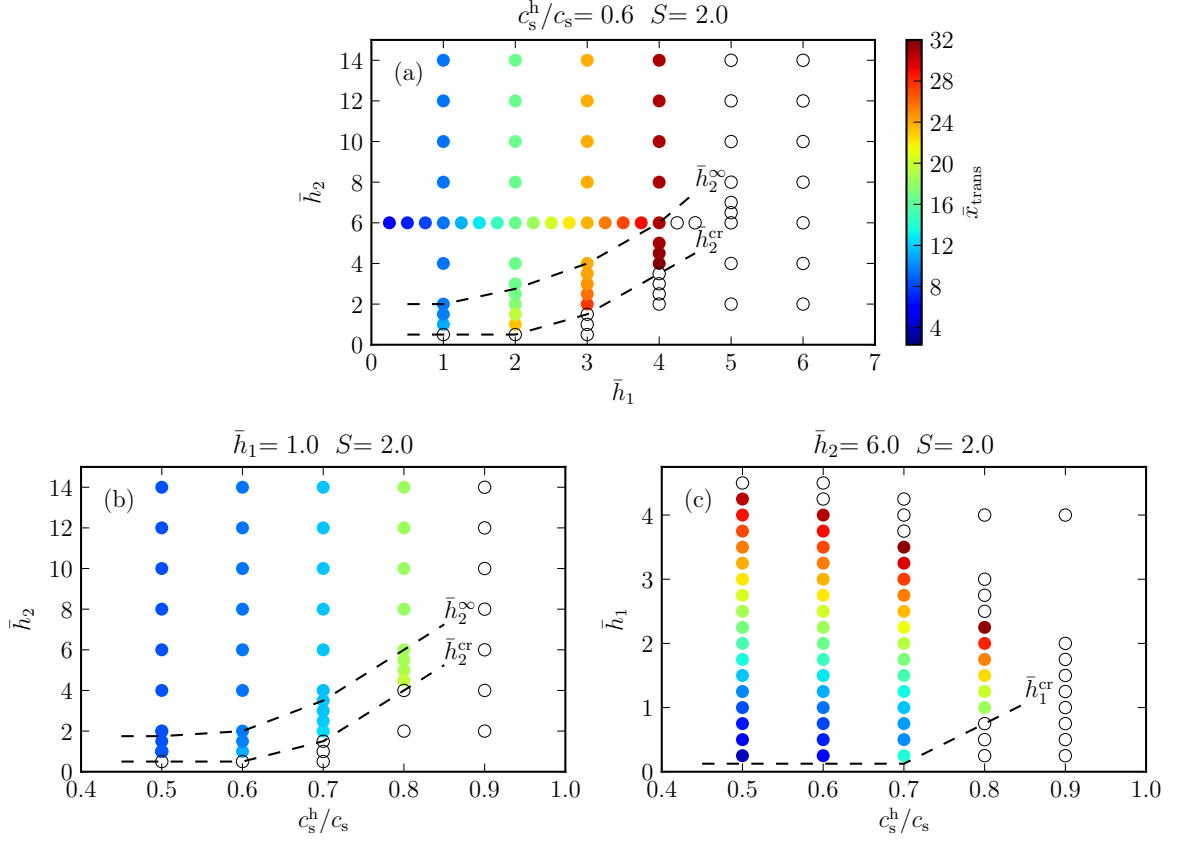


Figure 3.11: Various parameter studies considering $S = 2.0$ and $\bar{h}_2 < \infty$. \bar{x}_{trans} (color) is shown as function of \bar{h}_1 , \bar{h}_2 and c_s^h/c_s . Blank dots show simulations without supershear transition within simulated domain. (a) Parameter study $S = 2.0$, $c_s^h/c_s = 0.6$ with varying \bar{h}_1 and \bar{h}_2 . For a given \bar{h}_1 , \bar{x}_{trans} is constant for $\bar{h}_2 > \bar{h}_2^{\infty}$ and is equivalent to setups $\bar{h}_2 = \infty$ studied in Section 3.3.2. \bar{x}_{trans} increases as $\bar{h}_2^{\infty} > \bar{h}_2 > \bar{h}_2^{\text{cr}}$. (b) Parameter study $S = 2.0$, $\bar{h}_1 = 1$ with varying c_s^h/c_s and \bar{h}_2 . Similarly as in (a) \bar{x}_{trans} increases as $\bar{h}_2^{\text{cr}} < \bar{h}_2 < \bar{h}_2^{\infty}$ and converges to a constant value for $\bar{h}_2 > \bar{h}_2^{\infty}$. (c) Parameter study $S = 2.0$, $\bar{h}_2 = 6.0$ with varying c_s^h/c_s and \bar{h}_1 . For $c_s^h/c_s \leq 0.7$ results are comparable to the configuration with $\bar{h}_2 = \infty$. For $c_s^h/c_s = 0.8$ they differ from the case $\bar{h}_2 = \infty$ (see Figure 3.8).

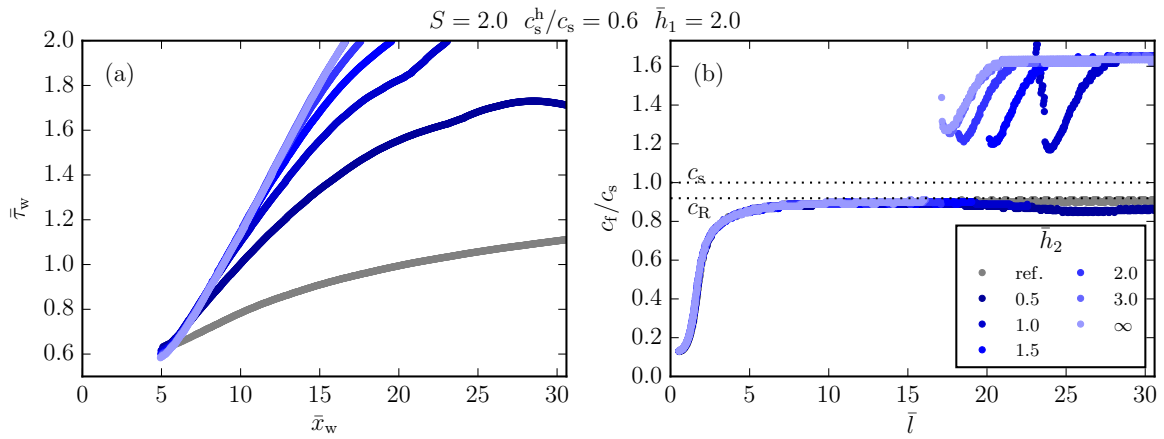


Figure 3.12: Effect of thin inclusion on shear stress peak and crack propagation. (a) $\bar{\tau}_w$ for $c_s^h/c_s = 0.6$ and $\bar{h}_1 = 2.0$. $\bar{\tau}_w$ is decreased due to wave reflection at further boundary of inclusion. (b) Crack propagation velocity c_f as function of crack length \bar{l} . Case on the threshold of supershear transition $\bar{h}_2 = 0.5 \lesssim \bar{h}_2^{st}$ features a decrease in propagation velocity at $\bar{l} = 20 - 30$.

3.4 Conclusion

We have investigated how material heterogeneities affect supershear transition mechanism for mode II ruptures using dynamic 2D finite-element simulations, with a linear slip-weakening friction law. Heterogeneous setups feature inclusions with contrasting stiffness compared to the bulk. The effect of geometry and velocity contrast of inclusions on the supershear transition mechanism has been analyzed within a wide parametric space.

Elastic wave reflection at the boundaries of the inclusions can enhance the shear stress peak preceding the propagating rupture and enable supershear transition even for cases of low loading condition $S > S_{\max}$, where in homogeneous uniform setups no transition would occur.

Two competing mechanisms have been identified. While reflected waves from the boundary of the low-velocity inclusions promote early supershear transition, lower effective stiffness reduces the available potential energy and delays transition. Inclusions that are relatively far from the interface only affect the shear stress peak through reflected waves. The reduced available potential energy for crack propagation becomes predominant for inclusions that are particularly close to the interface. This causes the crack propagation speed to approach an equivalent Rayleigh wave speed.

For high-velocity inclusions the same phenomena are observed with inverted signs. For particularly close inclusions, higher available potential energy enhances acceleration and promotes supershear transition. For far inclusions, the effect of higher energy release rate is negligible and wave reflections are the key mechanisms to supershear transition.

While the arriving S_{rP} wave initially reduces the shear stress peak with a delaying effect on supershear transition, the arrival of the reflected S_{rS} increases shear stress peak growth and promotes transition.

The difference in shear stress peak can be described by a wave reflection model, which links the fracture-mechanics-related length scale l_c with the wave reflection at the closer inclusion boundary h_1 . This model is particularly accurate for far inclusions, which have negligible effects on the available potential energy and provides generalized shear stress peak growth due to reflected S_{rP} being independent of h_1 , allowing the prediction of supershear transition length for a variety of geometry and loading conditions. Wave reflection at the further boundary of low-velocity inclusions is shown to delay supershear transition position, and even prevent it completely if the inclusion thickness is smaller than a critical value. Setups with relatively important inclusion thickness are equivalent to configurations with infinite thickness.

The results of this study may provide a better physical insight into the supershear transition of earthquakes under heterogeneous conditions. Low-velocity inclusions at seismogenic depths as well as damaged fault zones of neighboring tectonic faults are two types of potential heterogeneities that could affect the transition. Our study suggests that supershear earthquakes are more likely to occur at faults with nearby low-velocity inclusions and may help explain the mechanics leading to the supershear earthquake at the Kunlun fault in 2001 (Bouchon and Vallée, 2003). Our simulation results and the proposed model provide an understanding of how reflected waves affect the shear stress peak ahead of the earthquake rupture and may help estimate the reduction of the

supershear transition length, which could lead to a better evaluation of the potential for supershear earthquakes in the presence of low-velocity inclusions.

APPENDIX

3.A Reflected S_{rP} wave: derivation of analytical model

We derive the wave reflection model for an incident P-wave and reflected S-wave using the normalization with respect to h_1 , which is the length scale of the wave reflection problem. From geometrical and kinematic considerations the travel path and travel time of the incident and reflected wavefronts are linked by the following relations:

$$\tilde{x}_i^2 + 1 = \tilde{t}_i^2/k^2 \quad (3.12)$$

$$\tilde{x}_r^2 + 1 = \tilde{t}_r^2 \quad (3.13)$$

where \tilde{x}_i and \tilde{x}_r are the projections of the incident and reflected waves paths on the abscissa, respectively, \tilde{t}_i and \tilde{t}_r are the travel times of the incident and reflected waves, respectively, and $k = c_s/c_p$.

The direction of the reflected wave-front is governed by Snell's law (3.5), which can be expressed in terms of travel time and path by applying trigonometric identities:

$$k^2 \frac{\tilde{x}_i}{\tilde{t}_i} = \frac{\tilde{x}_r}{\tilde{t}_r} . \quad (3.14)$$

This non-linear system describes the kinematics of the considered wave reflection. Substituting (3.14) into (3.13) yields

$$k^4 \frac{\tilde{t}_r^2}{\tilde{t}_i^2} \tilde{x}_i^2 + 1 = \tilde{t}_r^2 . \quad (3.15)$$

With (3.12) we can express \tilde{x}_i in terms of \tilde{t}_i and (3.15) becomes

$$k^4 \frac{\tilde{t}_r^2}{\tilde{t}_i^2} \left(\frac{\tilde{t}_i^2}{k^2} - 1 \right) + 1 = \tilde{t}_r^2 \quad (3.16)$$

and by rearranging we can express \tilde{t}_r as function of \tilde{t}_i

$$\tilde{t}_r = \frac{1}{\sqrt{1 - k^2 + k^4/\tilde{t}_i^2}} . \quad (3.17)$$

This result is substituted into (3.8), which yields

$$\tilde{t} = \tilde{t}_0 + \tilde{t}_i + \frac{1}{\sqrt{1 - k^2 + k^4/\tilde{t}_i^2}} . \quad (3.18)$$

Combining (3.7),(3.8) with (3.12) and (3.13) we find the following

$$\tilde{x}_{\text{PS}}(\tilde{t}) = \tilde{x}_0 + \sqrt{\tilde{t}_i^2/k^2 - 1} + \sqrt{(\tilde{t} - \tilde{t}_0 - \tilde{t}_i)^2 - 1} \quad (3.19)$$

where $\tilde{t}_i(\tilde{t})$ is the root of $F(\xi)$, such that $k \leq \xi < \tilde{t} - \tilde{t}_0 - 1$ and $\xi \in \mathbb{R}$. From (3.18) we derive

$$F(\xi) = -\tilde{t} + \tilde{t}_0 + \xi + \frac{1}{\sqrt{1 - k^2 + k^4/\xi^2}} . \quad (3.20)$$

CHAPTER 4

STOCHASTIC PROPERTIES OF STATIC FRICTION

This chapter is drawn from the following peer-reviewed journal article:

Albertini, G., Karrer, S., Grigoriu, M. D. and Kammer, D. S. (2021) , ‘Stochastic properties of static friction’, *Journal of the Mechanics and Physics of Solids* **147**, 104242.

The onset of frictional motion is mediated by rupture-like slip fronts, which nucleate locally and propagate eventually along the entire interface causing global sliding. The static friction coefficient is a macroscopic measure of the applied force at this particular instant when the frictional interface loses stability. However, experimental studies are known to present important scatter in the measurement of static friction; the origin of which remains unexplained. Here, we study the nucleation of local slip at interfaces with slip-weakening friction of random strength and analyze the resulting variability in the measured global strength. Using numerical simulations that solve the elastodynamic equations, we observe that multiple slip patches nucleate simultaneously, many of which are stable and grow only slowly, but one reaches a critical length and starts propagating dynamically. We show that a theoretical criterion based on a static equilibrium solution predicts quantitatively well the onset of frictional sliding. We develop an efficient Monte-Carlo model by adapting the theoretical criterion and study the variability in global strength distribution caused by the stochastic properties of local frictional strength. The results demonstrate that an increasing spatial correlation length on the

interface, representing geometric imperfections and roughness, causes lower global static friction. Conversely, smaller correlation length increases the macroscopic strength while its variability decreases. We further show that randomness in local friction properties is insufficient for the existence of systematic precursory slip events. Random or systematic non-uniformity in the driving force, such as potential energy or stress drop, is required for arrested slip fronts. Our model and observations provide a necessary framework for efficient stochastic analysis of macroscopic frictional strength and establish a fundamental basis for probabilistic design criteria for static friction.

Keywords: frictional strength, critical shear stress, critical nucleation length, random interface properties, homogenization.

4.1 Introduction

Static friction is the maximal shear load that can be applied to an interface between two solids before they start to slide over each other. The famous Coulomb friction law ([Amontons, 1699](#); [Coulomb, 1785](#); [Popova and Popov, 2015](#)) states that static friction is proportional to the normal load with the friction coefficient being the proportionality factor. The friction coefficient is generally reported as function of the contacting material pair, which is often misinterpreted as the friction coefficient being a material (pair) property. While proportionality of friction to normal load is mostly valid, the friction coefficient is geometry-dependent and thus varies for different experimental setups with the same material pair ([Ben-David and Fineberg, 2011](#)). The underlying cause for this observation is the mechanism governing the onset of frictional sliding, which has been shown to be a fracture-like phenomenon ([Svetlizky and Fineberg, 2014](#); [Kammer et al., 2015](#); [Svetlizky et al., 2020](#); [Rubino et al., 2017](#)). The geometry and deformability of the solids lead to a non-uniform stress state along the interface. As a consequence, local frictional strength is reached at a critical point and slip nucleation starts, from where it extends in the space-time domain – just like a crack – until the entire interface transitioned and global sliding occurs. This process is well-known in the earthquake mechanics and rock friction community ([Okubo and Dieterich, 1984](#); [Dieterich, 1992](#); [Dieterich and Kilgore, 1996](#); [McLaskey, 2019](#)) and shows clearly that the macroscopic friction coefficient does not provide a measure for the local friction coefficient (*i.e.*, the material property) if the sample is larger than a characteristic nucleation length. In such over-sized experiments,

the observed friction coefficient is directly affected by boundary conditions and, hence, presents a size effect.

Variations in the static friction force, however, do not only occur because of changes in the loading configuration. Experiments have shown that the measured friction force varies also from one experiment to another when the exact same setup and exact same specimens are used. For instance, [Rabinowicz \(1992\)](#) showed that the static friction coefficient of a gold-gold interface, measured by a tilting plane friction apparatus, varies from 0.32 to 0.80 for normal load 75 g. Similar but to a lesser extent, [Ben-David and Fineberg \(2011\)](#) also observed variations in the static friction coefficient of glassy polymers when the loading configuration was fixed.

While these variations are not often reported, they are an important factor in the absence of a complete and consistent theory for friction ([Spencer and Tysoe, 2015](#)). If (seemingly) equivalent experiments lead to a large range of observations without consistent trends, it is challenging to isolate the relevant from the irrelevant contributions and, therefore, nearly impossible to create a fundamental understanding of the underlying process. Even though the presence of these large variations has important implications for the study of friction, current knowledge about the origin and properties of these observed variations in macroscopic friction remains limited.

One possible origin is randomness in local friction properties. Interfaces have been shown to consist of an ensemble of discrete micro-contacts ([Bowden and Tabor, 1950](#); [Dieterich and Kilgore, 1994](#); [Sahli et al., 2018](#)), which are created by surface roughness ([Thomas, 1999](#); [Hinkle et al., 2020](#)) when two solids are brought into contact. This

naturally leads to a system with random character, where micro-contacts of random size are distributed randomly along the interface (Greenwood et al., 1966; Persson, 2001; Hyun and Robbins, 2007; Yastrebov et al., 2015). Since frictional strength is directly related to the cumulative contact area of these micro-contacts (Bowden and Tabor, 1950; Greenwood et al., 1966), and the micro-contacts are the result of random surface roughness, the local frictional strength is likely also random.

Surprisingly, the effect of interfacial randomness on friction remains largely unexplored. Most of previous work is focused on how (random) surface roughness is related to various friction phenomenology including rate-dependence (Li et al., 2013; Lyashenko et al., 2013), local pressure excursions within lubricated contact (Savio et al., 2016), chemical aging (Li et al., 2018), or the existence of static friction (Sokoloff, 2001). However, only few studies have considered how interfacial randomness causes variations in these observations. Ampuero et al. (2006) and Ripperger et al. (2007, 2008) analyzed the effect of stochastic initial stress heterogeneities on the critical load for earthquake ruptures, which are essentially localized slip events on tectonic faults. Further, Amon et al. (2017) showed that systems with a nonuniform initial stress state with long range coupling are characterized by two regimes: at low loading, small patches of the system undergo sliding in an uncorrelated fashion; at higher loading, instabilities occur at regular intervals over patches of increasing size – just like confined stick-slip events (Kammer et al., 2015; Bayart et al., 2016) – and eventually span the whole system. Geus et al. (2019) simulated interface asperities as an elasto-plastic continuum with randomness in its potential energy and show that the stress drop during a stick-slip cycle is a stochastic property which vanishes with increasing number of asperities. These results demonstrate

well the stochastic character of macroscopic friction due to random interface properties. However, a complete understanding of the effects of interfacial randomness on the variability of macroscopic static friction, *e.g.*, the friction coefficient, remains missing.

Here, we address this gap of knowledge and aim at a better understanding of the stochastic properties of static friction. We present a combined numerical and theoretical study that links randomness of local friction properties with observed variability in macroscopic strength. Using dynamic simulations, we will show that the macroscopic friction threshold is attained when a local slipping area, of which many can co-exist, reaches a critical length and nucleates the onset of friction. This nucleation patch becomes unstable and propagates across the entire interface causing global sliding. We will then show that a quasi-static equilibrium theory, which takes an integral form, predicts quantitatively well the critical stress level that causes nucleation of global sliding. Based on this theoretical model, we will develop fast and accurate Monte Carlo simulations using a Fourier representation of the integral equations, and demonstrate the extent of variability in macroscopic static friction based on random interface strength with various correlation lengths. Finally, we will show that a decreasing interfacial correlation length leads to higher macroscopic strength with decreased variability.

This paper is structured as follows. First, we provide a problem statement in [Sec. 4.2](#) including a description of the physical system, the stochastic properties, and our approach to generate random strength fields. In [Sec. 4.3](#), we present the numerical method used to simulate the onset of frictional sliding and compare simulation results of critical stress leading to global sliding with predictions based on a theoretical model. This model is then

used in an analytical Monte Carlo study, which is developed and presented in Sec. 4.4. The implications of our model assumptions as well as the model results are discussed in Sec. 4.5. Finally, we provide a conclusion in Sec. 4.6.

4.2 Problem Statement

In this section, we first provide a description of the physical problem that we consider throughout this paper. We then describe the stochastic properties of the strength profile along the interface and, finally, explain how we generate these random fields.

4.2.1 Physical Problem

We study the macroscopic strength of a frictional interface. Our objective is to provide a fundamental understanding of the effect of local variations in frictional strength on the macroscopic response. For this reason, we focus on the simplest possible problem – without oversimplifying the constitutive relations of the bulk and the interface. Specifically, we consider a two-dimensional (2D) in-plane system consisting of two semi-infinite elastic solids, as shown in Fig. 4.2.1a. The domain is infinite in the y direction and periodic in x with period L . Both materials have the same elastic properties.

We apply a uniform shear load $\tau_0(t)$ that increases quasi-statically with time (see Fig. 4.2.1b). Once the mean interfacial shear stress $\langle\tau\rangle(t) = \int_0^L \tau(x)/L dx$ reaches the macroscopic strength of the interface τ_{cr} , the interface starts to slide and the frictional

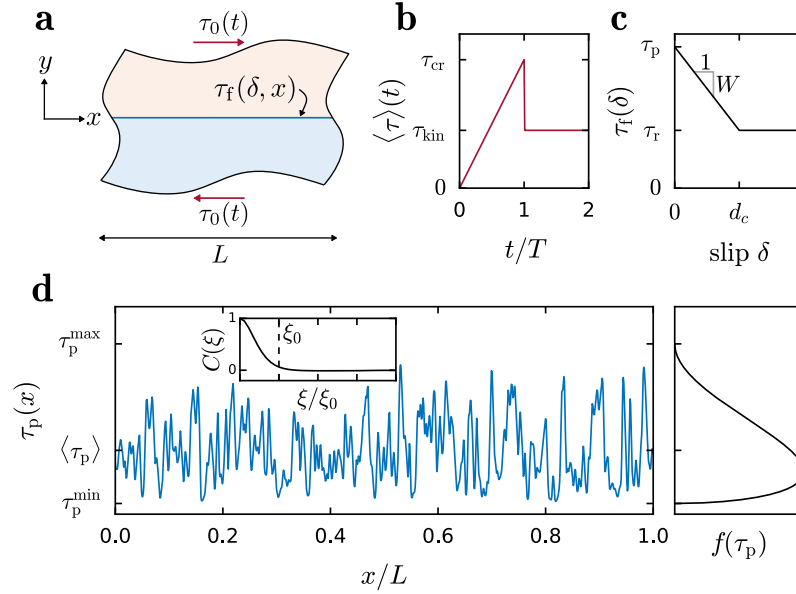


Figure 4.2.1: Problem statement. (a) A frictional interface (blue line) of strength $\tau_f(\delta, x)$ embedded within two semi-infinite elastic solids, which are periodic in x with period L and infinite in y . A uniform loading $\tau_0(t)$ is applied. (b) The mean interface frictional traction $\langle \tau \rangle(t)$ increases linearly with time t up to the onset of frictional motion when the stress drops from its critical value τ_{cr} to a kinetic level τ_{kin} . (c) The constitutive relation of the frictional interface is a linear slip-weakening law $\tau_f(\delta)$ with random peak strength $\tau_p(x)$ and constant weakening rate W (see Eq. 4.1). (d) $\tau_p(x)$ is a random field with spatial correlation $C(\xi)$ (inset) and probability density function $f(\tau_p)$ (right).

strength suddenly reduces to its kinetic level τ_{kin} . This observed reduction in shear stress is typically associated with friction-weakening processes, which may depend on various properties, such as slip, slip rate, and interface state. The critical shear stress τ_{cr} , if divided by the contact pressure, corresponds to the static macroscopic friction coefficient. Similarly, τ_{kin} is proportional to the kinetic friction coefficient.

These macroscopic observations depend on the local interface properties, which are the peak strength $\tau_p(x)$, and residual strength $\tau_r(x)$. As we will show, the local properties are generally different from the macroscopic properties; particularly, in the case of non-uniform stress or strength. While rate-and-state friction laws (Dieterich, 1979; Ruina, 1983; Rice and Ruina, 1983) provide a generally more realistic description of the evolution of local frictional strength during nucleation, we apply here a more simple linear slip-weakening law. This allows us to predefine important quantities, such as the weakening rate, and, hence, enables us to study unequivocally the effects of randomness on the macroscopic friction. The implications of this simplification are discussed in Sec. 4.5. The linear slip-weakening law, which is shown in Fig. 4.2.1c and is given by

$$\tau_f(\delta) = \tau_r + W(d_c - \delta)H(d_c - \delta) , \quad (4.1)$$

where $\delta(x)$ is local slip, $d_c(x)$ is a characteristic length scale, and $W(x) = (\tau_p(x) - \tau_r(x))/d_c(x)$ is the weakening rate. $H(\cdot)$ is the Heaviside function. In a symmetric system, this friction law is equivalent to $\tau_f(\delta) = \mu(\delta)p$, where $\mu(\delta) = \mu_k + H(d_c - \delta)(\mu_s - \mu_k)/d_c$, because contact pressure p remains constant over time. Hence, we find local properties of $\tau_r = \mu_k p$ and $\tau_p = \mu_s p$.

We consider a heterogeneous system with local peak strength $\tau_p(x)$ being a random field, as further described in Sec. 4.2.2. To reduce complexity of the problem, we assume uniform residual strength¹ $\partial_x \tau_r = 0$ and uniform weakening rate $\partial_x W = 0$. The variation in local peak strength is thought to represent possible heterogeneity in the material, but also the effect of surface roughness, which leads to a real contact area that consists of

¹We use ∂_i as short notation for partial derivative with respect to i .

an ensemble of discrete contact points with varying properties. The implications of this approach will be discussed in depth in Sec. 4.5.

4.2.2 Stochastic Properties of Frictional Interface

The local peak strength $\tau_p(x)$ is modeled as a stationary non-Gaussian random field with specified cumulative distribution function $F(\tau_p)$ and corresponding probability density $f(\tau_p)$, as shown in Fig. 4.2.1d. The random field is defined by the nonlinear mapping

$$\tau_p(x) = F^{-1}\left(\Phi(z(x))\right), \quad (4.2)$$

where $z(x)$ is Gaussian with zero mean and unit variance and Φ its cumulative distribution, depicted in Fig. 4.2.2a-left. F and Φ are monotonic by definition, so their inverse exist, which can be used to prove that $P(\tau_p(x) \leq \tau) = F(\tau)$. Further, with τ_p being the local peak strength of the interface, it needs to satisfy some physical requirements. First, the peak strength is always higher than the residual strength, *i.e.*, $\tau_p^{\min} \geq \tau_r$. Second, its maximum value is limited by the material properties. For this reason, we require that $\tau_p \in (\tau_p^{\min}, \tau_p^{\max})$, which we achieve by setting $F(\tau_p)$ as a Beta cumulative distribution function (see Fig. 4.2.2a-right).

The spatial distribution of $z(x)$ is specified by its power spectral density $g(k)$, which corresponds to the Fourier transform of the correlation function $C_z(\xi)$, *i.e.*,

$$g(k) \equiv \int_{-\infty}^{+\infty} C_z(\xi) e^{-ik\xi} d\xi, \quad (4.3)$$

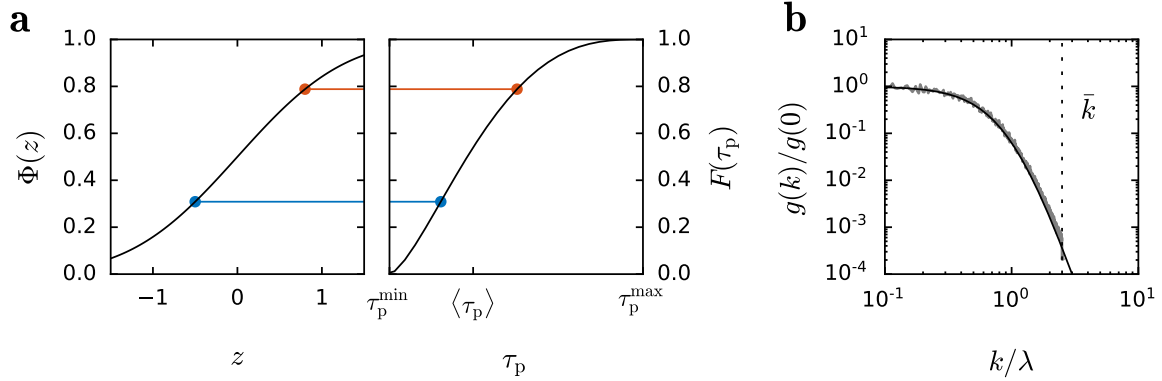


Figure 4.2.2: Stochastic properties of the random peak strength field $\tau_p(x)$. (a) The random variable τ_p is generated by applying a nonlinear mapping $F^{-1} \circ \Phi(x)$ (Eq. 4.2) onto the Gaussian random variable z . Two colored dots inked by a line represent a (z, τ_p) pair with equal cumulative density $F(\tau_p) = \Phi(z)$, which is the criterion imposed by the nonlinear mapping. (b) Black line is the normalized input spectral density function $g(k)/g(0)$ (Eq. 4.4). Gray line is the empirical spectral density function of $\tau_p(x)$. \bar{k} is the truncation frequency and $\lambda = 2\pi/\xi_0$ is the cutoff frequency.

where k is the angular wave number. We assume that $z(x)$ has a power spectral density

$$g(k) \propto (k^2 + \lambda^2)^{-4}, \quad (4.4)$$

where λ is the cutoff frequency, above which the spectral density decays as a power law $\sim k^{-8}$ (see Fig. 4.2.2b). The correlation length ξ_0 is a measure of memory of the random field; the longer ξ_0 the longer the memory. ξ_0 is inversely proportional to λ , and we define² it as $\xi_0 = 2\pi/\lambda$. The assumption of using this specific spectral density and probability distribution are discussed in Sec. 4.5.3.

²The correlation length does not have a precise definition. An alternative definition is $C(\xi_0) = \exp(-1)$.

4.2.3 Random Field Samples Generation

The samples of random field $\tau_p(x)$ are generated as follows. First, the Gaussian random field $z(x)$ is generated using a spectral representation

$$z(x) = \sum_{j=1}^J \sigma_j (A_j \cos(k_j x) + B_j \sin(k_j x)), \quad (4.5)$$

where A_j and B_j are independent Gaussian random variables with zero mean and unit variance and modal angular wave-number is $k_j = 2\pi j/L$. The fundamental wavelength of the field $2\pi/k_1 = L$ is chosen such that it corresponds to the domain size L , which implies that $z(x)$ is periodic over L , and so is $\tau_p(x)$. The modal variance $\sigma_j^2 \propto g(k_j)$ corresponds to the discrete spectral density, which is normalized to assure that z has unit variance

$$\sigma_j^2 = \frac{g(k_j)}{\sum_{j=1}^J g(k_j)}. \quad (4.6)$$

Due to the discrete representation of $z(x)$, we apply a truncation frequency that is considerably larger than the cutoff frequency $\bar{k} \equiv k_J = 2.5\lambda$. This ensures that most of the spectral power is preserved:

$$\frac{\int_0^{\bar{k}} g(k) dk}{\int_0^{\infty} g(k) dk} \approx 0.9997 \quad (4.7)$$

Further increase in \bar{k} would include additional high frequency modes but with negligible amplitudes. Finally, once $z(x)$ has been generated, we apply the nonlinear mapping $F^{-1} \circ \Phi$ (Eq. 4.2 and visualized in Fig. 4.2.2a) and obtain the random field $\tau_p(x)$. Fig. 4.2.1d shows a sample of $\tau_p(x)$ generated using the described procedure with corresponding correlation function and probability density. Since the correlation function of z is positive, $C_z(\xi) > 0$, it is not greatly affected by the nonlinear mapping $F^{-1} \circ \Phi$ and $C_z(\xi) \approx C_{\tau_p}(\xi)$

(Grigoriu, 1995, p.48) and, therefore, the empirical spectral density of $\tau_p(x)$ corresponds to the input spectral density $g(k)$ (see Fig. 4.2.2b).

4.3 Dynamic Simulations

In the following, we will first present the numerical method and model setup applied in our simulations of the onset of friction. We then provide a theoretical model to describe the simulations and present a comparison between the theoretical predictions with the numerical results.

4.3.1 Numerical Model

We model the physical problem, as described in Sec. 4.2.1, with the Spectral Boundary Integral Method (SBIM) (Geubelle and Rice, 1995; Breitenfeld and Geubelle, 1998). This method solves efficiently and precisely the elasto-dynamic equations of each half space. The spectral formulation applied in SBIM naturally provides periodicity along the interface. The half spaces are perfectly elastic and we apply a shear modulus of $G = 1$ GPa, Poisson's ratio of $\nu = 0.33$ and density $\rho = 1170$ kg/m³, and impose a plane-stress assumption. While we will report our results in adimensional quantities, we note that these parameters correspond to the static properties of glassy polymers, which have been widely used for friction experiments (Svetlizky and Fineberg, 2014; Rubino et al., 2017).

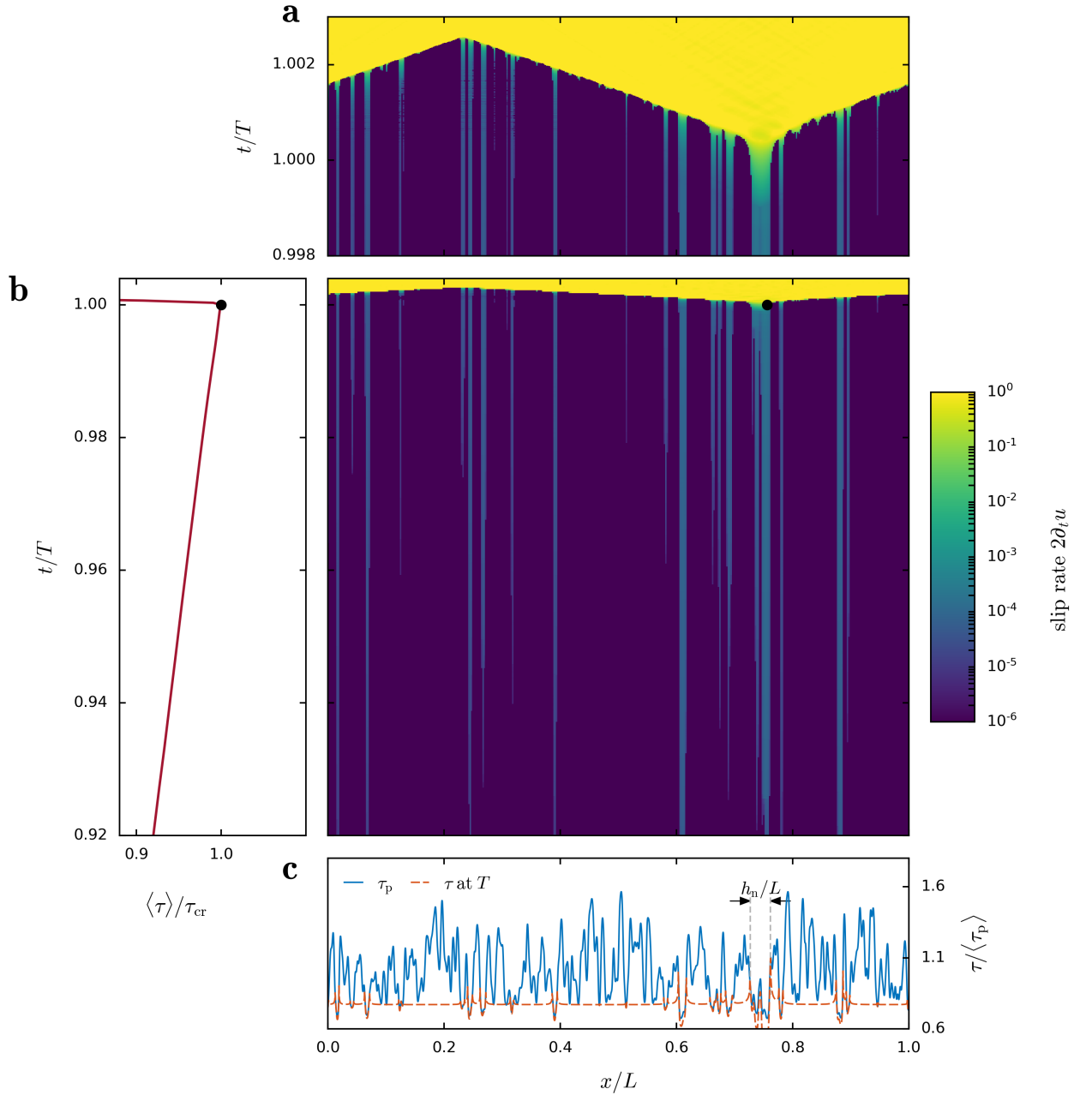


Figure 4.3.1: Representative numerical simulation of the onset of frictional sliding along an interface with random peak strength. (a) Space-time diagram of slip rate along the interface. Time is normalized by the time of friction onset T . Nucleation occurs at $x/L \approx 0.75$. (b-right) Same space-time diagram as in (a) with larger time span. Nucleation is marked by a black dot at $x/L \approx 0.75$ and $t/T = 1$. (b-left) Evolution of average interface stress $\langle \tau \rangle(t)$ normalized by its maximum value τ_{cr} . This corresponds to Fig. 4.2.1b. (c) Stress state $\tau(x)$ at $t/T = 1$ and random profile of peak strength $\tau_p(x)$ for simulation shown in (a-b). The correlation length is $\xi_0/h_n = 0.25$. The size of the critical nucleation patch h_n is marked by black arrows.

The interface between the two half spaces is coupled by a friction law as given by Eq. 4.1. The friction law corresponds essentially to a cohesive law, as known from fracture-mechanics simulations, but applied to the tangential direction. It describes the evolution of local strength as a function of slip. We apply peak strength $\tau_p(x)$ as a random field, following the description provided in Sec. 4.2.2, and constant τ_r . $\tau_p(x)$ follows a Beta distribution with $\alpha = 1.5$ and $\beta = 3$. We impose a maximum value for relative peak strength of $\max(\tau_p(x) - \tau_r) = 1.66$ MPa and minimum value of $\min(\tau_p(x) - \tau_r) = 0.66$ MPa. Therefore, the random field has a mean value of $\langle \tau_p - \tau_r \rangle = 1$ MPa and standard deviation of 0.2 MPa. We further apply a constant slip-weakening rate of $W = 0.5$ TPa/m, which is representative for glassy polymers (Svetlizky et al., 2020). Finally, a slowly increasing uniform shear stress $\tau_0(t)$ and constant uniform normal stress p is applied along the entire interface.

We use a repetition length of $L = 0.1$ m, which is, as we will show, considerably larger than the characteristic nucleation length scale. The interface is discretized by 512 – 1024 nodes. We verified convergence with respect to discretization, loading rate, and time step.

The results of a representative simulation are shown in Fig. 4.3.1. The $\tau_p(x)$ profile has many local minima (see Fig. 4.3.1c). Depending on their value, these minima cause localized slip, as evidenced by bright blue vertical stripes over most of the time period shown in Fig. 4.3.1b-right. These localized slip patches grow slowly with increasing loading, which is difficult to see for most patches in Fig. 4.3.1b-right. Growth is easiest observed for the slip patch at $x/L \approx 0.75$. Incidentally, this patch grows enough to reach

a critical size from which on the patch becomes unstable, marked by a black dot, and starts growing dynamically. This dynamic propagation, see orange-red area in Fig. 4.3.1a enlarged from Fig. 4.3.1b-right, does not stop and, therefore, causes sliding along the entire interface – hence global sliding. The effect on the macroscopic applied force on the mean interfacial shear stress $\langle\tau\rangle(t)$ is shown in Fig. 4.3.1b-left. At the precise moment when the slip patch becomes unstable, marked by a black dot, $\langle\tau\rangle(t)$ starts decreasing rapidly. The maximum value, denoted τ_{cr} , represents the macroscopic strength of the interface.

The simulation shows that macroscopic strength is not reached when the first point along the interface starts sliding but when the most critical slip patch becomes unstable, starts propagating dynamically, and "breaks" the entire interface. Therefore, the criterion determining macroscopic strength is non-local and depends on the stability of local slip patches. In the following section, we will present a theoretical description of this nucleation process and provide a criterion for the limit of macroscopic strength.

4.3.2 Theory for Nucleation of Local Sliding

During the nucleation process, a weak point along the interface starts sliding. Due to local stress transfer, the size of this slipping area grows continuously until it reaches a critical size and unstable interface sliding occurs (Campillo and Ionescu, 1997). This process is equivalent to the instability of a cohesive crack, which can be expressed and solved as an eigenvalue problem (Li and Liang, 1993; Bažant and Li, 1995; Dempsey

et al., 2010). In this section, we will adapt the criterion developed by Uenishi and Rice (2003), which is shortly summarized in 4.A, to describe and predict the limits of stable slip-area growth. Uenishi and Rice (2003) considered a similar system with two main differences to the problem studied here. First, in their case, the interface strength is uniform and the applied load is non-uniform. 4.A shows that both problems result in the same equation for the problem statement and thus lead to the same nucleation criterion. Second, Uenishi and Rice (2003) considered a system with an isolated non-uniformity in the applied load. In other words, the applied stress was mostly uniform but with one well-contained local increase. Therefore, the location of nucleation is known in advanced. In our system, where the non-uniform property is random, the location is unknown. We will address this difference here and discuss it further in Sec. 4.5.

Uenishi and Rice (2003) showed that on interfaces governed by linear slip-weakening friction (Eq. 4.1), there is a unique critical length for stable growth of the slipping area, which can be approximated by

$$h_n \approx 1.158 \frac{G^*}{W}, \quad (4.8)$$

where $G^* = G/(1 - \nu)$ for mode II plane-stress ruptures, assuming the stress within h_n has not attained the residual value τ_r anywhere. Eq. 4.8 shows that h_n depends only on the shear modulus G^* and the slip-weakening rate W . Most importantly, the critical length is independent of the shape of the non-uniformity in the system. Specifically to our case, it does not depend on the functional form of $\tau_p(x)$. Since we have homogeneous elastic solids and a uniform slip-weakening rate W , the critical size h_n is unique and uniform along the entire interface.

The important question for our problem, however, is to determine the level of critical stress that causes a nucleation patch to reach h_n and initiate global sliding. The solution for the stress level leading to nucleation, as derived by [Uenishi and Rice \(2003\)](#), is given by [Eq. 4.21](#), and can be rewritten in terms of $\tau_p(x)$ and h_n as

$$\tau_n(x) \approx 0.751 \int_{-1}^{+1} \tau_p\left(\frac{h_n}{2}s + x\right) v_0(s) ds, \quad (4.9)$$

where x is the center location of the nucleation patch and $v_0(s) \approx (0.925 - 0.308s^2)\sqrt{1 - s^2}$ is the first eigenfunction of the elastic problem. Note that the transformation applied to the argument of $\tau_p(x)$ results in the integral being computed over the critical nucleation patch size h_n . [Eq. 4.9](#) shows that the nucleation stress, which leads to a nucleation patch of size h_n , does clearly depend on the shape of $\tau_p(x)$. [Eq. 4.9](#) assumes that stresses within the nucleation patch have not attained the residual strength yet. Thus, the assumption of small-scale yielding does not hold, and the Griffith criterion for crack propagation does not apply. Note that this approach is based on a continuum description and does not model the failure of individual asperities where locations in between are contact free and hence have zero frictional strength, as studied by [Aghababaei et al. \(2016\)](#) and [Barras et al. \(2019\)](#).

As stated earlier, the nucleation stress $\tau_n(x)$ was derived for a contained non-uniformity, for which we know the location. Therefore, $\tau_n(x)$ corresponds to the critical stress of the system. In our system, however, $\tau_p(x)$ is random and multiple nucleation patches might slowly grow. Determining the critical stress τ_{cr} of the system requires computing the nucleation stress τ_n for each nucleation patch and identifying the critical one. To address this aspect, we follow the approach by [Ampuero et al. \(2006\)](#) and compute

Eq. 4.9 as a weighted moving average over the entire interface, and define the critical stress to be its minimum (see Fig. 4.3.2a). Therefore, we define the critical stress τ_{cr} as

$$\tau_{\text{cr}} = \tau_{\text{n}}(x_{\text{cr}}) \quad \text{such that } \tau_{\text{cr}} < \tau_{\text{n}}(x) \quad \forall x \neq x_{\text{cr}} . \quad (4.10)$$

For simplicity, we refer to this definition also as $\tau_{\text{cr}} = \min(\tau_{\text{n}}(x))$ and $x_{\text{cr}} = \arg \min(\tau_{\text{n}}(x))$. While it is possible, but not very likely, to have multiple minima of τ_{n} with the same amplitude, this does not affect the resulting τ_{cr} . However, multiple x_{cr} could coexist which would result in multiple slip patches becoming unstable simultaneously. By adopting Eq. 4.9 and defining Eq. 4.10, we essentially assume that there is no interaction between nucleation patches. We will verify the validity of this assumption in the following section.

4.3.3 Results

We compare the results from numerical simulations, as described in Sec. 4.3.1, with the theoretical prediction from Sec. 4.3.2 by analyzing simulations with random $\tau_{\text{p}}(x)$ generated using the method described in Sec. 4.2.3. For each of the three different correlation lengths $\xi_0/h_{\text{n}} = 0.25, 0.5,$ and 2.0 we run 20 simulations. The system size is fixed and chosen such that it is considerably larger than the nucleation length, *i.e.*, $h_{\text{n}}/L = 0.034$.

A representative example is shown in Fig. 4.3.1. The size of h_{n}/L is indicated in Fig. 4.3.1c and appears to provide a reasonable prediction for the nucleation patch size as observed in Fig. 4.3.1a. Further comparison is given in Fig. 4.3.2a. First, we illustrate the theoretical prediction. The nucleation stress $\tau_{\text{n}}(x)$ (solid blue line) is computed from

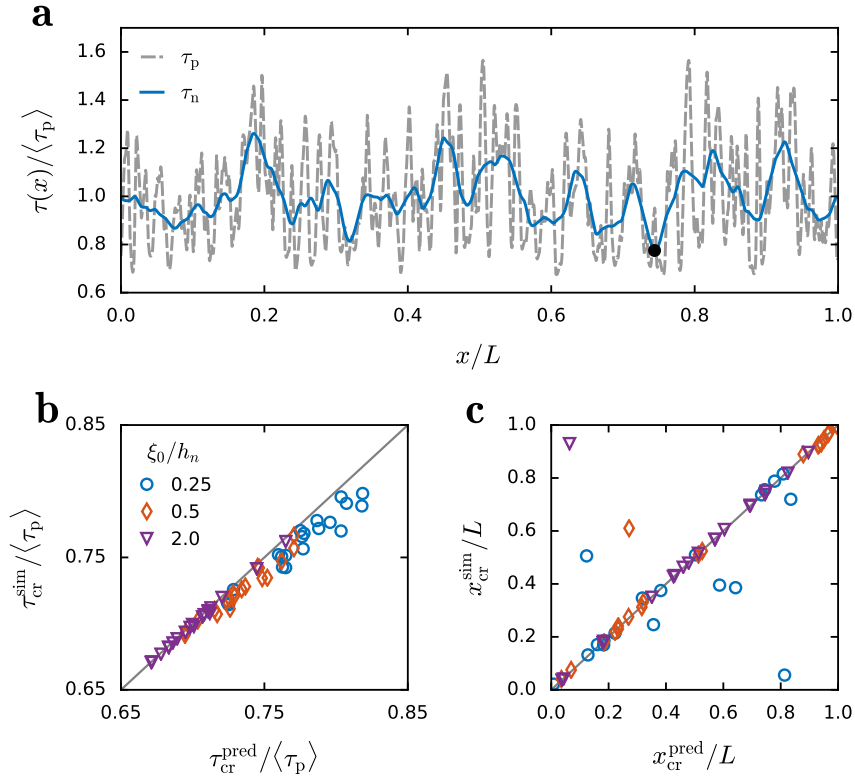


Figure 4.3.2: Verification of nucleation criterion on numerical simulations. (a) The random profile of $\tau_p(x)$ from simulation shown in Fig. 4.3.1 is depicted by dashed gray line. The nucleation stress $\tau_n(x)$ computed from $\tau_p(x)$ by Eq. 4.9 is shown as solid blue line. The point of nucleation given by Eq. 4.10, *i.e.*, (x_{cr}, τ_{cr}) , is marked by a black dot. (b) Comparison of critical length from theoretical prediction by Eq. 4.10 τ_{cr}^{pred} as shown in (a) with values measured from numerical simulations τ_{cr}^{sim} as illustrated in Fig. 4.3.1. 20 simulations are computed for each ξ_0/h_n value. (c) Comparison of nucleation location from theoretical prediction x_{cr}^{pred} with simulation result x_{cr}^{sim} for the same 60 simulations as shown in (b). (b-c) Gray line indicates slope of 1.

$\tau_p(x)$ (gray dashed line) using Eq. 4.9, and τ_{cr} is, according to Eq. 4.10, the minimum of $\tau_n(x)$ (marked by black dot). We find the location of nucleation to be $x_{cr}/L \approx 0.75$, which corresponds to our observation from the numerical simulation, as seen in Fig. 4.3.1.

A more precise and systematic comparison is provided in Fig. 4.3.2b&c. We compare the predicted critical stress τ_{cr}^{pred} with the measured value from dynamic simulations τ_{cr}^{sim} . We compute τ_{cr}^{pred} as described above with Eq. 4.10, and as illustrated in Fig. 4.3.2a. We further find $\tau_{cr}^{sim} = T\partial_t\tau_0$, where $\partial_t\tau_0$ is the applied loading rate and T is the time at which the mean interface stress, $\langle\tau\rangle(t)$, is maximal (see Fig. 4.3.1b-left). Comparison of τ_{cr}^{pred} with τ_{cr}^{sim} is shown in Fig. 4.3.2b for all 60 simulations. The results show that the prediction works generally well. For decreasing ξ_0/h_n the prediction becomes slightly less accurate with a tendency to over-predict the critical value. The results further show that the predicted and measured critical stress τ_{cr} increases with decreasing ξ_0/h_n .

While the location of nucleation is not relevant for the apparent global strength of our system, we compare the predicted and simulated x_{cr} for further evaluation of the developed theory. The comparison shown in Fig. 4.3.2c uses x_{cr}^{pred} , as given by Eq. 4.10 and shown for an example in Fig. 4.3.2a, and x_{cr}^{sim} as found by analyzing the simulation data as illustrated in Fig. 4.3.1a&b-right. The data shows that the prediction works well for most of the simulations. For 8 simulations, 6 of which have $\xi_0/h_n = 0.25$, the prediction does not work. However, as shown in Fig. 4.3.2b, τ_{cr} , which is the quantity of interest here, is correctly predicted for all of these cases. The reason for this discrepancies are likely second-order effects, as we will discuss in Sec. 4.5.

Overall, the results show that τ_{cr} is quantitatively well predicted by the theory presented in Sec. 4.3.2. This allows us to study systematically the effect of randomness in interface properties by applying the theoretical model in analytical Monte Carlo simulations.

4.4 Analytical Monte Carlo Study

In the following section, we introduce Monte Carlo simulations, which are based on the theoretical framework for nucleation of frictional ruptures in a random field of frictional strength $\tau_{\text{p}}(x)$, as derived in Sec. 4.3.2. The effect of correlation length ξ_0 on the effective frictional strength τ_{cr} (Eq. 4.10), and its probability distribution $f(\tau_{\text{cr}})$, is studied, while keeping all other properties constant. A Monte Carlo study based on the full dynamic problem (Sec. 4.3.1) would be computationally daunting. However, the theoretical framework allows us to evaluate τ_{cr} very efficiently and has been validated by 20 full dynamic simulations for each considered ξ_0 (see Fig. 4.3.2).

4.4.1 Monte Carlo Methodology

The effective frictional strength $\tau_{\text{cr}} = \min(\tau_{\text{n}}(x))$ requires the computation of the nucleation strength $\tau_{\text{n}}(x)$, which involves a convolution of the local peak strength $\tau_{\text{p}}(x)$ with the eigenfunction v_0 , given in Eq. 4.9. Considerable computation time can be saved by

using a spectral representation of the random field $\tau_p(x)$:

$$\tilde{\tau}_p(x) = \sum_{j=0}^J \hat{\tau}_p(k_j) e^{-ik_j x}, \quad (4.11)$$

where $\tilde{\tau}_p(x)$ signifies that $\tilde{\tau}_p(x)$ is an approximation of $\tau_p(x)$ and the number of frequencies J is chosen such that the approximation error $|\tilde{\tau}_p - \tau_p|$ is negligible. $\hat{\tau}_p(k_j)$ is the discrete Fourier transform of $\tau_p(x)$

$$\hat{\tau}_p(k_j) = \int_0^L \tau_p(x) e^{-ik_j x} dx, \quad (4.12)$$

where $\tau_p(x)$ is generated using the procedure described in Sec. 4.2.3. By substituting Eq. 4.11 into Eq. 4.9 the nucleation strength convolution becomes a dot product:

$$\begin{aligned} \tilde{\tau}_n(x) &\approx 0.751 \int_{-1}^{+1} \sum_{j=0}^J \hat{\tau}_p(k_j) e^{-ik_j(s - h_n/2 + x)} v_0(s) ds \\ &\approx 0.751 \sum_{j=0}^J \hat{\tau}_p(k_j) g_j(x) \end{aligned} \quad (4.13)$$

where $g_j(x) = \int_{-1}^{+1} e^{-ik_j(\frac{h_n}{2}s + x)} v_0(s) ds$ is the modal convolution term, which, being independent of the sample specific functional form of $\tau_p(x)$, can be pre-computed. This formulation allows for efficient and precise evaluation of the effective frictional strength $\tau_{cr} = \min \tau_n(x)$ for a large number of samples $N = 10,000$, such that the probability distribution $f(\tau_{cr})$ and its evolution as function of the correlation length ξ_0 can be accurately studied.

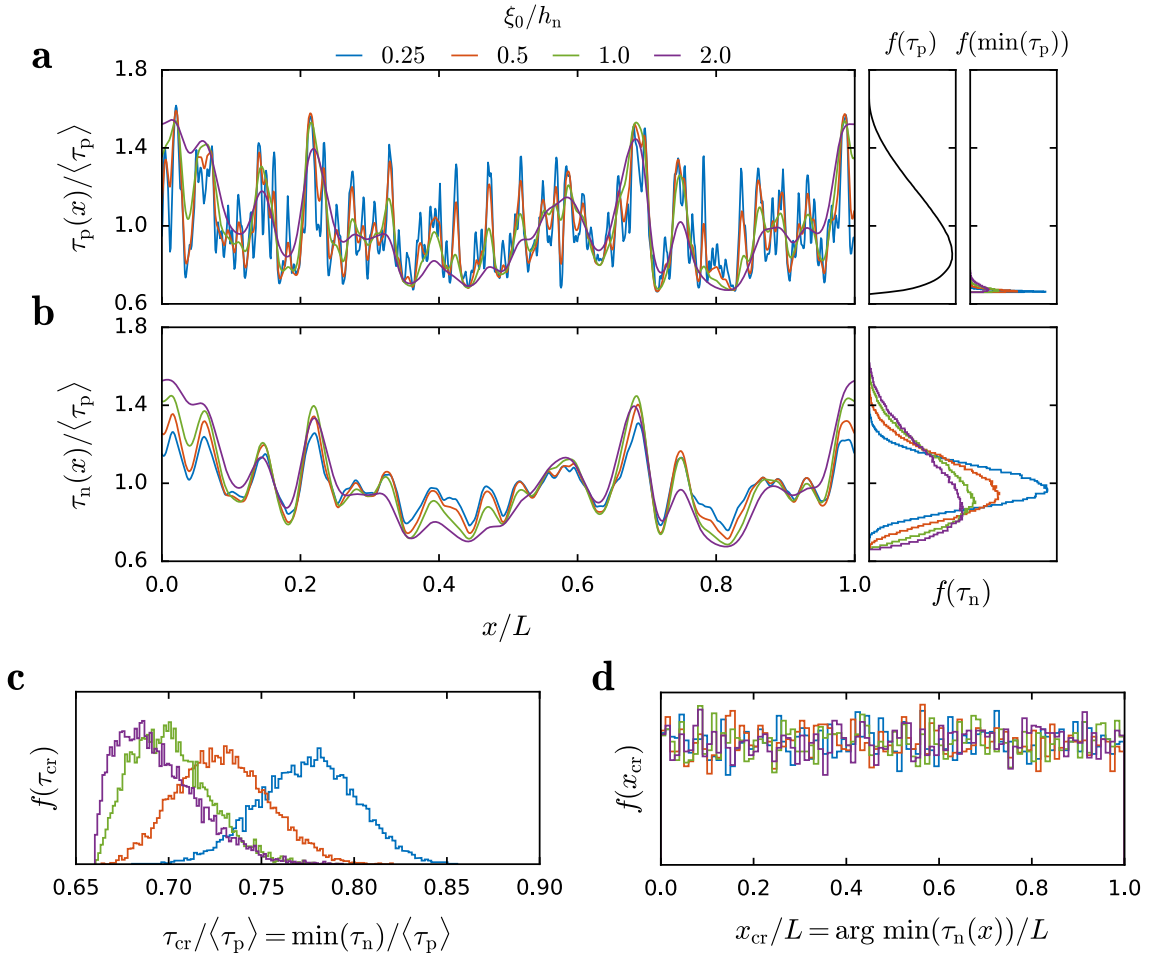


Figure 4.4.1: Analytical Monte Carlo study. (a) The random local friction strength $\tau_p(x)$ is generated with different correlation lengths ξ_0 . For visual purposes, the same random seed is used for the 4 cases shown. (b) The corresponding local nucleation strength $\tau_n(x)$ is computed using (Eq. 4.9). The probability densities f of the random fields τ_n , $\min(\tau_n)$ and τ_p are reported on the right of (a) and (b), respectively and computed using $N = 10,000$ samples. $f(\min(\tau_p))$ and $f(\tau_n)$ depend on ξ_0 . (c) Probability density of the global friction strength τ_{cr} . (d) Probability density of the position of the critical nucleation patch x_{cr} . Note that the seed is not fixed anymore for the samples used in (c) and (d).

4.4.2 Monte Carlo Results

Prior to presenting the numerical results we provide some intuition of the effect of correlation length on the nucleation strength τ_n based on probabilistic arguments. By exploiting the stationarity of τ_p and τ_n it is possible to derive an analytical expression of the expectation of the nucleation strength $E[\tau_n]$ and its variance $\text{Var}[\tau_n]$ as function of the corresponding statistical properties of local strength, $E[\tau_p]$, $\text{Var}[\tau_p]$ and ξ_0/h_n (see 4.B).

One interesting finding is that the expectation is not affected by ξ_0/h_n : $E[\tau_n] = E[\tau_p]$ (see derivation in Eq. 4.23). The expression for $\text{Var}[\tau_n]$, however, involves a double integral of the product of the correlation function $C(\cdot)$ and the eigenfunction $v_0(\cdot)$, which can be evaluated numerically (see derivation in Eq. 4.24).

For perfect correlation, *i.e.*, $\xi_0/h_n = \infty$, $C(\cdot)$ becomes a constant, thus $\text{Var}[\tau_n] = \text{Var}[\tau_p]$. Additionally, in the limit of $\xi_0 \ll h_n$, the double integral in Eq. 4.24 scales with ξ_0/h_n , thus $\text{Var}[\tau_n] \propto \text{Var}[\tau_p]\xi_0/h_n$ (see derivation in Eq. 4.26).

We consider a range of correlation lengths $\xi_0/h_n = \{0.25, 0.5, 1.0, 2.0\}$, while all other properties remain constant. Fig. 4.4.1a-left shows one sample of $\tau_p(x)$ for each considered ξ_0 . For clarity of visualization, in Fig. 4.4.1a we use the same seed when generating the random fields. Hence, the fields have the same modal random amplitudes A_j and B_j , see Eq. 4.5, but have different modal spectral densities σ_j^2 , corresponding to the different ξ_0 . For this reason, all shown samples have a similar spatial distribution and the effect of varying ξ_0 can be clearly observed. By definition, all $\tau_p(x)$ samples are drawn from the same probability distribution $f(\tau_p)$ (see Fig. 4.4.1a-center). Decreasing ξ_0 , moves the

probability density of its minimum $f(\min(\tau_p))$ towards the lower bound $\tau_p^{\min} = 0.66\langle\tau_p\rangle$ (see Fig. 4.4.1a-right), because with lower correlation lengths it is more likely to visit a broad range of τ_p values.

Fig. 4.4.1b-left shows the corresponding nucleation strength $\tau_n(x)$ for each of the local frictional strength fields $\tau_p(x)$ presented in Fig. 4.4.1a, computed using Eq. 4.13. As mentioned before, τ_n is essentially a weighted moving average of τ_p with window size h_n (see Eq. 4.9). Thus, most of the high frequency content of τ_p disappears and the effect of ξ_0 on τ_n is more subtle. One interesting feature is in the minima and maxima of τ_n : increasing ξ_0 causes lower minima and higher maxima, because the moving average is effectively computed over an approximately constant field $\tau_n \approx \tau_p$. Inversely, decreasing ξ_0 causes the opposite effect and $\tau_n \approx \langle\tau_p\rangle$.

This effect is more clearly visible by considering the distribution $f(\tau_n)$ shown in Fig. 4.4.1b-right. Increasing ξ_0 effectively puts more weight onto the tails of $f(\tau_n)$ (see $\xi_0/h_n = 2.0$ in Fig. 4.4.1b-right), and in the limiting case of $\xi_0/h_n \rightarrow \infty$ the distribution of τ_n will be the same as the one of τ_p (analogous to Eq. 4.25). On the other hand, decreasing ξ_0 puts weight on its mean $\langle\tau_p\rangle$, making $f(\tau_n)$ similar to a Gaussian (see $\xi_0/h_n = 0.25$ in Fig. 4.4.1b-right) with variance proportional to ξ_0 (see Eq. 4.26). In the limit $\xi_0/h_n \rightarrow 0$ the distribution of τ_n becomes a Dirac- δ centered at $\langle\tau_p\rangle$. The described dependence of $f(\tau_n)$ on ξ_0 confirms the previously stated statistical arguments (see 4.B for derivation).

Because $f(\tau_p)$ is skewed towards the lower bound of τ_p so is $f(\tau_n)$; the larger ξ_0 the larger the skewness. For τ_{cr} this effect is amplified by the fact that $\tau_{cr} = \min(\tau_n(x))$

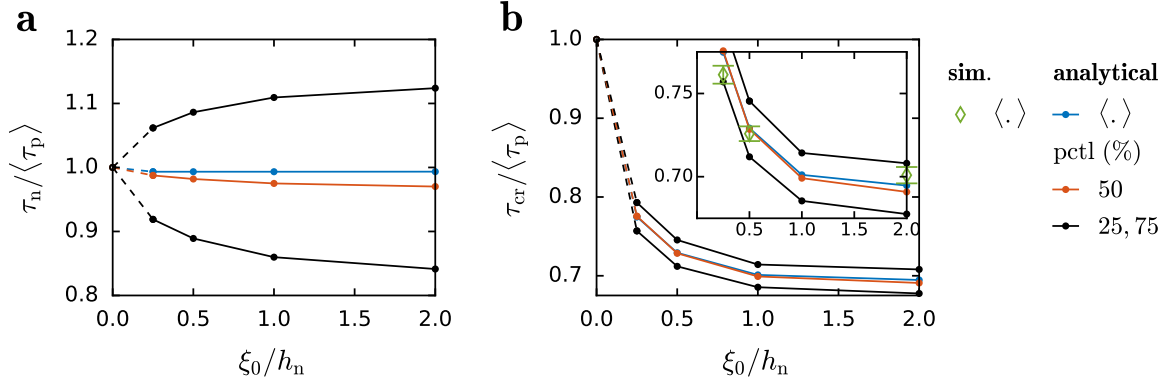


Figure 4.4.2: Variation of nucleation strength τ_n (a) and effective friction strength τ_{cr} (b) as function of correlation length ξ_0 . Solid lines are the results from the analytical Monte Carlo study with $N = 10,000$ (same data as Fig. 4.4.1). Data-points for $\xi_0/h_n \rightarrow 0$ are based on analytical considerations and connected to the analytical Monte Carlo results by dashed lines. Diamonds are results from 60 dynamic simulations (same data as Fig. 4.3.2).

as depicted in Fig. 4.4.1c, causing $\langle \tau_{cr} \rangle$ to decrease with increasing ξ_0 . As noted in Sec. 4.3.3, the location where the critical instability occurs x_{cr} is uniformly distributed over the entire domain as shown in Fig. 4.4.1d and is independent on ξ_0 .

We further analyze the effect of ξ_0 on the probability distribution of τ_n and τ_{cr} by reporting the mean, median and 25% percentile of the probability density function (see Fig. 4.4.2). We observe that the nucleation strength tends towards the mean peak strength for vanishing correlation length, $\lim_{\xi_0/h_n \rightarrow 0} \tau_n(x) = \langle \tau_p \rangle$, because the moving average in computing $\tau_n(x)$ is evaluated over a window h_n that appears infinite compared to ξ_0 (see Fig. 4.4.2a). Consequently, the effective strength also tends towards the mean of the local strength: $\lim_{\xi_0/h_n \rightarrow 0} \tau_{cr} = \langle \tau_p \rangle$ (see Fig. 4.4.2b). Conversely, if $\xi_0 \gg h_n$, the moving average is computed over a window h_n which vanishes, and thus (4.9) becomes the

identity: $\lim_{\xi_0/h_n \rightarrow \infty} \tau_n(x) = \tau_p(x)$. In this case, the effective strength will be more likely to be close to the actual lower bound of the distribution $\lim_{\xi_0/h_n \rightarrow \infty} \tau_{cr} = \min(\tau_p)$ (see Fig. 4.4.2b). The transition between these two limiting cases is described by the results of the analytical Monte Carlo study, which are validated by 20 dynamic simulations for each ξ_0/h_n by reporting the mean effective friction strength (see inset in Fig. 4.4.2b). For $\xi_0/h_n \geq 0.5$ simulations and theory coincide. However, for $\xi_0/h_n = 0.25$ the theoretical model slightly overestimates the effective friction strength. In Sec. 4.5, we will discuss the origin of the observed lower effective friction at small ξ_0/h_n .

4.5 Discussion

4.5.1 Implications of the Physical Problem

The analyzed physical problem is simplistic and contains only the absolute minimum of a realistic system with a frictional interface – while still maintaining a rigorous representation of the constitutive relation of the bulk and the interface. The objective is to provide a fundamental understanding of the macroscopic effects on static friction caused by randomness in the local frictional properties. While many options exist to complexify the proposed system, we leave them for future work and focus here on the basics. Nevertheless, in this section, we will discuss some of these simplifications as well as their implications.

Randomness along the interface may have various origins including heterogeneity in bulk material properties and local environmental conditions (*e.g.*, humidity and impurities). Prominent causes for randomness are geometric imperfections, which include non-flat interfaces and surface roughness. The real contact area, which is an ensemble of discrete micro-contacts (Bowden and Tabor, 1950; Dieterich and Kilgore, 1994; Li and Kim, 2008; Sahli et al., 2018) and is much smaller than the apparent contact area, introduces naturally randomness to the interface. Surface roughness is often modeled as self-affine fractals (Pei et al., 2005), which directly affects the size distribution of micro-contacts and local contact pressure. The resulting frictional properties are expected to vary similarly. This would typically lead to small areas of the interface with high frictional strength and most areas with no resistance against sliding, *i.e.*, $\tau_p = 0$, since only the micro-contacts may transmit stresses across the interface. Therefore, at this length scale, one would expect the random strength field to be bound by zero at most locations, similar to the approach taken by Barras et al. (2019). However, in many engineering systems, the nucleation length is orders of magnitude larger than the characteristic length scales of the micro-contacts: nucleation lengths of $\sim 10 - 100$ mm (Ben-David and Fineberg, 2011; Latour et al., 2013) and surface roughness lengths of ~ 1 μm (Svetlizky and Fineberg, 2014). For this reason, we consider a continuum description with a somewhat larger length scale. In our approach, the frictional strength profile is continuous and varies due to randomness in the micro-contacts population without considering individual contact points.

Surface roughness and other local properties directly affect how frictional strength changes depending on slip δ , slip rate $\partial_t \delta$, and state (Rabinowicz, 1995; Pilvelait et al.,

2020). This is often modeled in phenomenological rate-and-state friction models (Dieterich, 1979; Ruina, 1983; Rice and Ruina, 1983). As discussed by Garagash and Germanovich (2012) and demonstrated by Rubin and Ampuero (2005) and Ampuero and Rubin (2008), the nucleation length scale of rate-and-state friction models approaches asymptotically the critical length h_n used in this work and given by Eq. 4.8 if the rate-and-state friction parameters are favoring strong weakening with slip rate, *i.e.*, $a/b \rightarrow 0$, and the slipping region is prevented to expand laterally. However, if rate-weakening becomes negligible, the nucleation criterion tends towards the Griffith’s length (Andrews, 1976), which applies to ruptures with small-scale yielding. In this case, the frictional weakening process is contained in a small zone at the rupture tip and most of the rupture surface is at the residual stress level, which is different to the nucleation patches by Uenishi and Rice (2003), where the entire rupture surface is still weakening when the critical length is reached.

While on geological faults rate-neutral or even strengthening friction is common (Marone, 1998), engineering materials such as polymer glasses (Baumberger and Caroli, 2006; Bar-Sinai et al., 2014; Rubino et al., 2017), metals (Rabinowicz, 1995; Armstrong-Hélouvry et al., 1994), and paper (Baumberger and Caroli, 2006) have strong rate-weakening friction, which results in large scale yielding during nucleation. For this reason, we assume a slip weakening friction with strong slip-weakening.

Since many engineering materials present relatively important slip-rate weakening friction, *e.g.*, dynamic weakening of ~ 1 MPa for glassy polymers at normal pressure of ~ 5 MPa (Svetlizky et al., 2020) and, similarly, ~ 1 MPa weakening for granite

at normal pressure of ~ 6 MPa (Kammer and McLaskey, 2019), we considered a model system with strong frictional weakening. However, we neglect the complexity of rate-and-state friction, as extensively demonstrated by Ray and Viesca (2017, 2019), and apply a linear slip-weakening friction law at the interface because it has the most important features of friction, *i.e.*, a weakening mechanism, while being simple and well-understood. The advantage is that the weakening-rate W is predefined. It further has a well-defined *fracture* energy Γ , which is the energy dissipated by the weakening process, *i.e.*, the triangular area $(\tau_p - \tau_r)d_c/2$ in Fig. 4.2.1c:

$$\Gamma(x) = \frac{(\tau_p(x) - \tau_r)^2}{2W}. \quad (4.14)$$

Since W is constant in our system Γ varies with $(\tau_p(x) - \tau_r)^2$. Assuming that variations in Γ and τ_p are predominately caused by surface roughness and, hence, random contact pressure $p(x)$, a correlation between $\Gamma(x)$ and $\tau_p(x)$ can be expected (at least in some range of p) because $\Gamma \propto p$ (Bayart et al., 2016) and $\tau_p \propto p$ as assumed in most friction constitutive laws. Nevertheless, the exact relation applied here is a first-order approximation.

Further, the linear slip-weakening law is contact-pressure independent, which may appear counter-intuitive based on Coulomb's well-known friction laws (Amontons, 1699; Coulomb, 1785). However, the contact pressure is, due to symmetry in similar-material interfaces, constant over time and, therefore, any possible pressure dependence becomes irrelevant for the nucleation process itself. Nevertheless, local friction properties are expected to change for systems with different normal pressure. This effect has not been

analyzed here since we did not vary the contact pressure, but could be taken into account by changing the values of τ_p , τ_r and d_c .

Finally, we note that by assuming a periodic system, we neglect possible boundary effects. We expect that the boundary would locally reduce τ_{cr} compared to the prediction based on Eq. 4.10, which assumes an infinite domain, because the free boundary would locally restrict stress redistribution and thus increase the stress at the edge of the nucleation patch. Therefore, the probability density of global frictional strength τ_{cr} for a periodic system, as shown in Fig. 4.4.1c, has likely a slight tendency towards higher values compared to a finite system. However, we expect the spatial range of the boundary effect to scale with h_n and, therefore, $f(\tau_{cr})$ will tend towards the periodic solution for $h_n/L \rightarrow 0$. Verification would require a large number of numerical simulations, which is beyond the scope of this work.

4.5.2 Interpretation of Numerical Simulations

The simulations have shown that uniform τ_0 and random $\tau_p(x)$ cause multiple nucleation patches to develop simultaneously. We can see in Fig. 4.3.1b-right that 20-30 patches (bright blue stripes) coexist by the time global strength is reached, *i.e.*, $t/T = 1$. Most of these nucleation patches grow very slowly and their number increases with increasing $\tau_0(t)$. Nucleation patches can also merge, which is what happens in this simulation to the critical patch. Furthermore, the simulation shows that unstable growth and thus global failure is not necessarily caused by the first nucleation patch to appear. For instance,

the $\tau_p(x)$ profile shown in Fig. 4.3.1c presents three local minima with approximately the same value, *i.e.*, at $x/L \approx 0.4, 0.6$ and 0.75 . Therefore, the first three nucleation patches appear quasi-simultaneously. Whether one of these patches or another one appearing later is the one becoming unstable first does only depend indirectly on the minimum value of $\tau_p(x)$. More important is whether $\tau_p(x)$ remains low in the near region of the local minimum. The nucleation patch at $x/L \approx 0.75$ is in an area of relatively low $\tau_p(x)$, compared to the other early nucleation patches, which is why it develops faster to the critical size and causes unstable propagation.

This non-local character of the nucleation patches becomes obvious when considering the integral form of Eq. 4.9 that corresponds to a weighted moving average of $\tau_p(x)$. In Fig. 4.3.2a, we can see that τ_n at $x/L \approx 0.75$ is considerably lower than at the location of the other early nucleation patches $x/L \approx 0.4$ and 0.6 . This is why $x/L \approx 0.75$ gets critical first and causes unstable slip area growth. Interestingly, $x/L \approx 0.3$ is the second most critical point even though the local minimum in τ_p is higher than many others in this system. However, $\tau_p(x)$ remains rather low over an area that approaches h_n , and therefore τ_n is also low.

In Fig. 4.3.2, we compared the prediction of τ_{cr} with measurements from simulations and showed that the prediction works generally well. However, we noticed that for decreasing ξ_0/h_n the discrepancies increase. The theory generally predicts higher τ_{cr} than observed in simulations. Schär et al. (2020) showed that the coalescence of subcritical nucleation patches is the cause for these discrepancies. In this process, two nucleation patches, which individually would require substantial additional load to reach h_n , coa-

lesce and, hence, result in a nucleation patch that exceeds h_n already at $\tau_{cr}^{sim} < \tau_{cr}^{pred}$. Interestingly, a similar phenomenon has recently been observed in simulations of compressive failure governed by a mesoscopic Mohr-Coulomb criterion, where local damage clusters interact and eventually coalesce to macroscopic failure (Dansereau et al., 2019). However, Schär et al. (2020) also showed that critical coalescence, which causes these discrepancies, occurs predominantly for an intermediate range of ξ_0/h_n and becomes less likely for small ξ_0/h_n .

The nucleation patch coalescence is likely also the cause for discrepancies observed in the prediction of the nucleation location x_{cr} , as shown in Fig. 4.3.2c. While most cases are very well predicted, some simulations present unstable growth that starts from a different location. In these cases, two nucleation patches have very similar critical stress level. However, the (slightly) less critical patch coalesces with a neighboring smaller patch and thus becomes unstable at a lower stress level than theoretically expected. This is more likely to occur for systems with low ξ_0/h_n since this increases the likelihood of another local minimum being located close to active nucleation patches. Nevertheless, the critical stress level τ_{cr} remains quantitatively well predicted, as shown Fig. 4.3.2b and discussed above, because these secondary effects are minor.

The representative simulation illustrated in Fig. 4.3.1 shows that the frictional rupture front, after becoming unstable, does not arrest until it propagated across the entire interface leading to global sliding. This is a general feature of our problem and all our simulations present the same behavior. What is the reason for this run-away propagation? Right after nucleation, the slipping area continues to weaken along its entire length,

i.e., $\delta < d_c$ everywhere. However, after some more growth, it transforms slowly into a frictional rupture front, which is essentially a Griffith's shear crack with a cohesive zone and constant residual strength (Svetlizky and Fineberg, 2014; Svetlizky et al., 2020; Garagash and Germanovich, 2012). The arrest of frictional rupture fronts are governed by an energy-rate balance (Kammer et al., 2015), which states that a rupture continues to propagate as long as the (mode II) static energy release rate G_{II} is larger than the fracture energy, *i.e.*, $G_{\text{II}} > \Gamma$. In our system, the stress drop $\Delta\tau = \tau_0 - \tau_r$ is uniform since τ_0 and τ_r are uniform. Thus, the static energy release rate grows linearly with rupture length $G_{\text{II}} \propto h$, and it becomes increasingly difficult to arrest a rupture as it continues to grow. Specifically for our case, we find that $G_{\text{II}} > \Gamma_{\text{max}}$ for $h/h_n \gtrsim 3$, where Γ_{max} is Γ from Eq. 4.14 for τ_p^{max} . Hence, once the slipping area reached a size of $h/h_n \gtrsim 3$, nothing can stop it anymore – not even τ_p^{max} . For $h/h_n \lesssim 3$, it is theoretically possible for the slipping area to arrest after some unstable propagation. However, a large increase in $\tau_p(x)$ would need to occur simultaneously on both side, which is very unlikely, in particular for $\xi_0/h_n > 1$. Therefore, our assumptions of constant stress drop $\Delta\tau$ and limited variation of local frictional strength causes arrested rupture fronts to be extremely rare. Nevertheless, since Γ_{max} depends on the probability distribution function $f(\tau_p)$, a larger variance, and thus a larger τ_p^{max} , would make crack arrest (slightly) more likely.

It is interesting to note, however, that arrest of dynamically propagating slipping areas may occur in other systems. Amon et al. (2017), for instance, showed in their simulations that multiple smaller events nucleate and arrest in order to prepare the interface for a global event. In their system, the initial position along the interface is random as well as the friction properties. Therefore, the available elastic energy, which is the driving force, is

random and may fluctuate enough to cause arrest. For the same reason, [Geus et al. \(2019\)](#) observed arrested events of various sizes in simulations with random potential energy along the interface. On the contrary, our system, as outlined above, is characterized by steadily increasing available energy and, thus, behaves differently.

Experimental evidence for arrest of frictional rupture fronts is rather limited. The arrest of confined events observed by [Rubinstein et al. \(2007\)](#) on glassy polymers and by [Ke et al. \(2018\)](#) on granite, is caused by non-uniform loading due to the experimental configuration as demonstrated by [Kammer et al. \(2015\)](#) and [Ke et al. \(2018, 2020\)](#). While small scale randomness in the applied shear stress may occur, it does not cause arrest – at best, it may slightly delay or expedite it. Therefore, these experimental observations do not support the presence of any important randomness in the applied shear load; at least at these scales. In much larger systems, such as tectonic plates, randomness in the background stress is likely very important, as discussed in [Sec. 4.5.4](#).

4.5.3 Interpretation of Monte Carlo Study

In an engineering context, it is usually not enough to know the mean value of a macroscopic property, *e.g.*, the static friction strength, since design criteria are determined based on probability of failure; and risk assessments require failure probability analysis. If the stochastic properties of local interfacial strength $\tau_p(x)$ are known, the developed theoretical framework in [Sec. 4.4](#) provides a tool to evaluate the global strength distribution and, hence, the failure probability. However, $\tau_p(x)$ is not directly observable in

experiments (at least so far). In the absence of experimental evidence, the stochastic properties of $\tau_p(x)$ have been chosen based on physical considerations but our specific parameter choice is arbitrary. This approach is a first approximation that enables us to develop an efficient Monte Carlo method to study the effects of such variations on macroscopic properties. This method may be adapted to more realistic random friction profiles. In the following section we will discuss the choice of each stochastic property of $\tau_p(x)$ and its effect on the variability of global strength, τ_{cr} .

We assumed that $\tau_p(x)$ is a random variable following a Beta distribution because it provides simultaneously a non-Gaussian property and well-defined boundaries for minimum and maximum strength, which is physically consistent since mechanical properties are bounded. The parameters of the Beta distribution are chosen such that it is skewed towards the lower bound of τ_p . Physically this means that the local interface strength is mostly weak with few strong regions. Under this assumption we observed that the global interface strength τ_{cr} is close the lower bound of τ_p and that decreasing correlation length ξ_0 leads to higher τ_{cr} with smaller variation (see Fig. 4.4.2). Nucleation is governed by the strength of the weakest region which size equals or exceeds the nucleation length. Hence, if the skewness would be toward high values of τ_p – this would corresponds to a mostly strong interface with few weak regions – the variation of τ_{cr} would be larger because of the longer tail at the lower bound. However, the effect of correlation length would remain unchanged: lower ξ_0 would cause higher τ_{cr} with smaller variation.

Further, we assumed that τ_p has a power spectral density specified in Eq. 4.4 with a specific exponent, which affects the memory of the random field. A smaller exponent

would result in a flatter decay above the cutoff frequency, and thus generate a field with more high-frequency content. However, when considering equivalent correlation lengths³, effects of different assumptions regarding the functional form of the power spectral density are expected to be minor in the probability density of τ_{cr} .

It is noteworthy that there are three relevant length scales: L , h_{n} and ξ_0 . Here, we have not considered the effects of changes in L so far. Based on our theoretical model, we expect that a larger L would result in smaller variance of τ_{cr} . One approach to explore this effect, while avoiding to change the size of the experimental system, could be to modify the normal load, which would affect τ_{p} and τ_{r} , and hence the critical nucleation size $h_{\text{n}} \propto (\tau_{\text{p}} - \tau_{\text{r}})^{-1}$, as shown experimentally by [Latour et al. \(2013\)](#).

4.5.4 Implications for Earthquake Nucleation

In the current study, we are interested in estimating the probability distribution of the macroscopic strength of a frictional interface of given size L . Similar systems but with a focus on other aspects have been studied in order to gain a better understanding of earthquake nucleation. The challenges in studying earthquake nucleation are associated with the size of the system (hundreds of kilometers) and the limited physical access to measure important properties, such as stress state and frictional properties. However, when and how an earthquake nucleates affects directly the average stress drop level $\langle \Delta\tau \rangle \equiv \tau_{\text{cr}} - \tau_{\text{kin}}$, and the earthquake magnitude, which is more easily determined.

³ $C(\xi_0) = e^{-1}$

Hence, there is a need to infer from earthquake magnitude observation back on the fault properties and their variability, to learn about the risk of potential future earthquakes. This is a similar inverse problem as described above.

Previous studies have shown that randomness in simplified models present earthquake magnitudes that follow a power-law distribution (Carlson and Langer, 1989; Ampuero et al., 2006). The simulations presented a large range of magnitudes because the slipping areas arrested, which is the result of randomness in the local stress drop, as discussed in Sec. 4.5.2. Interestingly, small events were shown to smoothen the stress profile, which reduces the randomness, thus prepared the interface for larger events, as also observed experimentally (Ke et al., 2018). This would suggest that nucleation of larger events tend to be caused by randomness in fault properties rather than (background) stress level, since the stress is getting smoothed. Therefore, our model provides a simple but reasonable tool to study nucleation of medium to large earthquakes.

Our results show that smaller correlation length lead to higher overall strength and more variation. In the context of earthquakes, this would suggest that smaller ξ_0/h_n support larger earthquake magnitudes since nucleation at a higher stress level translates into larger average stress drops, which provides more available energy to release and, thus, makes arrest more difficult. This is complementary to observations by Ampuero et al. (2006) that showed a trend to higher earthquake magnitudes for decreasing standard deviation of the random stress drop field $\Delta\tau(x)$ while keeping ξ_0/h_n constant.

In addition to the important question on critical stress level for earthquake nucleation, it also remains unclear how the nucleation process takes place. Two possible models

([Beroza and Ellsworth, 1996](#); [Noda et al., 2013](#); [McLaskey, 2019](#)) are discussed. The "Cascade" model, where foreshocks trigger each other with increasing size and finally lead to the main earthquake; and the "Pre-Slip" model, which assumes that nucleation is the result of aseismic slow-slip. In our simplistic model, nucleation occurs in a "Pre-Slip" type process, with a long phase of slow slip and an abrupt acceleration after the nucleation patch reached its critical size (see [Fig. 4.3.1b-right](#)). However, if the amplitude range of our random $\tau_p(x)$ field was much larger, the likelihood of arrest would increase and, thus, interaction between arrested small events could emerge. This would lead to a nucleation process that resembles more the "Cascade" model. We, therefore, conclude that the type of nucleation process that may occur at a given fault depends on extent of randomness in the local stress and property fields.

4.6 Conclusion

We studied the stochastic properties of frictional interfaces considering the nucleation of unstable slip patches. We considered a uniform loading condition and studied the effect of random interface strength, characterized by its probability density and correlation function. Using numerical simulations solving the elastodynamic equations, we demonstrated that macroscopic sliding does not necessarily occur when the weakest point along the interface starts sliding, but when one of possible many slowly slipping nucleation patches reaches a critical length and becomes unstable. We verified that the nucleation criterion originally developed by [Uenishi and Rice \(2003\)](#) predicts well the critical stress leading to

global sliding if the criterion is formulated as a minimum of the local strength convolved with the first eigenfunction of the elastic problem. The simulations further showed that increasing correlation lengths of the random interface strength lead to reduced macroscopic static friction. Using the theoretical nucleation criterion, we perform a Monte Carlo study that provided an accurate description of the underlying probability density functions for these observed variations in macroscopic friction. We showed that the probability density function of the global critical strength approaches the probability density of the minimum in the random local strength when the correlation length is much larger than the critical nucleation length. Conversely, a vanishingly small correlation length results in generally higher macroscopic strength with smaller variation. We showed that the presence of precursory dynamic slip events, as in more complex models, is extremely unlikely under the assumption of uniform stress drop. Finally, we discussed discrepancies between the theoretical model and simulations, which suggest that for small correlation lengths the theoretical prediction overestimates the frictional strength, possibly because it neglects coalescence of neighboring nucleation patches.

APPENDIX

4.A Nucleation Criterion

The nucleation criterion used in this work is based on the theory developed by [Uenishi and Rice \(2003\)](#). It is not our intention of re-deriving the theoretical framework. Nevertheless, in this section, we provide a clear problem statement such that our work can easily be related to the work by [Uenishi and Rice \(2003\)](#). The peak strength along the interface is given by

$$\tau_p(x) = \tau_p^{\min} + q(x) , \quad (4.15)$$

where τ_p^{\min} is the minimum value of $\tau_p(x)$. The functional form $q(x)$ satisfies $q(x_m) = 0$ and $q(x) > 0$ for $x \neq x_m$. If local slip occurs at any point along the interface, the local strength decreases because of the slip-weakening friction law, as defined by Eq. 4.1. Therefore, any point that is in the weakening process, *i.e.*, $d_c > \delta(x, t) > 0$, presents a local shear stress that is given by

$$\tau(x) = \tau_p(x) - W\delta(x, t) = \tau_p^{\min} + q(x) - W\delta(x, t) , \quad (4.16)$$

where Eq. 4.15 was used and the weakening rate satisfies $W > 0$.

The applied shear stress, which starts at the level of the minimum strength, is defined by

$$\tau_0(t) = \tau_p^{\min} + Rt , \quad (4.17)$$

where $R > 0$ is the shear-stress loading rate.

Following [Uenishi and Rice \(2003\)](#), we can consider the quasi-static elastic equilibrium ([Bilby and Eshelby, 1968](#)) that relates the stress change along the interface with the local slip through

$$\tau(x, t) = \tau_0(x, t) - \frac{G^*}{2\pi} \int_{a_-(t)}^{a_+(t)} \frac{\partial \delta(\xi, t) / \partial \xi}{x - \xi} d\xi, \quad (4.18)$$

where $G^* = G/(1 - \nu)$ and $a_-(t) < x < a_+(t)$ are the boundaries of the slowly expanding slipping area. By substituting Eq. 4.16 and Eq. 4.17 into Eq. 4.18, we find

$$-W\delta(x, t) = Rt - q(x) - \frac{G^*}{2\pi} \int_{a_-(t)}^{a_+(t)} \frac{\partial \delta(\xi, t) / \partial \xi}{x - \xi} d\xi, \quad (4.19)$$

for $\delta(x, t) > 0$ and $a_-(t) < x < a_+(t)$. This corresponds exactly to ([Uenishi and Rice, 2003](#), Eq.4).

Starting from this equation, [Uenishi and Rice \(2003\)](#) show that quasi-static solutions cease to exist for slipping areas larger than a critical length h_n , which is given by

$$h_n \approx 1.158 \frac{G^*}{W}. \quad (4.20)$$

Interestingly, the critical length only depends on the shear modulus G^* and the slip-weakening rate W , and is independent of the loading rate R and the shape of the peak strength $q(x)$.

[Uenishi and Rice \(2003\)](#) further show that a slipping area exceeding h_n is reached at time t_c when the critical stress level is given by ([Uenishi and Rice, 2003](#), Eq.14)

$$Rt_c \approx 0.751 \int_{-1}^{+1} q[a(t_c)s + b(t_c)]v_0(s)ds, \quad (4.21)$$

where $a(t) = [a_+(t) - a_-(t)]/2$ and $b(t) = [a_+(t) + a_-(t)]/2$ are the half-length and center location of the slipping area, respectively, and $s = [x - b(t)]/a(t)$ and $v_0(s) \approx$

$(0.925 - 0.308s^2)\sqrt{1 - s^2}$. It becomes obvious that the stress level at which the slipping area reaches the critical length depends on the shape of $q(x)$.

4.B Simplified Statistical Analysis of the Nucleation Strength

In order to give some intuition of the effects of correlation length ξ_0 on the nucleation strength τ_n (Eq. 4.9), we provide a statistical argument, which is based on the property of stationarity of τ_p . Note that $v_0(\cdot)$ has the following property

$$0.751 \int_{-1}^{+1} v_0(s) ds = 1 \quad (4.22)$$

We aim to evaluate the expectation and variance of τ_n as function of ξ_0 . The expectation is an integral with respect to a probability measure rather than a Lebesgue measure. Since τ_p and τ_n are stationary, we can apply the Fubini's theorem, which states that the order of integration can be changed, and express the expectation $E[\tau_n]$ as function of the expectation of the local strength $E[\tau_p]$.

$$\begin{aligned} E[\tau_n] &= E \left[0.751 \int_{-1}^{+1} \tau_p(s h_n/2 + x) v_0(s) ds \right] = 0.751 \int_{-1}^{+1} E[\tau_p(s h_n/2 + x)] v_0(s) ds \\ &= E[\tau_p] 0.751 \int_{-1}^{+1} v_0(s) ds = E[\tau_p] \end{aligned} \quad (4.23)$$

Similarly, we can express its variance $\text{Var}[\tau_n]$ as function of the variance of the local strength $\text{Var}[\tau_p]$ by applying Fubini's Theorem and the definition of the correlation func-

tion $C(\xi) = E[(\tau_p(x) - E[\tau_p])(\tau_p(x + \xi) - E[\tau_p])]/\text{Var}[\tau_p]$

$$\begin{aligned}
\text{Var}[\tau_n] &= E[(\tau_n(x) - E[\tau_n])^2] = E \left[\left(0.751 \int_{-1}^{+1} \tau_p(s h_n/2 + x) v_0(s) ds - E[\tau_p] \right)^2 \right] \\
&= E \left[\left(0.751 \int_{-1}^{+1} (\tau_p(s h_n/2 + x) - E[\tau_p]) v_0(s) ds \right)^2 \right] \\
&= 0.751^2 \iint_{[-1,1]^2} E [(\tau_p(s h_n/2 + x) - E[\tau_p]) (\tau_p(t h_n/2 + x) - E[\tau_p])] v_0(s) v_0(t) ds dt \\
&= \text{Var}[\tau_p] 0.751^2 \iint_{[-1,1]^2} C((s - t)h_n/2) v_0(s) v_0(t) ds dt
\end{aligned} \tag{4.24}$$

For the limiting cases the expression for the variance can be expressed analytically. For perfectly correlated τ_p , $\xi_0 = \infty$, $C(\cdot) = 1$

$$\lim_{\xi_0/h_n \rightarrow \infty} \text{Var}[\tau_n] = \text{Var}[\tau_p] \tag{4.25}$$

Both $C(\cdot)$ and $v_0(\cdot)$ are known. Therefore, the integral of Eq. 4.24 can be solved numerically (see Fig.4.B.1). For $\xi_0 \ll h_n$ the correlation function $C(\cdot) \approx \text{Dirac-}\delta$ and the double integral collapses to a single integral.

$$\xi_0 \ll h_n \Rightarrow \text{Var}[\tau_n] \propto \text{Var}[\tau_p] \int_{-1}^{+1} \frac{\xi_0}{h_n} v_0^2(s) ds \propto \text{Var}[\tau_p] \frac{\xi_0}{h_n} \tag{4.26}$$

Note the linear scaling for $\xi_0 \ll h_n$ in Fig. 4.B.1d.

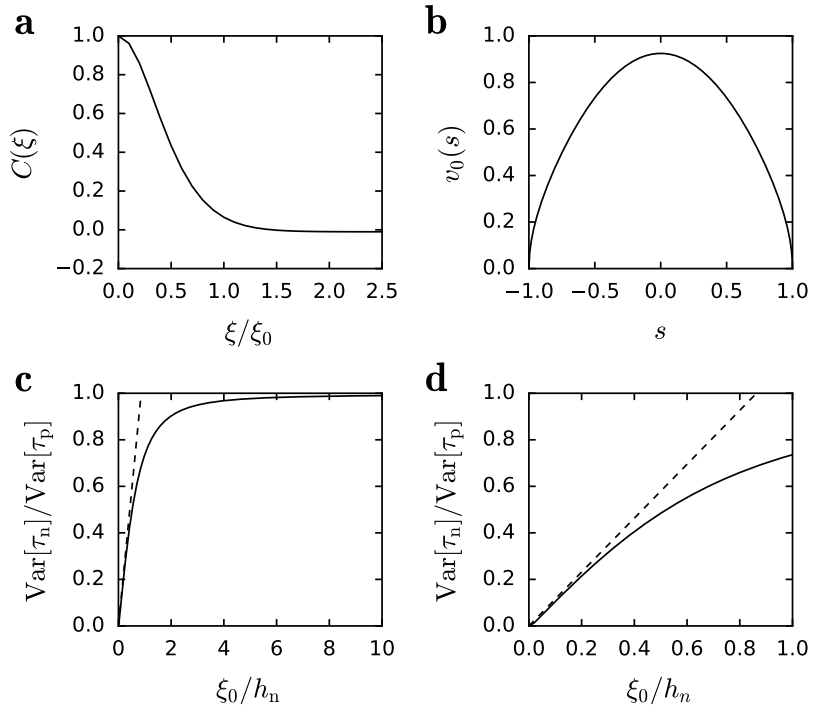


Figure 4.B.1: Numerical evaluation of Eq. 4.24. (a) Correlation function. (b) First eigenfunction of the elastic problem. (c) Normalized variance of the nucleation strength τ_n . (d) Zoom over $\xi_0 < h_n$. Dashed line in (c,d) represents approximation Eq. 4.26 for $\xi_0 \ll h_n$.

CHAPTER 5

EFFECTIVE TOUGHNESS OF HETEROGENEOUS MATERIALS WITH RATE-DEPENDENT FRACTURE ENERGY

This chapter is drawn from the following article, currently under review:

Albertini, G., Lebihain, M., Hild, F. Ponson, L. and Kammer, D.S. (2021), ‘Effective toughness of periodic heterogeneous materials: the role of rate-dependent fracture energy’, [arXiv:2003.13805](https://arxiv.org/abs/2003.13805) [[cond-mat.soft](https://arxiv.org/abs/2003.13805)].

We investigate dynamic fracture of heterogeneous materials by measuring displacement fields as a rupture propagates through a periodic array of obstacles of controlled toughness. We provide direct evidence of crack speed jumps at the boundary of obstacles. Our experiments reveal that such a discontinuous dynamics emerges from rate-dependent fracture energy, which combined with inertia, allows the crack to cross a fracture energy discontinuity at constant energy release rate. The rate-dependency is a direct consequence of the out-of-equilibrium nature of the fracture phenomenon and is often neglected. However, it plays a central role in setting up homogenized toughness, leading ultimately to increased resistance to failure.

5.1 Introduction

Many biological materials, such as bone, nacre and tooth, have intricate microstructures which are responsible for remarkable macroscopic mechanical properties (Ritchie, 2011; Jackson A. P. et al., 1988). Carefully designed microstructures combined with advances in micro-fabrication techniques allow for the development of new materials with unprecedented properties (Florijn et al., 2014; Bles et al., 2015; Bertoldi et al., 2010; Silverberg et al., 2014; Siéfert et al., 2019; Yin et al., 2019). Understanding how to harness small-scale heterogeneities is, however, necessary to achieve the desired macroscopic properties. For fracture properties, recent research focused either on disordered microstructures, where randomly located obstacles distort the crack front and cause toughening by collective pinning (Gao and Rice, 1989; Roux et al., 2003; Ponson and Pindra, 2017; Lebihain et al., 2020), or on elastic heterogeneities, where compliant inclusions provide toughening by effectively reducing the energy flow into the crack tip (Hossain et al., 2014; Wang and Xia, 2017). However, a complete and fundamental theory for effective material resistance against fracture remains missing, and experimental observations, which are key for establishing such theoretical knowledge, are scarce.

To address fracture problems theoretically, one can use the well-established framework of fracture mechanics that builds from the seminal work of Griffith (Griffith and Taylor, 1921; Rice, 1978): a crack will propagate as soon as the released elastic energy per unit increment of crack length $G^S = -\partial_l \Omega$, where Ω is the elastic energy in the medium and l the crack length, balances the local fracture energy Γ (*i.e.*, the energy necessary for creating two unit surfaces). Γ is generally assumed to be a material constant.

However, in heterogeneous media, this approach lets several questions unanswered. As G^S is a continuous function of crack length l , when the crack faces a sudden drop in fracture energy there is an excess elastic energy release rate $G^S > \Gamma$. How is this excess energy dissipated? As our experimental observation will show, body inertia is not the only mechanism that can balance the excess energy release (Freund, 1990; Sharon and Fineberg, 1999), and there exists a quasi-static mechanism that allows the crack to leave tough obstacles without having to reach speeds $v = \dot{l}$ close to the Rayleigh wave speed c_R – the theoretical limit speed for a crack (Freund, 1990). The second issue relates to the problem of a crack entering a region of larger fracture energy. Only *dynamic* fracture mechanics would predict that the crack crosses the interface into the (marginally) tougher obstacle. However, as our experiments will show, cracks may not stop at the interface, if the incident speed is larger than some critical speed. And here also, inertia is not required as a quasi-static approach assuming $v \ll c_R$ suffices to capture this phenomenon. To the best of our knowledge, neither of these mechanisms have been experimentally observed and quantified in a well-controlled setting.

In this Letter, we analyze these issues in depth through the experimental investigation of crack propagation in heterogeneous media with fracture energy discontinuities. Usually, fracture mechanics experiments are based on global measurements, thus, only capture averaged quantities. In contrast, our experimental setup and simplified 2D geometry with periodic heterogeneities allows local measurements of the near-crack-tip fields, which support the uncovering of fundamental mechanisms. While the elastic energy release rate is constant as the crack faces a fracture energy discontinuity, the speed at which the crack propagates is observed to vary discontinuously. We study the amplitude of the

speed jumps as the crack crosses the interface between regions of different fracture energy and show that it stems from rate-dependency of fracture energy in addition to inertia of the medium. Rate-dependent effects result from the non-equilibrium nature of fracture problems and are prevailing in materials. Thus, rate-dependent fracture energy applies to a wide range of materials and has been observed, for instance, on rock (Ponson, 2009; Atkinson, 1984), glassy polymers (Sharon and Fineberg, 1999; Scheibert et al., 2010; Vasudevan et al., 2021) and metals (Rosakis and Zehnder, 1985). Surprisingly, rate-dependent effects are generally neglected. However, they significantly affect the effective toughness of heterogeneous materials, as we will show with our experimental observations.

5.2 Method

Our experimental setup (see FIG. 5.2.1a) consists of a tapered double cantilever beam, made of multi-material 3D-printed polymers (Stratasys Objet260 Connex3), a high-speed camera (Phantom v2511) and an electromechanical testing machine (Shimadzu AG-X Plus). The matrix material is VeroClear with static fracture energy $\Gamma_0^M \approx 80 \text{ J/m}^2$ and Young's modulus $E^M \approx 2.8 \pm 0.2 \text{ GPa}$. The obstacle material is VeroWhite-DurusWhite ($\Gamma_0^O \approx 106 \text{ J/m}^2$, $E^O \approx 1.9 \pm 0.2 \text{ GPa}$), which is tougher and more compliant. We prescribe a constant crack mouth displacement rate $\dot{\delta} \approx 25 \text{ mm/s}$. Hence, the elastic energy in the system is gradually increased, until a planar crack initiates from a pre-existing notch. The elastic energy release rate at initiation is proportional to the bluntness of the notch, which we can tune to explore a range of initial crack speeds from moderate

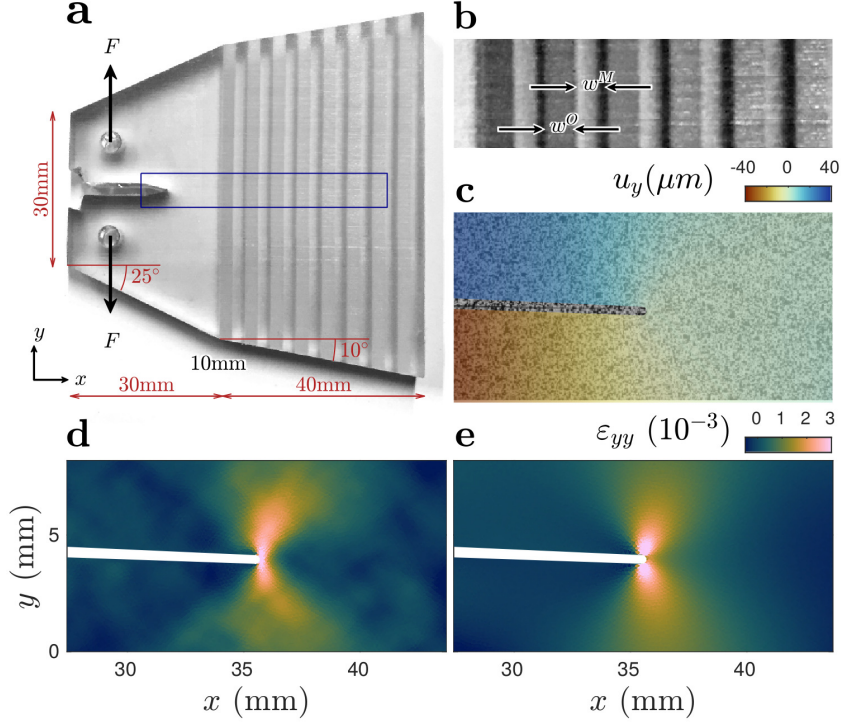


Figure 5.2.1: (a) Model heterogeneous material made of multi-material 3D-printed polymers in a tapered double cantilever beam geometry with applied forces F . The displacement field $\mathbf{u} = (u_x, u_y)$ is measured in the area within the blue box by digital image correlation. (b) Closeup view shows two different materials in a periodic stripe geometry. The transparent material constitutes the matrix with width w^M and the opaque (darker) areas are obstacles of higher fracture energy $\Gamma^O/\Gamma^M \approx 1.3$ with width w^O . (c) Closeup of crack tip at $l \approx 35\text{mm}$ and $v \approx 50\text{m/s}$. The crack interface is slightly visible running from left to center. A random speckle pattern is applied onto the surface, which is compared to its reference pre-cracked configuration to find \mathbf{u} . (d) Infinitesimal strain $\epsilon_{yy} = \partial_y u_y$ found by differentiating \mathbf{u} . Approaching the crack tip, ϵ_{yy} diverges. (e) ϵ_{yy} assuming the Williams eigenfunctions as basis for \mathbf{u} .

up to $350 \text{ m/s} \approx 0.4c_R$, where $c_R \approx 800 \text{ m/s}$. The crack propagates then dynamically through a series of periodic obstacles (see FIG. 5.2.1b). During crack propagation no additional energy is added to the system (δ is constant) and the tapered geometry causes exponentially decaying released elastic energy $G^S \sim \delta^2 e^{-l/l_{\text{sys}}}$, where $l_{\text{sys}} \approx 17.5 \text{ mm}$ is a structural length scale directly related to the sample size (Grabois et al., 2018). Thus, the crack speed gradually decreases on average. All properties are constant through the sample thickness and the overall behavior is quasi-2D. We analyze the crack dynamics by measuring the near-tip displacement field \mathbf{u} using Digital Image Correlation. We apply a random speckle pattern (see FIG. 5.2.1c) onto the surface of the specimen using aerosol paint. The temporal evolution of the speckle is tracked using high speed photography at 250,000 fps. The auto-correlation length of the pattern corresponds to 4-6 pixels, where the pixel size is $\approx 45 \mu\text{m}$. \mathbf{u} (see color in FIG. 5.2.1c) is found by minimizing the difference between the pattern at a given time t mapped back to its pre-crack configuration (see Supplemental Material in Appendix 5.A). The resulting infinitesimal strain field ε_{yy} is depicted in FIG. 5.2.1d. An alternative approach (see FIG. 5.2.1e) is the Integrated Digital Image Correlation (IDIC) (Roux and Hild, 2006; Grabois et al., 2018), which assumes the analytical solution for a singular crack in an infinite elastic medium – the Williams eigenfunctions expansion (Williams, 1956) – as basis for \mathbf{u} (see Supplemental Material in Appendix 5.A). The first term of the series has singular strains at the crack tip $\varepsilon_{ij} \sim 1/\sqrt{r}$, where r is the distance from the tip and its amplitude is related to the stress intensity factor K . Note that for both methods the amplitude of ε is similar. IDIC has the advantages of precisely determining the crack tip position l and directly computing K , from which, one can find the dynamic energy release rate $G = \frac{K^2}{E} A(v)$ that provides a

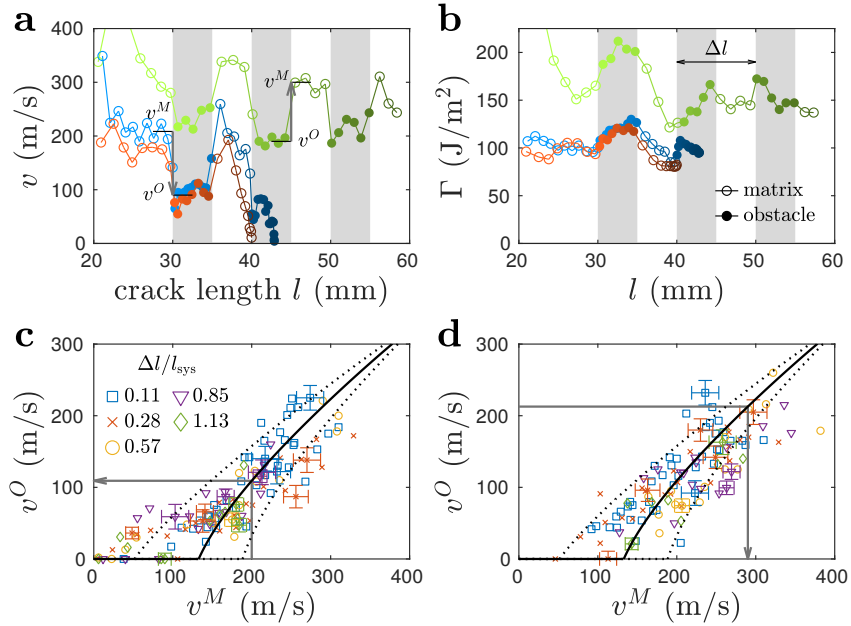


Figure 5.3.1: (a,b) Experimental results for three specimens with $\Delta l/l_{\text{sys}} = 0.57$. (a) v undergoes abrupt deceleration ($l = \{30, 40, 50\}$ mm) and acceleration ($l = \{35, 45, 55\}$ mm) when the crack front is trapped and untrapped, respectively, at the interface. (b) Discontinuities in Γ occur at trapping and untrapping with higher values within the obstacle. (c) Trapping: speed prior to entering the obstacle v^M is plotted vs. speed immediately after v^O . When the approaching velocity $v^M < v_c \approx 130$ m/s the front arrests. (d) Untrapping: speed after exiting the obstacle v^M is plotted vs. speed immediately before exiting v^O . (c,d) Solid black line is the theoretical model (5.2) with $\pm 10\%$ variation in Γ (dotted lines).

measure of the fracture energy Γ at the crack tip (Freund, 1990; Svetlizky and Fineberg, 2014) (see Supplemental Material in Appendix 5.A). The effects of elastic heterogeneity are minor and discussed in (see Supplemental Material in Appendix 5.A).

5.3 Results

Typical experiments are illustrated in FIG. 5.3.1a&b. The crack first propagates through the matrix material with propagation speed v being maximum immediately after initiation, then v gradually decreases as crack length increases. v undergoes abrupt deceleration (acceleration) as the front enters (leaves) an obstacle. Simultaneously, Γ also abruptly increases (decreases). However, the relative jumps of the dissipation rate are significantly smaller than the ones observed on crack speed. We calculate the speed in the obstacle v^O and matrix v^M by selecting the mean speed over $12\mu\text{s}$ before and after the obstacle boundaries. All speed jumps at material discontinuities were studied for a collection of 30 experiments with different period length $\Delta l = w^O + w^M$ and constant obstacle density $\beta = \frac{w^O}{w^O + w^M} = 1/2$. Jumps as the crack enters (trapping) and leaves (untrapping) an obstacle are shown in FIG. 5.3.1c&d, respectively. Results show that the crack dynamics at the matrix/obstacle interface is independent of obstacle width and is symmetric with respect to the direction of propagation, *i.e.*, the jumps are the same for trapping and untrapping. This implies that the crack dynamics only depends on local fracture properties.

In order to understand the jumps and their effect on effective material properties, we analyze the fracture propagation with a crack-tip energy balance. In our experiments, failure mechanisms occur at time scales 4 orders of magnitude smaller than the viscous relaxation time typical of the polymers used in this study (see Supplemental Material in Appendix 5.A) so that an elastic response of the sample can be safely assumed. Moreover, the failure mechanisms are too fast for a craze to develop (Ravi-Chandar and Balzano,

1988), making the fracture process essentially brittle. Thus, we develop a theoretical model based on Linear Elastic Fracture Mechanics (LEFM) to interpret the experimental observations.

As the crack advances, elastic energy G^S is released from the specimen and is in part dissipated as fracture energy Γ to create new surfaces and in part radiated away as elastic waves. Analyzing the near-tip fields of a steady-state dynamic crack, Freund (1990) showed that the energy release rate of a dynamic crack $G(l, v)$ is related to the energy release rate for a corresponding static crack $G^S(l)$ by $g(v)$, a universal function of v . The crack-tip energy balance provides the equation of motion for a crack (see Supplemental Material in Appendix 5.A)

$$\Gamma(v) = G^S(l)g(v) \approx G^S(l)(1 - v/c_R), \quad (5.1)$$

which implies that within the framework of LEFM, a sub-Rayleigh crack in an infinite medium has no inertia and v adjusts instantaneously to fluctuations in Γ or G^S (see Supplemental Material in Appendix 5.A). We note that for rate-dependent materials, the fracture energy $\Gamma(v)$ is not a constant as commonly assumed.

We analyze the rate-dependence of the matrix and obstacle material by independently plotting Γ vs. v (see averaged data as dashed line in FIG. 5.3.2 or full data in FIG. S3 of (see Supplemental Material in Appendix 5.A)). We observe that our measurements are in good agreement with a model by (Scheibert et al., 2010) (solid line in FIG. 5.3.2) that considers the actual dissipative mechanism taking place within the process zone. Within the matrix or obstacle material, the fracture energy follows this kinetic law. At the material boundaries, however, the rupture needs to jump from one kinetic law to the

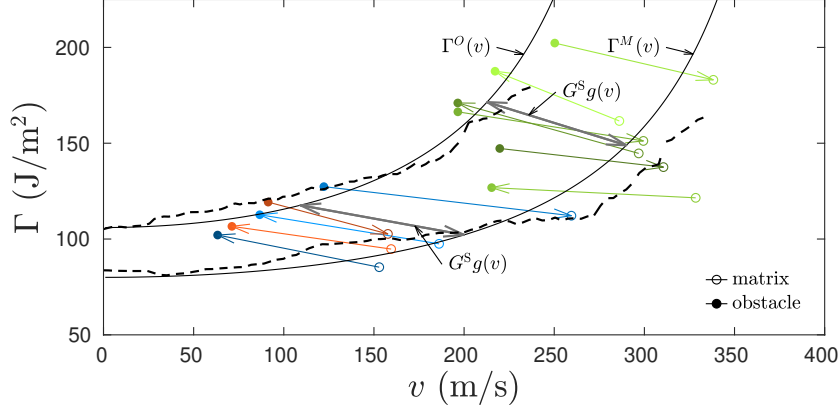


Figure 5.3.2: Experimental results for the same specimens shown in FIG. 5.3.1a&b – with same color-code. Data points represent crack speed and fracture energy at the moment of transition of material property. $\Gamma(v)$ is separated in two distinct clusters corresponding to the matrix and obstacle material. Black dashed lines are the average fracture energy measurements based on 30 heterogeneous and 10 homogeneous samples (see Supplemental Material in Appendix 5.A). Solid black lines are the rate-dependent fracture energy law (Scheibert et al., 2010) for the obstacle $\Gamma^O(v)$ and matrix $\Gamma^M(v)$ materials. The transition from one branch to the other is described by $G^S(l)g(v)$ – the equation of the gray arrows (5.1).

other. The jump amplitude is governed by the energy balance (5.1). The jump trajectory in the Γ - v space corresponds to the right-hand side of (5.1), which, since $G^S(l)$ is constant across the boundary, corresponds to a diagonal line $G^S g(v)$ (arrows in FIG. 5.3.2).

Thus, at a discontinuity in material property the equation of motion of a crack becomes

$$G^S = \Gamma^M(v^M)/g(v^M) = \Gamma^O(v^O)/g(v^O) , \quad (5.2)$$

which captures the experimentally observed velocity discontinuity at trapping and untrapping with no fitting parameter (see FIG. 5.3.1c&d). Eq. (5.2) cannot be solved explicitly. However, assuming a *linear* rate-dependent fracture energy $\Gamma(v) \approx \Gamma_0 + \gamma v$,

for the purpose of discussion, the velocity jump becomes

$$v^M - v^O \approx \Delta\Gamma_0 \frac{1 - v^M/c_R}{\gamma + \Gamma_0^M/c_R}, \quad (5.3)$$

where $\Delta\Gamma_0 = \Gamma_0^O - \Gamma_0^M$ is the jump in fracture energy. This simple result highlights that (i) the jump amplitude is the same for trapping and untrapping (FIG. 5.3.1c&d) and (ii) during trapping the velocity right after the interface is zero if v^M is smaller than a critical incident velocity v_c below which the obstacle causes crack arrest

$$v_c \approx \Delta\Gamma_0 / (\gamma + \Gamma_0^O/c_R). \quad (5.4)$$

All these features are discernible from our experimental data and are captured fairly well by the model. Eq. (5.3) as well as a parameter study of (5.2) (see FIG. S3 in (see Supplemental Material in Appendix 5.A)) reveal that the speed jump and v_c are proportional to the toughness discontinuity $\Delta\Gamma_0$. The latter is particularly noisy because of variations of fracture properties of both matrix and obstacle material, *i.e.*, $\text{Var}[\Delta\Gamma_0] = \text{Var}[\Gamma_0^M] + \text{Var}[\Gamma_0^O]$, assuming Γ_0^O and Γ_0^M are uncorrelated. In the limit of small rate dependency $\gamma \ll \Gamma_0/c_R$, inertia starts to control the speed jumps, that are then given by $v^M - v^O \approx (\Delta\Gamma_0/\Gamma_0^M)(c_R - v^M)$ and the corresponding condition for crack arrest becomes $v < v_c \approx (\Delta\Gamma_0/\Gamma_0^O)c_R$. Conversely, in the limit of large rate dependency $\gamma \gg \Gamma_0/c_R$ and quasi-static propagation $v \ll c_R$, inertia can be neglected and the speed jumps become constant $v^M - v^O \approx \Delta\Gamma_0/\gamma \equiv v_c$.

How does such a trapping/untrapping dynamics impact the effective fracture properties $\bar{\Gamma}$ of periodic heterogeneous materials? We compute the homogenized fracture energy $\bar{\Gamma}$ by integrating over an interval Δl of uninterrupted crack propagation starting at l_i ,

the beginning of each matrix/obstacle period,

$$\bar{\Gamma}(\bar{v}) = \frac{1}{\Delta l} \int_{l_i}^{l_i+\Delta l} \Gamma(v(\tilde{l})) d\tilde{l}. \quad (5.5)$$

As the fracture energy in each phase depends on crack speed, the homogenized fracture energy depends on it too. Thus, we report $\bar{\Gamma}$ as a function of the apparent crack velocity $\bar{v} = \Delta l / \int_{l_i}^{l_i+\Delta l} v^{-1} dl$.

Let us first assume $\Delta l \ll l_{\text{sys}}$, *i.e.*, a clear separation between the micro-structural scale and the specimen scale. In this simple case, it is possible to define *intrinsic* homogenized fracture properties, decoupled from the specimen size and the details of applied boundary conditions. Under this assumption, G^S remains constant during the entire crack propagation. Thus, the local crack velocity and fracture energy are constant within each material phase (insets in FIG. 5.3.3a), which allows us to calculate the dissipation rate from (5.5)

$$\lim_{\Delta l/l_{\text{sys}} \rightarrow 0} \bar{\Gamma} = \beta \Gamma^O(v^O) + (1 - \beta) \Gamma^M(v^M) \quad (5.6)$$

and the apparent crack speed

$$\lim_{\Delta l/l_{\text{sys}} \rightarrow 0} \bar{v} = (\beta/v^O + (1 - \beta)/v^M)^{-1}, \quad (5.7)$$

where $\beta = 1/2$ is the obstacle density. Note that (5.7) is a weighted harmonic mean, which is dominated by its lower argument, v^O , so \bar{v} is effectively lower than the arithmetic mean ($\langle v \rangle = \beta v^O + (1 - \beta) v^M$). As a result, the apparent kinetic law $\bar{\Gamma}(\bar{v})$ is shifted towards lower speeds in comparison to the kinetic law $\bar{\Gamma}(\langle v \rangle)$. This leads, in practice, to a resistance to failure $\bar{\Gamma}$ *larger* than the toughness spatial average $\langle \Gamma \rangle = \beta \Gamma^O(\bar{v}) + (1 - \beta) \Gamma^M(\bar{v})$, but lower than the obstacle toughness Γ^O predicted by rate-independent theory (see FIG. 5.3.3).

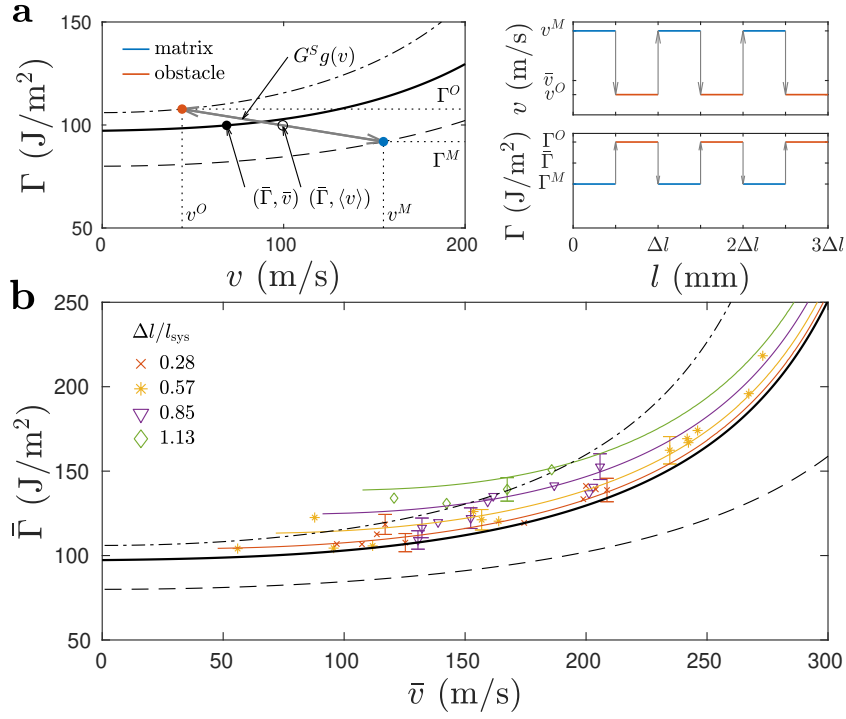


Figure 5.3.3: Homogenization of fracture energy $\bar{\Gamma}$ vs. average velocity, \bar{v} . (a) $\bar{\Gamma}$ assuming the scale separation condition $\Delta l \ll l_{\text{sys}}$. Blue and red dots represent the state of the crack within the two materials, which are related by (5.2) depicted as a gray arrow. The black dot is the corresponding homogenized state $(\bar{\Gamma}, \bar{v})$ computed using (5.6) and (5.7). By varying G^S one can derive the entire homogenized fracture energy law $\bar{\Gamma}(\bar{v})$ (black solid line in a&b). (b) $\bar{\Gamma}(\bar{v})$, measured experimentally using (5.5), is depicted as colored circles for a range of $\Delta l \approx l_{\text{sys}}$. Colored solid lines are the theoretical solution for $\Delta l \approx l_{\text{sys}}$ derived using (5.5), (5.1) (see Supplemental Material in Appendix 5.A) (theory and experiment colors correspond). (a,b) Dash-dotted line and dashed line are $\Gamma^O(v)$ and $\Gamma^M(v)$ from FIG 5.3.2.

However, when comparing the infinite system size prediction (5.6) and (5.7) to our experimental measurements we observe higher effective toughness (see FIG. 5.3.3b). The interplay between the size of the heterogeneity Δl and the structural length scale l_{sys} makes homogenization of fracture properties particularly challenging. The emerging effective toughness depends on the ratio $\Delta l/l_{\text{sys}}$, and (5.6) and (5.7) only represent a lower bound of $\bar{\Gamma}(\bar{v})$. The larger $\Delta l/l_{\text{sys}}$, the higher the homogenized fracture energy $\bar{\Gamma}(\bar{v})$, which can even exceed the toughness $\Gamma^O(\bar{v})$ of the obstacle material. This additional toughening, related to the structural problem with $\Delta l \approx l_{\text{sys}}$, is quantitatively captured by the theoretical solutions for $\bar{\Gamma}(\bar{v})$, which we derive from (5.5) and (5.1), assuming $G^S \sim e^{-l/l_{\text{sys}}}$. Note that as we approach $\Delta l \ll l_{\text{sys}}$, the experimental toughness converges towards the theoretical one; and for $\Delta l \gg l_{\text{sys}}$ the rupture arrests before reaching Δl required for homogenization of fracture properties.

5.4 Discussion and Conclusion

To conclude, our study shows that when a dynamic crack reaches a toughness discontinuity, it will arrest if it was slower than a threshold speed that is primarily dependent on the toughness contrast and independent of the characteristic size of the microstructure (*i.e.*, obstacle thickness). If the crack penetrates the obstacle, it reacts by instantaneously adapting its speed, which is mediated by the rate-dependent fracture energy combined with inertia. Finally, the heterogeneous material presents an increased effective (homogenized) toughness because of high fluctuations in crack speed between obstacles and

matrix, and the rate-dependent nature of the fracture energy. Overall, our findings suggest that the rate-dependency of fracture energy cannot be neglected when considering failure in heterogeneous materials.

What are the practical implications of our findings for material design? The crack arrest criterion in periodic heterogeneous materials is derived in terms of a critical incident speed $v_c \approx \Delta\Gamma_0/(\gamma + \Gamma_0^O/c_R)$ below which an obstacle is capable of stopping a crack. It is worth noting that this is a local mechanism, so even a very thin obstacle can cause the crack to arrest. Thus, the rate-dependent factor γ and the obstacle toughness Γ_0^O can be selected for designing flaw insensitive materials, whose resistance to crack propagation – or ability to prevent a crack to grow indefinitely – is directly proportional to the obstacle toughness but independent of its size.

Finally, we would like to discuss some open questions raised by our findings. Our study highlighted the central role played by rate-dependent fracture energy on the toughness of heterogeneous materials with periodic microstructures. How would rate-dependence affect the fracture behavior of disordered materials? Further, we revealed that toughness could be significantly enhanced when the size of the heterogeneities becomes of the order of the structural length l_{sys} , even exceeding the toughness of the obstacles. How could this effect be harnessed to improve the mechanical integrity of structures and limit their risk of failure?

APPENDIX

5.A Supplemental Material

Table 5.A.1: Description of variables used in the study.

Symbol	Unit	Description
t	(s)	time
u_i	(m)	displacement field, with $i = \{x, y\}$
ε_{ij}	(-)	infinitesimal strain tensor
σ_{ij}	(Pa)	stress tensor
σ_Y	(Pa)	yield stress
E	(Pa)	Young's modulus
ν	(-)	Poisson's ratio
c_d	(m/s)	dilatational wave speed
c_s	(m/s)	shear wave speed
c_R	(m/s)	Rayleigh wave speed
l	(m)	crack length
w^O	(m)	width of the obstacle stripe
w^M	(m)	width of the matrix stripe
$\Delta l = w^O + w^M$	(m)	period of the micro-structure
$\beta = w^O/\Delta l$	(-)	obstacle density
v	(m/s)	crack speed

Continued on next page

Table 5.A.1 – continued from previous page

Symbol	Unit	Description
v_c	(m/s)	threshold speed causing crack arrest
l_{sys}	(m)	structural length scale
K	(Pa $\sqrt{\text{m}}$)	stress intensity factor
K^{S}	(Pa $\sqrt{\text{m}}$)	static stress intensity factor
G	(J/m ²)	dynamic energy release rate
G^{S}	(J/m ²)	static energy release rate
Γ	(J/m ²)	fracture energy
$\bar{\Gamma}$	(J/m ²)	effective fracture energy
F	(N)	applied force at crack mouth
δ	(m)	crack mouth opening displacement
λ	(m/N)	compliance of the specimen
λ_m	(m/N)	compliance of the loading apparatus
b	(m)	specimen width

5.B Experimental results

Given the crack tip displacement versus time measurements $l(t)$, we compute the speed $v(t)$ by central differences

$$v(l(t) + l(t + \Delta t)/2) = \frac{l(t) + l(t + \Delta t)}{\Delta t}, \quad (5.8)$$

where $\Delta t \approx 4\mu s$ is the time interval between measurements. FIG. 5.B.1 shows the measured crack length, speed and fracture energy for selected experiments.

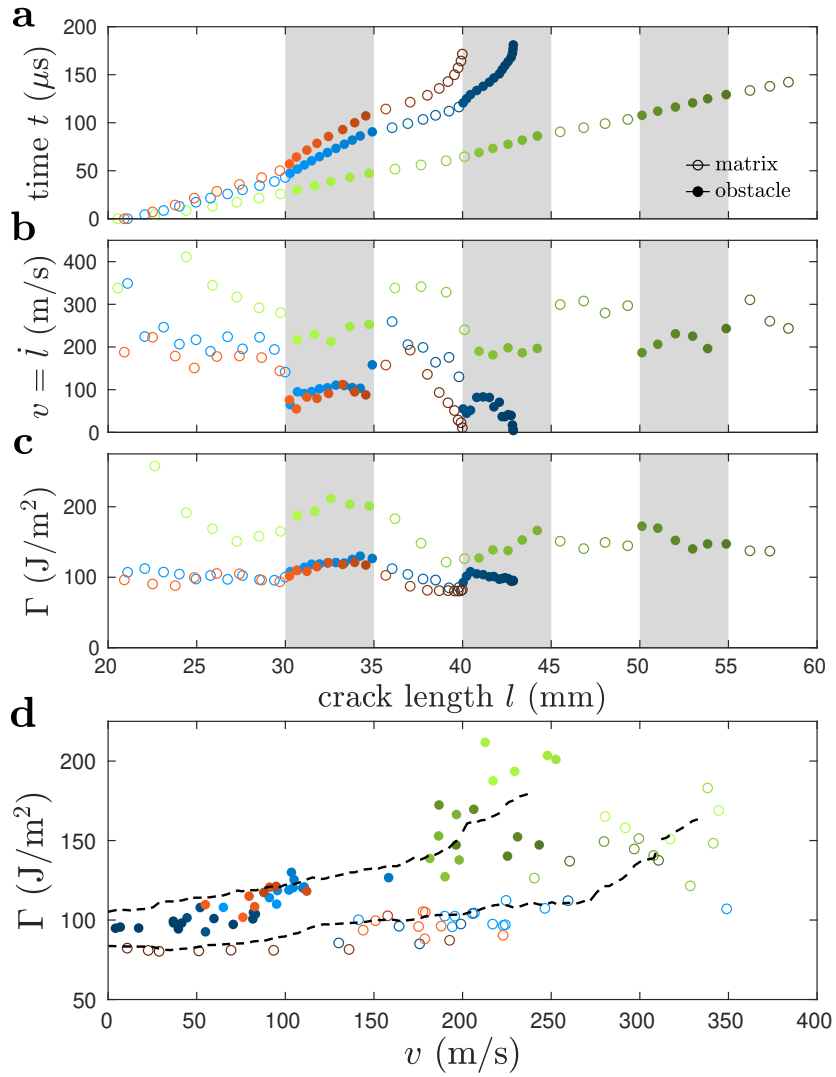


Figure 5.B.1: Supplemental experimental results to FIG. 2. Measurements of crack length vs. time (a) and corresponding crack speed (b) for the same samples as in FIG. 2 and 3. (c) Fracture energy Γ measured by Integrated Digital Image Correlation vs. crack length. (d) $\Gamma(v)$ with average measurements based on 30 heterogeneous and 10 homogeneous samples as black dashed lines. (a,b,c) Gray areas represent obstacles.

5.C Dynamic crack propagation

In our experiments, failure occurs during $\tau_{failure} = l_{sys}/v \simeq 0.1$ ms while the viscous relaxation time typical of the polymers used in this study is ~ 1 s so that an elastic response of the sample can be safely assumed. The relaxation time is measured by applying a small crack mouth opening displacement such that the crack does not propagate and measuring the time over which the load decays. In the present case, the boundaries are far enough from the crack tip so that reflected waves do not affect the dynamics and the infinite medium assumption holds. A theoretical model based on Linear Elastic Fracture Mechanics (LEFM) is thus developed to interpret the experimental observations. The dynamic energy release rate for plane stress configuration is then given by

$$G(l, v, \sigma_{yy}) = \frac{1}{E} K^2(l, v, \sigma_{yy}) A_I(v) \quad (5.9)$$

where the function $A_I(v)$ is a universal function, in the sense that it is independent of applied loading σ_{yy} or geometry, and K is the dynamic stress intensity factor (Freund, 1990). Assuming a semi-infinite crack in an unbounded linear elastic medium subjected to time independent loading, the dynamic stress intensity factor becomes

$$K(l, v, \sigma_{yy}) = k(v) K^S(l, \sigma_{yy}) \quad (5.10)$$

where $k(v) \approx (1 - v/c_R)/\sqrt{1 - v/c_d}$ is another universal function, c_d is the dilatational wave speed and $K^S(l, \sigma_{yy})$ is the stress intensity factor for the equivalent static crack, which depends on geometry and applied loading (Freund, 1990). Thus, the dynamic energy release rate $G(l, v, \sigma_{yy})$ is related to the static energy release rate $G^S(l, \sigma_{yy})$ by

the universal function $g(v)$:

$$G(l, v, \sigma_{yy}) = G^S(l, \sigma_{yy})g(v), \quad (5.11)$$

which can be approximated by $g(v) \approx 1 - v/c_R$ as illustrated in FIG. 5.C.1.

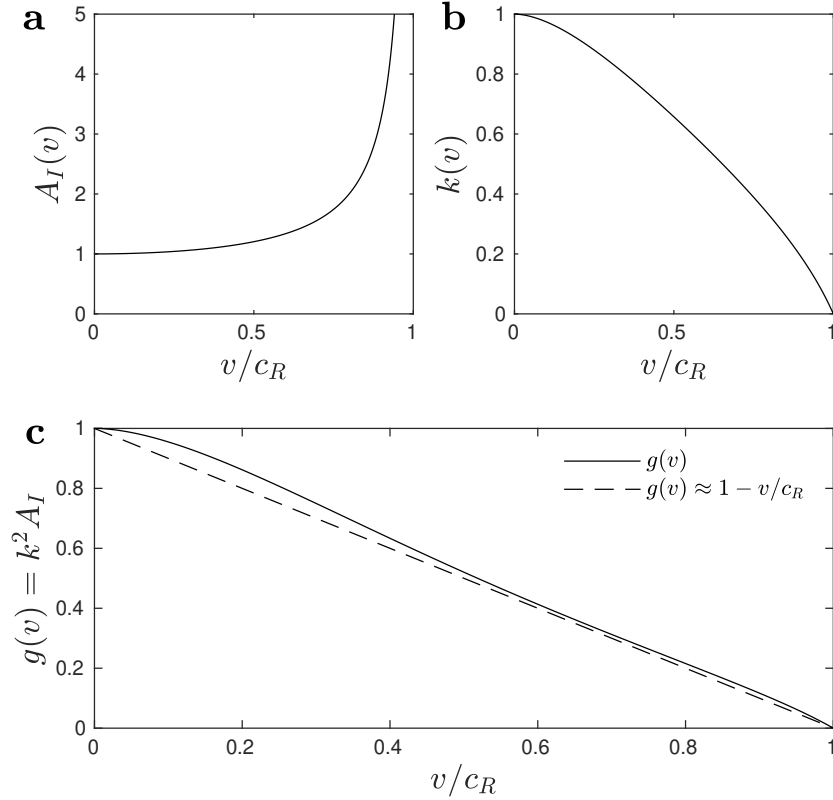


Figure 5.C.1: Universal functions of dynamic fracture mechanics. (a) Experiments are performed at velocities $v < 0.4c_R$ where the contribution of A_I is small. (b, c) Contribution of $k(v)$ is non-negligible for the considered v .

5.D Fracture energy based on dynamic stress intensity factor measurements

The stress intensity factor is measured from the displacement field, which means that the dynamic stress intensity factor $K(l, v, \sigma_{yy})$ can be estimated. The dissipated fracture energy $\Gamma(v) = \frac{K^2}{E} A_I(v)$ is determined from a crack tip energy balance, where $A_I(v)$ accounts for the dynamic contribution of the energy release rate. Rate-dependent processes occurring within the fracture process zone are accounted for by considering a speed dependent fracture energy model for speeds below the micro-branching instability (Scheibert et al., 2010). The fracture energy is related to the surface energy γ^s and the process zone size $l_{pz}(v) = K(l, v)^2 / a\sigma_Y^2 = K^S(l)^2 k(v)^2 / a\sigma_Y^2$

$$\begin{aligned}\Gamma(v) &= \gamma^s + \epsilon l_{pz}(v) \\ &= \gamma^s + \epsilon \frac{K^S(l)^2 k(v)^2}{a\sigma_Y^2} \\ &= \gamma^s + \epsilon \frac{\Gamma(v)/A_I(v)E}{a\sigma_Y^2}\end{aligned}$$

which yields

$$\Gamma(v) = \frac{\gamma^s}{1 - \alpha/A_I(v)},$$

where $\alpha = \epsilon E / (a\sigma_Y^2)$. Setting $\Gamma_0 = \gamma^s / (1 - \alpha)$ one finds

$$\Gamma(v) = \Gamma_0 \frac{1 - \alpha}{1 - \alpha/A_I(v)}, \quad (5.12)$$

where Γ_0 and α are material dependent fitting parameters. Postmortem fracture surfaces are smooth and microcrack branching from the main crack is absent. All experiments

have crack velocities lower than the critical velocity for the micro-branching instability to occur. FIG. 5.D.1 shows the rate-dependent fracture energy for a collection of 30 experiments on homogeneous samples and stripe geometry. From this study, it is found $\Gamma_0^M = 80 \text{ J/m}^2$ for the matrix material and $\Gamma_0^O = 106 \text{ J/m}^2$ for the obstacle, $\alpha = 1.17$ as in Ref. (Scheibert et al., 2010). A_I depends on the elastic properties of the material, which are $E^M \approx 2.8 \pm 0.2 \text{ GPa}$ for the matrix and $E^O \approx 1.9 \pm 0.2 \text{ GPa}$ for the obstacle, $\nu \approx 0.35$ and $\rho \approx 1100 \text{ kg/m}^3$ are identical for both materials. Assuming plane-stress condition one finds $c_R^M \approx 900 \text{ m/s}$ and $c_R^O \approx 730 \text{ m/s}$.

A simplified fracture energy model with linear dependency on v is also introduced

$$\Gamma(v) = \Gamma_0 + \gamma v \quad (5.13)$$

where $\gamma^O \approx 0.22$ and $\gamma^M \approx 0.17$.

5.E Equation of motion of a crack

The equation of motion of a crack is described by energy balance

$$\Gamma(v) = G(l, v, \sigma_{yy}) \quad (5.14)$$

where $\Gamma(v)$ is the energy dissipated by a unit increment in crack length and G is the dynamic energy release rate, given in equation (5.11). Note that v is first order in time meaning that the crack has no inertia. The crack speed adjusts instantaneously to the speed dictated by Γ and G .

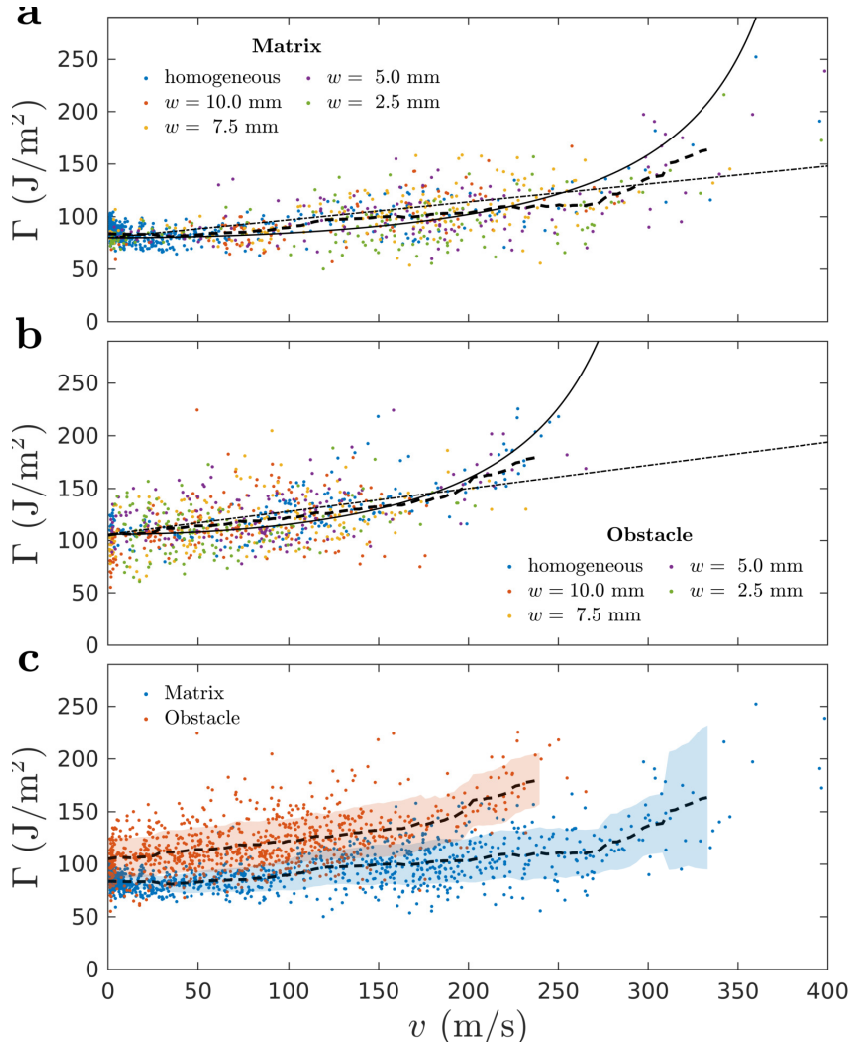


Figure 5.D.1: Measured $\Gamma(v)$ for the matrix (a) and obstacle (b) materials. Measurements on homogeneous samples are reported as well as for stripes geometry with different stripe widths. The dashed line is a moving average over an interval $\Delta v = 25$ m/s. The solid line is the fracture energy model (5.12). The dash-dotted line is the simplified fracture energy model (5.13). (c) Comparison of $\Gamma(v)$ of both materials with error-band corresponding to standard deviation.

For a linear elastic 2D medium the strain energy is $\Omega = \frac{F^2}{2b} \lambda$, where F is the applied force, λ the compliance and $b = 8\text{mm}$ is the specimen width. The static energy release rate becomes

$$G^S = -\frac{\partial\Omega}{\partial l} = \frac{F^2}{2b} \frac{\partial\lambda}{\partial l}. \quad (5.15)$$

For a displacement controlled system and accounting for the compliance of the loading apparatus λ_m , the applied force becomes $F = \delta/(\lambda + \lambda_m)$, where δ is the prescribed displacement. The static energy release rate (5.15) remains unchanged but its rate of change is affected

$$\frac{\partial G^S}{\partial l} = -\frac{F^2}{b} \frac{(\partial\lambda/\partial l)^2}{\lambda + \lambda_m} + \frac{F^2}{2b} \frac{\partial^2\lambda}{\partial l^2}. \quad (5.16)$$

Because the first term in equation (5.16) is always negative, a nonzero λ_m causes a larger $\partial G^S/\partial l$ compared to the case of an infinitely stiff loading stage $\lambda_m = 0$. Thus, λ_m is destabilizing the crack growth. However, $\partial G^S/\partial l < 0$ keeps the crack velocities within the limits prescribed by the image acquisition setup.

The experiments were performed at a constant prescribed displacement rate $\frac{d\delta}{dt} = 25 \text{ mm/s}$. At typical propagation speed of $\sim 100 \text{ m/s}$, the crack breaks the specimen in $\sim 10^{-4} \text{ s}$. The typical loading time to reach the critical energy release rate for the crack to start propagating is $\sim 10^{-1} \text{ s}$, hence the change in δ during propagation is negligible $\sim 0.1\%$. An estimate $\lambda_m \approx 0.75 \text{ } \mu\text{m/N}$ is based on geometry and elastic properties of the pins linking the specimen to the grips. For comparison purposes, the specimen compliance is $\lambda \approx 0.7 \text{ } \mu\text{m/N}$ at initiation ($l = 20 \text{ mm}$) and increases exponentially with crack length, reaching $\lambda \approx 25 \text{ } \mu\text{m/N}$ at $l = 60 \text{ mm}$.

For the tapered double cantilever beam geometry, $\lambda(l)$ is computed by means of finite element simulations, solving the 2D elasticity equations. The geometry is chosen such that the compliance can be approximated by an exponential function

$$\lambda = \frac{\lambda_0}{Eb} e^{l/l_{\text{sys}}}, \quad (5.17)$$

where $\lambda_0 = 3.45$ and $l_{\text{sys}} = 17.5$ mm depend on specimen geometry and $b = 8$ mm is the out-of-plane dimension, which are all kept constant during this study and are found by fitting equation (5.17) to the finite element results.

We use Freund's equation of motion (5.14) to derive the equation describing the speed jump Eq. (2) and for computing the homogenized fracture energy in FIG. 4, where we assumed Eq. (5.17) with $\lambda_m = 0$.

The equation of motion was derived for an elastically homogeneous medium. However, it faithfully capture the experimentally observed velocity jumps without fitting parameters (see FIG. 2c&d). Since G^{S} and $g(v)$ are integral properties, they do not change in a discontinuous way between two nearby points. Therefore the effects of elastic heterogeneity at the interface between two materials are minor: G^{S} is approximately constant and cancels out in Eq. (2) & (3). Furthermore, the difference in $g(v) \approx (1 - v/c_{\text{R}})$ for matrix and obstacle material for $v < 0.4c_{\text{R}}$ is smaller than 8%, which is within the 10% variation observed in FIG. 2c&d. Hence, we use homogenized elasticity when evaluating $g(v)$.

When using the equation of motion to predict the homogenized properties, we perform an integration over the whole period over which material properties vary (see Eq. 5.20).

Thus, homogenized elastic properties can be assumed, as validated by the good agreement between theory and experiments in FIG. 4b.

5.F Trapping and untrapping dynamics

At a material discontinuity, continuity of $G^S(l)$ is ensured, which relates the velocity right before the discontinuity v^- with the velocity immediately after v^+ through

$$G^S = \frac{\Gamma^-(v^-)}{g(v^-)} = \frac{\Gamma^+(v^+)}{g(v^+)}. \quad (5.18)$$

Note that equation (5.18) does not depend on the direction of propagation but only on material properties. Because a sub-Rayleigh crack has no inertia the trapping and untrapping dynamics is symmetric $\frac{\Gamma^O(v^O)}{g(v^O)} = \frac{\Gamma^M(v^M)}{g(v^M)}$.

A simplified model for the speed jumps at the matrix/obstacle interface is derived based on the linear version of rate-dependent fracture energy (5.13). The velocity jump can be found by solving $G^S = \Gamma^M(v^M)/g(v^M) = \Gamma^O(v^O)/g(v^O)$ and assuming an average $\gamma = 0.2$.

$$v^M - v^O \approx \Delta\Gamma_0 \frac{1 - v^M/c_R}{\gamma + \Gamma_0^M/c_R} \quad (5.19)$$

The difference between the simplified model (5.19) and the reference model (5.18) are shown in FIG. 5.F.1a. Additionally, we consider the effect of a rate-independent obstacle ($\alpha^O = 0$), which causes a decrease in jump amplitude (dash dotted line in FIG. 5.F.1a). Conversely, a rate-independent matrix ($\alpha^M = 0$) causes a larger velocity jump (dotted line in FIG. 5.F.1a).

A parametric study is performed on the fracture law parameter α and fracture contrast Γ^O/Γ^M and Young's modulus. It is observed that α is not very sensitive in the range of uncertainty ($\alpha = 1.17 \pm 10\%$) as shown in FIG. 5.F.1.b. Hence, the velocity dependence of the fracture energy is non negligible. FIG. 5.F.1.c shows the effect of fracture energy contrast that shifts the graph horizontally as the contrast increases. Increasing the Young's modulus causes a decrease in v^O as depicted in FIG. 5.F.1.d. The theoretical model is not very sensitive to \bar{E} in its range of uncertainty ($\bar{E} = 2.25 \pm 0.2$ GPa). \bar{E} is the homogenized Young's modulus, which is used to compute c_R . \bar{E} for such a striped composite (with the stripes oriented in the tensile direction) equal to the Reuss bound, which is the harmonic mean of the two moduli: $\bar{E} = (\frac{1}{2E^M} + \frac{1}{2E^O})^{-1}$. From this parametric study it is concluded that fracture contrast is the most important parameter.

5.G Homogenization of fracture energy

The equation of motion of a crack (5.14) is solved numerically assuming $G^S(l) = G_0^S e^{-l/l_{\text{sys}}}$ to find $v(l)$ and the results are integrated to compute the homogenized fracture energy

$$\bar{\Gamma} = \frac{1}{\Delta l} \int_{l_i}^{l_i+\Delta l} \Gamma(v(\tilde{l})) d\tilde{l}, \quad (5.20)$$

where l_i is the location of the start of a matrix phase and $\Delta l = w^O + w^M$. The mean velocity is $\bar{v} = \Delta l / \int_{l_i}^{l_i+\Delta l} v^{-1} dl$.

For vanishing obstacle size with respect to system size $\Delta l/l_{\text{sys}} \rightarrow 0$ we recover a steady-state solution, where G^S is constant over a crack advance Δl . In this case the

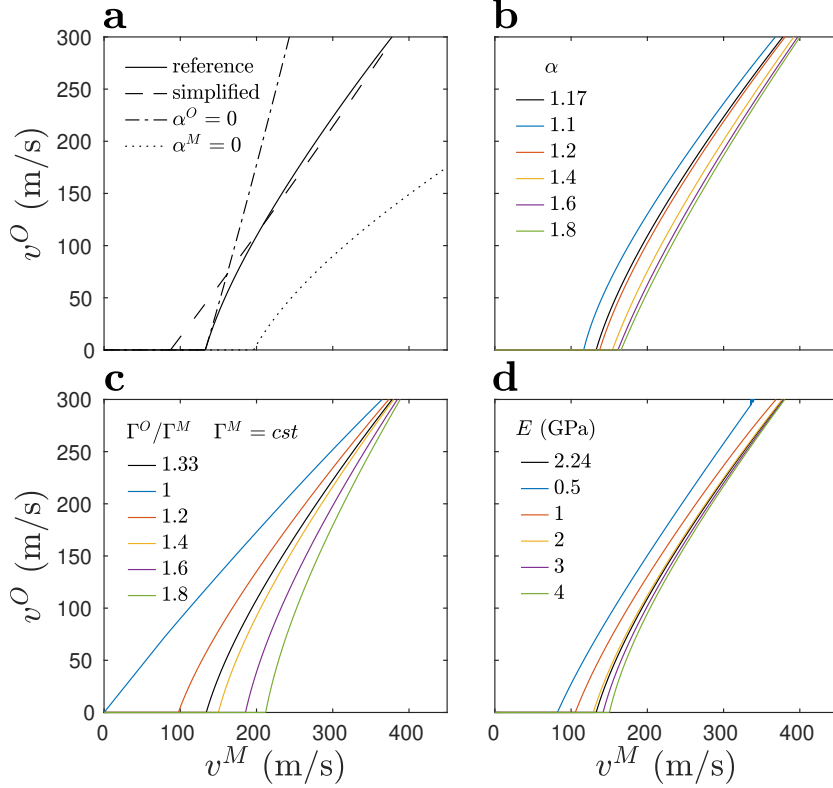


Figure 5.F.1: Trapping and untrapping dynamics assumptions and parametric study. The solid black line is identical throughout the subplots and represents the solution used for comparison with experiments with parameters based on the material characterization (see FIG. 5.D.1). (a) Reference model (5.18) vs. simplified model (5.19) – dashed line. Dash dotted line assumes rate independent obstacle material ($\alpha^O = 0$). Dotted line assumes rate independent matrix material ($\alpha^M = 0$). (b, c, d) Parametric study for a wide range of parameter space well beyond the uncertainties of the measurements.

homogenized fracture energy simply becomes

$$\bar{\Gamma} = \beta\Gamma^O(v^O) + (1 - \beta)\Gamma^M(v^M) \quad (5.21)$$

and the average speed

$$\bar{v} = (\beta/v^O + (1 - \beta)/v^M)^{-1} \quad (5.22)$$

where $w^O = \beta\Delta l$ and $w^M = (1 - \beta)\Delta l$.

5.H Digital Image Correlation analysis

Digital Image Correlation consists in providing an estimate measurement of the displacement field \mathbf{u} at a given time t based on correlating the deformed image $f(\mathbf{x}, t)$ with its reference undeformed image $f(\mathbf{x}, t = 0)$, where \mathbf{x} is the spatial coordinate.

The basic principle is the conservation of gray level

$$f(\mathbf{x}, t = 0) = f(\mathbf{x} + \mathbf{u}, t), \quad (5.23)$$

from which a minimization problem can be set up:

$$\mathbf{u} = \operatorname{argmin} \int_A R(\mathbf{u})^2 d\mathbf{x}, \quad (5.24)$$

where $R(\mathbf{u}) = |f(\mathbf{x}, t = 0) - f(\mathbf{x} + \mathbf{u}, t)|$ is the residual and A the region of interest. In order to find the displacement field \mathbf{u} and inverse problem needs to be solved.

There are multiple approaches for solving the inverse problem, the simplest of which being subdividing the domain in sub-domains A_i and finding \mathbf{u}_i by cross correlation. In the current study different approaches have been used: a global approach and an integrated approach.

Global Approach: A global digital image correlation (Roux and Hild, 2006) involves resolving \mathbf{u} by minimizing $R(\mathbf{u})$ over the whole region of interest. \mathbf{u} is approximated by

$$\mathbf{u}(\mathbf{x}) = \sum \mathbf{u}_i \phi_i(\mathbf{x}) \quad (5.25)$$

where $\phi_i(\mathbf{x})$ are basis functions and \mathbf{u}_i the displacement of each degree of freedom. In order to ensure algorithmic stability, a regularization term which penalizes high gradients

in \mathbf{u} is introduced.

$$\mathbf{u} = \operatorname{argmin} \int_A (R(\mathbf{u})^2 d + \alpha \|\nabla \mathbf{u}\|^2) d\mathbf{x} \quad (5.26)$$

Integrated Approach: The Integrated Digital Image Correlation method (Roux and Hild, 2006; Grabois et al., 2018) uses the analytical solution for a straight crack in an infinite linear elastic medium, known as the Williams eigenfunction expansion $r^{n/2}\psi_n(\theta)$, as basis for the trial displacement field $u = \sum_n a_n^I r^{n/2}\psi_n^I(\theta) + \sum_n a_n^{II} r^{n/2}\psi_n^{II}(\theta)$ (Williams, 1956), where r is the distance from the crack tip and θ the angle with respect to the propagation direction. The superscripts I and II stand for the mode of fracture, I being symmetric with respect to the crack plane and II anti-symmetric. Note that the terms for $n = 0$ are rigid body motions, $n = 1$ represents the singular stress fields and discontinuous displacements across the crack and are related to the stress intensity factor

$$a_1^I = \frac{K^I}{\mu\sqrt{2\pi}}, \quad a_1^{II} = \frac{K^{II}}{\mu\sqrt{2\pi}} \quad (5.27)$$

which in turns is related to the fracture energy by Eq. (5.9). Higher order terms are governed by boundary conditions. Crack velocity is slow enough $v < 0.4c_R$ that the velocity dependence of the angular functions $\psi_n(\theta, v)$ (see Eq. 5.40) can be neglected (Svetlizky and Fineberg, 2014).

The near-tip displacement field can be represented by the first 10 terms of the expansion, which greatly reduces the number of unknowns to be solved for. Thus, there is no need for penalizing high gradients. Also, it automatically accounts for the displacement discontinuity caused by the presence of the crack.

The crack tip position is determined by considering the location along the crack path where the first supersingular term of the Williams expansion $n = -1$ vanishes. This allows for precise measurement of the crack tip position. The amplitudes a_n^I and a_n^{II} are obtained by solving (5.24).

Effect of elastic heterogeneity on IDIC The Williams' expansion assumes that the material elastic properties are homogeneous. The matrix and obstacle material used in the heterogeneous samples differ in Young's modulus by 30%. The IDIC analysis is used to determine the crack tip position and fracture energy. The crack tip position is directly determined by the $u \sim r^{1/2}$ term in the Williams' expansion, which is the dominant term in the displacement field at the tip. Since, the position of the tip does not depend on the amplitude of this term, the elastic heterogeneity does not affect the precision of determining the crack-tip position.

Regarding the fracture energy, we validated the viability of using IDIC on the heterogeneous samples by measurements on homogeneous samples. Our data suggest that effects of elastic heterogeneity of 30% are within the range of variation observed in the homogeneous samples (see FIG. 5.D.1). This can be explained by a homogenization argument, where elasticity near the crack-tip are effectively homogenized within the near tip region where the displacement field $u \sim r^{1/2}$. The size of this region is $\sim 1\text{cm}$ which is larger than the size of the heterogeneity.

Speckle Pattern: For correlating reference and deformed images over the region of interest surrounding the crack tip (Grabois et al., 2018), a speckle pattern was applied on the surface of the specimen using aerosol paint. First, a homogeneous white coating is

applied, followed by a black speckle sprayed from a larger distance. Spline interpolation of the gray-levels across pixels allowed for sub-pixel displacement measurements. The auto-correlation length of the speckle pattern corresponds to 4-6 pixels. The pixel size is 45 μm .

5.I Williams eigenfunctions expansion

Consider a polar coordinate system with origin at the crack tip.

$$x - x_{\text{tip}} + iy = re^{i\theta} \quad (5.28)$$

The displacement field $u = u_x + iu_y$ is a linear combination of the eigenfunctions

$$u = \sum_n a_n^I r^{n/2} \psi_n^I(\theta) + \sum_n a_n^{II} r^{n/2} \psi_n^{II}(\theta) \quad (5.29)$$

where

$$\psi_n^I(\theta) = \frac{1}{2} \left(\kappa e^{i\theta \frac{n}{2}} - \frac{n}{2} e^{i\theta(2-\frac{n}{2})} + (-1)^n e^{-i\theta \frac{n}{2}} + \frac{n}{2} e^{-i\theta \frac{n}{2}} \right) \quad (5.30)$$

$$\psi_n^{II}(\theta) = \frac{i}{2} \left(\kappa e^{i\theta \frac{n}{2}} + \frac{n}{2} e^{i\theta(2-\frac{n}{2})} + (-1)^n e^{-i\theta \frac{n}{2}} - \frac{n}{2} e^{-i\theta \frac{n}{2}} \right) \quad (5.31)$$

where, for plane-stress conditions,

$$\kappa = \frac{3 - \nu}{1 + \nu}, \quad (5.32)$$

with ν the Poisson's ratio.

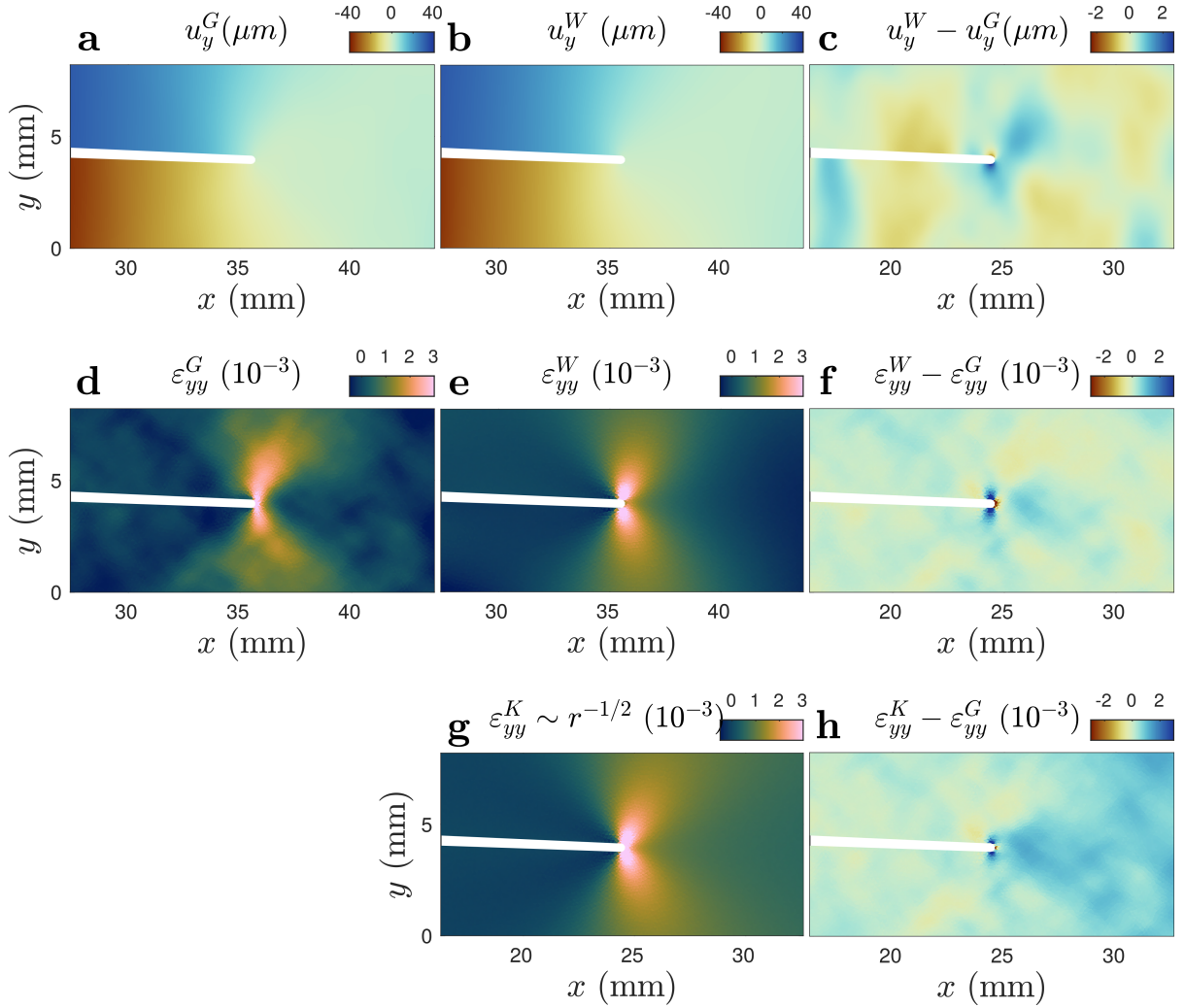


Figure 5.H.1: Digital Image Correlation results. (a) Displacement field u_y measured using the global approach. (b) u_y using integrated approach. (c) Difference in measured displacement between the two methods. (d) Strain field $\varepsilon_{yy} = \partial_y u_y$ computed from the results of the global approach. (e) ε_{yy} from the integrated approach. (f) Difference in strain between the two methods. (g) Singular component of ε_{yy} from the integrated approach. (h) Difference in strain between the global method and the the singular component from the integrated method.

5.I.1 Near tip fields for in-plane dynamic cracks

In the following section we report the solution of the asymptotic near tip fields of a dynamic mode I crack as derived following the procedure in (Freund, 1990).

For a dynamic crack the polar coordinates r, θ are related to the velocity dependent coordinates $r_{d,s}, \theta_{d,s}$ according to

$$\gamma_d = r_d/r = \sqrt{1 - (v \sin \theta / c_d)^2} \quad \gamma_s = r_s/r = \sqrt{1 - (v \sin \theta / c_s)^2} \quad (5.33)$$

$$\tan \theta_d = \alpha_d \tan \theta, \quad \tan \theta_s = \alpha_s \tan \theta, \quad (5.34)$$

where $\alpha_d^2 \equiv 1 - v^2/c_d^2$ and $\alpha_s^2 \equiv 1 - v^2/c_s^2$.

The mode I near tip stress field is

$$\sigma_{ij}(r, \theta) = \sum_n \mu b_n r^{n/2} \Sigma_{ij,n}^I(\theta, v) \quad (5.35)$$

where the asymptotic angular functions $\Sigma_{ij,-1}^I$ are

$$\Sigma_{yy}^I(\theta, v) = -\frac{1}{D(v)} \left[(1 + \alpha_s^2)^2 \gamma_d^{-1/2} \cos(\theta_d/2) - 4\alpha_s \alpha_d \gamma_s^{-1/2} \cos(\theta_s/2) \right] \quad (5.36)$$

$$\Sigma_{xy}^I(\theta, v) = \frac{2\alpha_d(1 + \alpha_s)^2}{D(v)} \left[\gamma_d^{-1/2} \sin(\theta_d/2) - \gamma_s^{-1/2} \sin(\theta_s/2) \right] \quad (5.37)$$

where b_{-1} is related to the stress intensity factor by

$$b_{-1} = \frac{K_I}{\mu \sqrt{2\pi}} \quad (5.38)$$

where

$$D(v) = 4\alpha_s \alpha_d - (1 + \alpha_s^2)^2 \quad (5.39)$$

is the Rayleigh function.

Similarly the mode I displacement field is

$$u_i(r, \theta) = \sum_n b_n r^{1+n/2} \psi_{i,n}^I(\theta, v) \quad (5.40)$$

where the asymptotic angular functions $\psi_{i,-1}(\theta, v)$

$$\psi_{x,-1}^I(\theta, v) = 2 \frac{1}{D(v)} \left[(1 + \alpha_s^2) \gamma_d^{1/2} \cos(\theta_d/2) - 2\alpha_s \alpha_d \gamma_s^{1/2} \cos(\theta_s/2) \right] \quad (5.41)$$

$$\psi_{y,-1}^I(\theta, v) = -2 \frac{\alpha_d}{D(v)} \left[(1 + \alpha_s^2) \gamma_d^{1/2} \sin(\theta_d/2) - 2\gamma_s^{1/2} \sin(\theta_s/2) \right] \quad (5.42)$$

The mode I stress angular functions (see [\(Svetlizky and Fineberg, 2014\)](#) for mode II) consider odd terms $n = -1, 1, 3, 5, \dots$

$$\Sigma_{yy,n}^I(\theta, v) = -\frac{1}{D(v)} \left[(1 + \alpha_s^2)^2 \gamma_d^{n/2} \cos(n\theta_d/2) - 4\alpha_s \alpha_d \gamma_s^{n/2} \cos(n\theta_s/2) \right] \quad (5.43)$$

$$\Sigma_{xy,n}^I(\theta, v) = -\frac{2\alpha_d(1 + \alpha_s)^2}{D(v)} \left[\gamma_d^{n/2} \sin(n\theta_d/2) - \gamma_s^{n/2} \sin(n\theta_s/2) \right] \quad (5.44)$$

CHAPTER 6

CONCLUSION

The objective of this dissertation has been to gain a better understanding of nucleation and dynamic fracture in heterogeneous materials and interfaces. More specifically, we investigated how length scales that describe the spatial extent of the heterogeneity interact with fracture mechanics related length scales to give rise to new properties. We studied dynamic fracture in deterministic systems with inclusions of contrasting elastic properties running parallel to the fracture plane, using a combination of numerical and theoretical methods. We showed that the crack speed can transition to supershear by means of reflected waves at the boundary of the inclusions. We studied nucleation of fracture along interfaces with random local fracture properties using numerical simulations and derived a semi-analytical Monte Carlo model. We showed that the global strength of the interface depends on the spatial correlation of the local fracture energy. Large correlation lengths lead to lower global strength, while small correlation lengths lead to higher global strength with smaller variation. We studied dynamic fracture in deterministic systems with heterogeneous fracture energy using experiments, which revealed that the crack front undergoes abrupt jumps in speed as it enters a material with contrasting fracture energy. We derived an equation describing the crack speed discontinuity as the crack transitions between materials and showed that the rate dependence of fracture energy plays an important role in defining the amplitude of the speed jumps. Additionally, we proposed a homogenization approach for fracture in periodic heterogeneous materials.

We developed an open-source spectral-boundary-integral software, which applies principles of high performance computing. We developed a new three dimensional hybrid method for dynamic rupture problems in complex, heterogeneous unbounded domains, by coupling the finite-element with the spectral-boundary-integral method. This hybrid method is particularly interesting for studying complex systems in a computationally efficient manner, by harnessing the high accuracy of the spectral-boundary-integral method, which serves as a wave absorption algorithm. This method opens the door to a range of new studies which would benefit from the computational savings, such as earthquake cycles and multi-physics fracture processes. Another advantage of the hybrid method is that it could be implemented with any volume based method. For example, if the fracture plane is not known a priori, one could use discretization techniques with embedded discontinuities or a continuum representation of fracture using phase-field methods. Applications of interest are multi-scale models of frictional interfaces, fracture of fiber-reinforced polymers, fracture of concrete with explicit representation of aggregates and cement paste, and debonding of reinforcement bars.

BIBLIOGRAPHY

- Abdelmeguid, M., Ma, X. and Elbanna, A. (2019), ‘A Novel Hybrid Finite Element-Spectral Boundary Integral Scheme for Modeling Earthquake Cycles: Application to Rate and State Faults With Low-Velocity Zones’, *Journal of Geophysical Research: Solid Earth* **124**(12), 12854–12881.
- Aghababaei, R., Warner, D. H. and Molinari, J.-F. (2016), ‘Critical length scale controls adhesive wear mechanisms’, *Nature Communications* **7**, 11816.
- Aki, K. and Richards, P. P. . (2009), *Quantitative Seismology*, 2nd ed. edn, University Science Books, Mill Valley.
- Albertini, G., Elbanna, A. and Kammer, D. S. (2021), ‘A three-dimensional hybrid finite element – spectral boundary integral method for modeling earthquakes in complex unbounded domains’.
- Albertini, G. and Kammer, D. S. (2017), ‘Off-fault heterogeneities promote supershear transition of dynamic mode II cracks’, *Journal of Geophysical Research: Solid Earth* **122**(8), 2017JB014301.
- Allam, A. A. and Ben-Zion, Y. (2012), ‘Seismic velocity structures in the southern California plate-boundary environment from double-difference tomography’, *Geophysical Journal International* **190**(2), 1181–1196.
- Allam, A. A., Ben-Zion, Y., Kurzon, I. and Vernon, F. (2014), ‘Seismic velocity structure in the Hot Springs and Trifurcation areas of the San Jacinto fault zone, California, from double-difference tomography’, *Geophysical Journal International* **198**(2), 978–999.

- Amon, A., Blanc, B. and Géminard, J.-C. (2017), ‘Avalanche precursors in a frictional model’, *Physical Review E* **96**(3), 033004.
- Amontons, G. (1699), ‘De la resistance cause’e dans les machines, tant par let frottements des parties qui les component, que par la roideur des cordes qu’on y employe, et la maniere de calculer l’un et l’autre’, *Memoires de l’Academie Royale A* pp. 275–282.
- Ampuero, J. P. (2002), ‘Etude physique et numerique de la nucleation des seismes’, *PhD Thesis, University of Paris VII, France* .
- Ampuero, J.-P., Ripperger, J. and Mai, P. M. (2006), Properties of Dynamic Earthquake Ruptures With Heterogeneous Stress Drop, *in* ‘Earthquakes: Radiated Energy and the Physics of Faulting’, American Geophysical Union, Washington, DC, pp. 255–261.
- Ampuero, J.-P. and Rubin, A. M. (2008), ‘Earthquake nucleation on rate and state faults – Aging and slip laws’, *Journal of Geophysical Research: Solid Earth* **113**(B1).
- Andrews, D. J. (1976), ‘Rupture velocity of plane strain shear cracks’, *Journal of Geophysical Research* **81**(32), 5679–5687.
- Andrews, D. J. (1985), ‘Dynamic plane-strain shear rupture with a slip-weakening friction law calculated by a boundary integral method’, *Bulletin of the Seismological Society of America* **75**(1), 1–21.
- Andrews, D. J. (1994), ‘Dynamic growth of mixed-mode shear cracks’, *Bulletin of the Seismological Society of America* **84**(4), 1184–1198.
- Archuleta, R. J. (1984), ‘A faulting model for the 1979 Imperial Valley earthquake’, *Journal of Geophysical Research: Solid Earth* **89**(B6), 4559–4585.

- Archuleta, R. J. and Day, S. M. (1980), ‘Dynamic rupture in a layered medium: The 1966 Parkfield earthquake’, *Bulletin of the Seismological Society of America* **70**(3), 671–689.
- Armstrong-Hélouvy, B., Dupont, P. and De Wit, C. C. (1994), ‘A survey of models, analysis tools and compensation methods for the control of machines with friction’, *Automatica* **30**(7), 1083–1138.
- Atkinson, B. K. (1984), ‘Subcritical crack growth in geological materials’, *Journal of Geophysical Research: Solid Earth* **89**(B6), 4077–4114.
- Bai, K. and Ampuero, J.-P. (2017), ‘Effect of Seismogenic Depth and Background Stress on Physical Limits of Earthquake Rupture Across Fault Step Overs: FAULT CRITICAL STEP OVER JUMP DISTANCE’, *Journal of Geophysical Research: Solid Earth* **122**(12), 10,280–10,298.
- Barras, F., Aghababaei, R. and Molinari, J.-F. (2019), ‘Onset of sliding across scales: How the contact topography impacts frictional strength’, *arXiv:1910.11280 [cond-mat, physics:physics]* .
- Barras, F., Kammer, D. S., Geubelle, P. H. and Molinari, J.-F. (2014), ‘A study of frictional contact in dynamic fracture along bimaterial interfaces’, *International Journal of Fracture* **189**(2), 149–162.
- Bar-Sinai, Y., Spatschek, R., Brener, E. A. and Bouchbinder, E. (2014), ‘On the velocity-strengthening behavior of dry friction’, *Journal of Geophysical Research: Solid Earth* **119**(3), 1738–1748.

- Baumberger, T. and Caroli, C. (2006), ‘Solid friction from stick–slip down to pinning and aging’, *Advances in Physics* **55**(3-4), 279–348.
- Bayart, E., Svetlizky, I. and Fineberg, J. (2016), ‘Fracture mechanics determine the lengths of interface ruptures that mediate frictional motion’, *Nature Physics* **12**(2), 166–170.
- Bažant, Z. P. and Li, Y.-N. (1995), ‘Stability of Cohesive Crack Model: Part II—Eigenvalue Analysis of Size Effect on Strength and Ductility of Structures’, *Journal of Applied Mechanics* **62**(4), 965–969.
- Belytschko, T., Liu, W. K., Moran, B. and Elkhodary, K. (2013), *Nonlinear Finite Elements for Continua and Structures*, Wiley.
- Ben-David, O. and Fineberg, J. (2011), ‘Static Friction Coefficient Is Not a Material Constant’, *Physical Review Letters* **106**(25), 254301.
- Ben-Zion, Y. and Huang, Y. (2002), ‘Dynamic rupture on an interface between a compliant fault zone layer and a stiffer surrounding solid’, *Journal of Geophysical Research: Solid Earth* **107**(B2), ESE 6–1.
- Ben-Zion, Y., Peng, Z., Okaya, D., Seeber, L., Armbruster, J. G., Ozer, N., Michael, A. J., Baris, S. and Aktar, M. (2003), ‘A shallow fault-zone structure illuminated by trapped waves in the Karadere–Duzce branch of the North Anatolian Fault, western Turkey’, *Geophysical Journal International* **152**(3), 699–717.

- Benjema, M., Glinsky-Olivier, N., Cruz-Atienza, V. M., Virieux, J. and Piperno, S. (2007), ‘Dynamic non-planar crack rupture by a finite volume method’, *Geophysical Journal International* **171**(1), 271–285.
- Berenger, J.-P. and others (1994), ‘A perfectly matched layer for the absorption of electromagnetic waves’, *Journal of computational physics* **114**(2), 185–200.
- Bernard, P. and Baumont, D. (2005), ‘Shear Mach wave characterization for kinematic fault rupture models with constant supershear rupture velocity’, *Geophysical Journal International* **162**(2), 431–447.
- Beroza, G. C. and Ellsworth, W. L. (1996), ‘Properties of the seismic nucleation phase’, *Tectonophysics* **261**(1), 209–227.
- Bertoldi, K., Reis, P. M., Willshaw, S. and Mullin, T. (2010), ‘Negative Poisson’s Ratio Behavior Induced by an Elastic Instability’, *Advanced Materials* **22**(3), 361–366.
- Bettess, P. (1977), ‘Infinite elements’, *International Journal for Numerical Methods in Engineering* **11**(1), 53–64.
- Bhat, H. S., Dmowska, R., King, G. C. P., Klinger, Y. and Rice, J. R. (2007), ‘Off-fault damage patterns due to supershear ruptures with application to the 2001 Mw 8.1 Kokoxili (Kunlun) Tibet earthquake’, *Journal of Geophysical Research: Solid Earth* **112**(B6), B06301.
- Bilby, B. and Eshelby, J. (1968), Dislocations and theory of fracture, in H. Liebowitz, ed., ‘Fracture, An Advanced Treatise’, Vol. 1, Academic, San Diego, pp. 99–182.

- Bizzarri, A. and Das, S. (2012), ‘Mechanics of 3-D shear cracks between Rayleigh and shear wave rupture speeds’, *Earth and Planetary Science Letters* **357–358**, 397–404.
- Blees, M. K., Barnard, A. W., Rose, P. A., Roberts, S. P., McGill, K. L., Huang, P. Y., Ruyack, A. R., Kevek, J. W., Kobrin, B., Muller, D. A. and McEuen, P. L. (2015), ‘Graphene kirigami’, *Nature* **524**(7564), 204–207.
- Boatwright, J. and Quin, H. (1986), The Seismic Radiation from a 3-D Dynamic Model of a Complex Rupture Process. Part I: Confined Ruptures, *in* ‘Earthquake Source Mechanics’, American Geophysical Union (AGU), pp. 97–109.
- Bonnet, M. and Bui, H. D. (1993), Regularization of the Displacement and Traction BIE for 3D Elastodynamics Using Indirect Methods, *in* J. H. Kane, G. Maier, N. Tosaka and S. N. Atluri, eds, ‘Advances in Boundary Element Techniques’, Springer Series in Computational Mechanics, Springer, Berlin, Heidelberg, pp. 1–29.
- Boore, D. M., Aki, K. and Todd, T. (1971), ‘A two-dimensional moving dislocation model for a strike-slip fault’, *Bulletin of the Seismological Society of America* **61**(1), 177–194.
- Bouchon, M., Toksöz, M. N., Karabulut, H., Bouin, M.-P., Dietrich, M., Aktar, M. and Edie, M. (2002), ‘Space and Time Evolution of Rupture and Faulting during the 1999 İzmit (Turkey) Earthquake’, *Bulletin of the Seismological Society of America* **92**(1), 256–266.
- Bouchon, M. and Vallée, M. (2003), ‘Observation of Long Supershear Rupture During the Magnitude 8.1 Kunlunshan Earthquake’, *Science* **301**(5634), 824–826.

- Bowden, F. P. and Tabor, D. (1950), *The Friction and Lubrification of Solids, vol. 1*, Clarendon Press.
- Breitenfeld, M. S. and Geubelle, P. H. (1998), ‘Numerical analysis of dynamic debonding under 2D in-plane and 3D loading’, *International Journal of Fracture* **93**(1-4), 13–38.
- Brietzke, G. B. and Ben-Zion, Y. (2006), ‘Examining tendencies of in-plane rupture to migrate to material interfaces’, *Geophysical Journal International* **167**(2), 807–819.
- Broberg, K. B. (1989), The near-tip field at high crack velocities, *in* E. S. Folias, ed., ‘Structural Integrity’, Springer Netherlands, pp. 1–13.
- Broberg, K. B. (1999), CRACKS AND FRACTURE, *in* K. B. Broberg, ed., ‘Cracks and Fracture’, Academic Press, San Diego, pp. 753–754.
- Burridge, R. (1973), ‘Admissible speeds for plane-strain self-similar shear cracks with friction but lacking cohesion’, *Geophysical Journal International* **35**(4), 439–455.
- Campillo, M. and Ionescu, I. R. (1997), ‘Initiation of antiplane shear instability under slip dependent friction’, *Journal of Geophysical Research: Solid Earth* **102**(B9), 20363–20371.
- Carlson, J. M. and Langer, J. S. (1989), ‘Properties of earthquakes generated by fault dynamics’, *Physical Review Letters* **62**(22), 2632–2635.
- Carpenter, N. J., Taylor, R. L. and Katona, M. G. (1991), ‘Lagrange constraints for transient finite element surface contact’, *International Journal for Numerical Methods in Engineering* **32**(1), 103–128.

- Chen, C.-T. and Gu, G. X. (2019), ‘Composite Materials: Effect of Constituent Materials on Composite Performance: Exploring Design Strategies via Machine Learning (Adv. Theory Simul. 6/2019)’, *Advanced Theory and Simulations* **2**(6), 1970018.
- Cochard, A. and Madariaga, R. (1994), ‘Dynamic faulting under rate-dependent friction’, *pure and applied geophysics* **142**(3), 419–445.
- Cochran, E. S., Li, Y.-G., Shearer, P. M., Barbot, S., Fialko, Y. and Vidale, J. E. (2009), ‘Seismic and geodetic evidence for extensive, long-lived fault damage zones’, *Geology* **37**(4), 315–318.
- Coulomb, C. (1785), ‘Théorie des machines simples en ayant égard au frottement de leurs parties et à la roideur de leurs cordages’, *Memoires de Mathematique et de Physique de l’Academie Royale* pp. 161–342.
- Courant, R., Friedrichs, K. and Lewy, H. (1928), ‘Über die partiellen Differenzgleichungen der mathematischen Physik’, *Mathematische Annalen* **100**(1), 32–74.
- Cruz-Atienza, V. M., Virieux, J. and Aochi, H. (2007), ‘3D finite-difference dynamic-rupture modeling along nonplanar faults’, *GEOPHYSICS* **72**(5), SM123–SM137.
- Dalguer, L. A. and Day, S. M. (2007), ‘Staggered-grid split-node method for spontaneous rupture simulation’, *Journal of Geophysical Research: Solid Earth* **112**(B2).
- Dansereau, V., Démercy, V., Berthier, E., Weiss, J. and Ponson, L. (2019), ‘Collective Damage Growth Controls Fault Orientation in Quasibrittle Compressive Failure’, *Physical Review Letters* **122**(8), 085501.

- Das, S. (1980), ‘A numerical method for determination of source time functions for general three-dimensional rupture propagation’, *Geophysical Journal International* **62**(3), 591–604.
- Das, S. and Aki, K. (1977), ‘A numerical study of two-dimensional spontaneous rupture propagation’, *Geophysical Journal of the Royal Astronomical Society* **50**(3), 643–668.
- Das, S. and Kostrov, B. V. (1987), ‘On the Numerical Boundary Integral Equation Method for Three-Dimensional Dynamic Shear Crack Problems’, *Journal of Applied Mechanics* **54**(1), 99–104.
- Das, S. and Kostrov, B. V. (1988), ‘An investigation of the complexity of the earthquake source time function using dynamic faulting models’, *Journal of Geophysical Research: Solid Earth* **93**(B7), 8035–8050.
- Day, S. M. (1982), ‘Three-dimensional simulation of spontaneous rupture: The effect of nonuniform prestress’, *Bulletin of the Seismological Society of America* **72**(6A), 1881–1902.
- Day, S. M., Dalguer, L. A., Lapusta, N. and Liu, Y. (2005), ‘Comparison of finite difference and boundary integral solutions to three-dimensional spontaneous rupture’, *Journal of Geophysical Research: Solid Earth* **110**(B12), B12307.
- Dempsey, J. P., Tan, L. and Wang, S. (2010), ‘An isolated cohesive crack in tension’, *Continuum Mechanics and Thermodynamics* **22**(6), 617–634.
- Dieterich, J. H. (1979), ‘Modeling of rock friction: 2. Simulation of preseismic slip’, *Journal of Geophysical Research: Solid Earth* **84**(B5), 2169–2175.

- Dieterich, J. H. (1992), ‘Earthquake nucleation on faults with rate-and state-dependent strength’, *Tectonophysics* **211**(1), 115–134.
- Dieterich, J. H. and Kilgore, B. (1996), ‘Implications of fault constitutive properties for earthquake prediction’, *Proceedings of the National Academy of Sciences* **93**(9), 3787–3794.
- Dieterich, J. H. and Kilgore, B. D. (1994), ‘Direct observation of frictional contacts: New insights for state-dependent properties’, *Pure and Applied Geophysics* **143**(1-3), 283–302.
- Dunham, E. M. (2007), ‘Conditions governing the occurrence of supershear ruptures under slip-weakening friction’, *Journal of Geophysical Research* **112**(B7).
- Dunham, E. M. and Archuleta, R. J. (2004), ‘Evidence for a Supershear Transient during the 2002 Denali Fault Earthquake’, *Bulletin of the Seismological Society of America* **94**(6B), S256–S268.
- Dunham, E. M. and Archuleta, R. J. (2005), ‘Near-source ground motion from steady state dynamic rupture pulses’, *Geophysical Research Letters* **32**(3).
- Dunham, E. M., Favreau, P. and Carlson, J. M. (2003), ‘A Supershear Transition Mechanism for Cracks’, *Science* **299**(5612), 1557–1559.
- Erickson, B. A. and Day, S. M. (2016), ‘Bimaterial effects in an earthquake cycle model using rate-and-state friction’, *Journal of Geophysical Research: Solid Earth* **121**(4), 2480–2506.

- Festa, G. and Vilotte, J.-P. (2006), ‘Influence of the rupture initiation on the intersonic transition: Crack-like versus pulse-like modes’, *Geophysical Research Letters* **33**(15).
- Florijn, B., Coulais, C. and van Hecke, M. (2014), ‘Programmable Mechanical Metamaterials’, *Physical Review Letters* **113**(17), 175503.
- Freund, L. B. (1972), ‘Energy flux into the tip of an extending crack in an elastic solid’, *Journal of Elasticity* **2**(4), 341–349.
- Freund, L. B. (1979), ‘The mechanics of dynamic shear crack propagation’, *Journal of Geophysical Research: Solid Earth* **84**(B5), 2199–2209.
- Freund, L. B. (1990), *Dynamic Fracture Mechanics*, Cambridge University Press, Cambridge.
- Gao, H. and Rice, J. R. (1989), ‘A First-Order Perturbation Analysis of Crack Trapping by Arrays of Obstacles’, *Journal of Applied Mechanics* **56**(4), 828.
- Garagash, D. I. and Germanovich, L. N. (2012), ‘Nucleation and arrest of dynamic slip on a pressurized fault’, *Journal of Geophysical Research: Solid Earth* **117**(B10).
- Geubelle, P. H. and Rice, J. R. (1995), ‘A spectral method for three-dimensional elastodynamic fracture problems’, *Journal of the Mechanics and Physics of Solids* **43**(11), 1791–1824.
- Geus, T. W. J. d., Popović, M., Ji, W., Rosso, A. and Wyart, M. (2019), ‘How collective asperity detachments nucleate slip at frictional interfaces’, *Proceedings of the National Academy of Sciences* **116**(48), 23977–23983.

- Grabois, T. M., Neggers, J., Ponson, L., Hild, F. and Toledo Filho, R. D. (2018), ‘On the validation of integrated DIC with tapered double cantilever beam tests’, *Engineering Fracture Mechanics* **191**, 311–323.
- Greenwood, J. A., Williamson, J. B. P. and Bowden, F. P. (1966), ‘Contact of nominally flat surfaces’, *Proceedings of the Royal Society of London. Series A. Mathematical and Physical Sciences* **295**(1442), 300–319.
- Griffith, A. A. and Taylor, G. I. (1921), ‘VI. The phenomena of rupture and flow in solids’, *Philosophical Transactions of the Royal Society of London. Series A, Containing Papers of a Mathematical or Physical Character* **221**(582-593), 163–198.
- Grigoriu, M. (1995), *Applied non-Gaussian processes: examples, theory, simulation, linear random vibration, and MATLAB solutions*, PTR Prentice Hall, Englewood Cliffs, NJ.
- Hajarolasvadi, S. and Elbanna, A. E. (2017), ‘A new hybrid numerical scheme for modelling elastodynamics in unbounded media with near-source heterogeneities’, *Geophysical Journal International* **211**(2), 851–864.
- Harris, R. A., Archuleta, R. J. and Day, S. M. (1991), ‘Fault steps and the dynamic rupture process: 2-D numerical simulations of a spontaneously propagating shear fracture’, *Geophysical Research Letters* **18**(5), 893–896.
- Harris, R. A. and Day, S. M. (1997), ‘Effects of a low-velocity zone on a dynamic rupture’, *Bulletin of the Seismological Society of America* **87**(5), 1267–1280.

- Hinkle, A. R., Nöhring, W. G., Leute, R., Junge, T. and Pastewka, L. (2020), ‘The emergence of small-scale self-affine surface roughness from deformation’, *Science Advances* **6**(7), eaax0847.
- Hossain, M. Z., Hsueh, C. J., Bourdin, B. and Bhattacharya, K. (2014), ‘Effective toughness of heterogeneous media’, *Journal of the Mechanics and Physics of Solids* **71**(Supplement C), 15–32.
- Hu, F., Xu, J., Zhang, Z. and Chen, X. (2016), ‘Supershear transition mechanism induced by step over geometry’, *Journal of Geophysical Research: Solid Earth* **121**(12), 2016JB013333.
- Huang, Y. and Ampuero, J.-P. (2011), ‘Pulse-like ruptures induced by low-velocity fault zones’, *Journal of Geophysical Research* **116**(B12).
- Huang, Y., Ampuero, J.-P. and Helmberger, D. V. (2014), ‘Earthquake ruptures modulated by waves in damaged fault zones’, *Journal of Geophysical Research: Solid Earth* **119**(4), 2013JB010724.
- Huang, Y., Ampuero, J.-P. and Helmberger, D. V. (2016), ‘The potential for supershear earthquakes in damaged fault zones – theory and observations’, *Earth and Planetary Science Letters* **433**, 109–115.
- Huang, Y. and Gao, H. (2001), ‘Intersonic crack propagation - Part I: The fundamental solution’, *Journal of Applied Mechanics, Transactions ASME* **68**(2), 169–175.
- Huang, Y. and Gao, H. (2002), ‘Intersonic crack propagation - Part II: Suddenly stopping crack’, *Journal of Applied Mechanics, Transactions ASME* **69**(1), 76–80.

- Hyun, S. and Robbins, M. O. (2007), ‘Elastic contact between rough surfaces: Effect of roughness at large and small wavelengths’, *Tribology International* **40**(10), 1413–1422.
- Ida, Y. (1972), ‘Cohesive force across the tip of a longitudinal-shear crack and Griffith’s specific surface energy’, *Journal of Geophysical Research* **77**(20), 3796–3805.
- Israil, A. and Banerjee, P. (1990), ‘Two-dimensional transient wave-propagation problems by time-domain BEM’, *International Journal of Solids and Structures* **26**(8), 851–864.
- Jackson A. P., Vincent Julian F. V., Turner R. M. and Alexander Robert Mcneill (1988), ‘The mechanical design of nacre’, *Proceedings of the Royal Society of London. Series B. Biological Sciences* **234**(1277), 415–440.
- Jiang, C., Yang, Y. and Zheng, Y. (2014), ‘Penetration of mid-crustal low velocity zone across the Kunlun Fault in the NE Tibetan Plateau revealed by ambient noise tomography’, *Earth and Planetary Science Letters* **406**, 81–92.
- Kammer, D. S., Albertini, G. and Ke, C.-Y. (2021), ‘Uguca: a spectral-boundary-integral method for modeling fracture and friction’, *To be published* .
- Kammer, D. S. and McLaskey, G. C. (2019), ‘Fracture energy estimates from large-scale laboratory earthquakes’, *Earth and Planetary Science Letters* **511**, 36–43.
- Kammer, D. S., Radiguet, M., Ampuero, J.-P. and Molinari, J.-F. (2015), ‘Linear Elastic Fracture Mechanics Predicts the Propagation Distance of Frictional Slip’, *Tribology Letters* **57**(3), 1–10.
- Kammer, D. S., Svetlizky, I., Cohen, G. and Fineberg, J. (2018), ‘The equation of motion for supershear frictional rupture fronts’, *Science Advances* **4**(7), eaat5622.

- Kammer, D. S., Yastrebov, V. A., Anciaux, G. and Molinari, J. F. (2014), ‘The existence of a critical length scale in regularised friction’, *Journal of the Mechanics and Physics of Solids* **63**, 40–50.
- Kaneko, Y., Lapusta, N. and Ampuero, J.-P. (2008), ‘Spectral element modeling of spontaneous earthquake rupture on rate and state faults: Effect of velocity-strengthening friction at shallow depths’, *Journal of Geophysical Research: Solid Earth* **113**(B9).
- Ke, C.-Y., McLaskey, G. C. and Kammer, D. S. (2018), ‘Rupture Termination in Laboratory-Generated Earthquakes’, *Geophysical Research Letters* **45**(23), 12,784–12,792.
- Ke, C.-Y., McLaskey, G. C. and Kammer, D. S. (2020), ‘The Earthquake Arrest Zone’, *Geophysical Journal International* .
- Koller, M. G., Bonnet, M. and Madariaga, R. (1992), ‘Modelling of dynamical crack propagation using time-domain boundary integral equations’, *Wave Motion* **16**(4), 339–366.
- Komatitsch, D. and Tromp, J. (1999), ‘Introduction to the spectral element method for three-dimensional seismic wave propagation’, *Geophysical Journal International* **139**(3), 806–822.
- Kozdon, J. E., Dunham, E. M. and Nordström, J. (2013), ‘Simulation of Dynamic Earthquake Ruptures in Complex Geometries Using High-Order Finite Difference Methods’, *Journal of Scientific Computing* **55**(1), 92–124.

- Käser, M. and Dumbser, M. (2006), ‘An arbitrary high-order discontinuous Galerkin method for elastic waves on unstructured meshes — I. The two-dimensional isotropic case with external source terms’, *Geophysical Journal International* **166**(2), 855–877.
- Lapusta, N., Rice, J. R., Ben-Zion, Y. and Zheng, G. (2000), ‘Elastodynamic analysis for slow tectonic loading with spontaneous rupture episodes on faults with rate- and state-dependent friction’, *Journal of Geophysical Research: Solid Earth* **105**(B10), 23765–23789.
- Latour, S., Schubnel, A., Nielsen, S., Madariaga, R. and Vinciguerra, S. (2013), ‘Characterization of nucleation during laboratory earthquakes’, *Geophysical Research Letters* **40**(19), 5064–5069.
- Le Pape, F., Jones, A. G., Vozar, J. and Wenbo, W. (2012), ‘Penetration of crustal melt beyond the Kunlun Fault into northern Tibet’, *Nature Geoscience* **5**(5), 330–335.
- Lebihain, M., Leblond, J.-B. and Ponson, L. (2020), ‘Effective toughness of periodic heterogeneous materials: the effect of out-of-plane excursions of cracks’, *Journal of the Mechanics and Physics of Solids* **137**, 103876.
- Lewis, M. A. and Ben-Zion, Y. (2010), ‘Diversity of fault zone damage and trapping structures in the Parkfield section of the San Andreas Fault from comprehensive analysis of near fault seismograms’, *Geophysical Journal International* **183**(3), 1579–1595.
- Lewis, M. A., Peng, Z., Ben-Zion, Y. and Vernon, F. L. (2005), ‘Shallow seismic trapping structure in the San Jacinto fault zone near Anza, California’, *Geophysical Journal International* **162**(3), 867–881.

- Li, H., Li, S., Song, X. D., Gong, M., Li, X. and Jia, J. (2012), ‘Crustal and uppermost mantle velocity structure beneath northwestern China from seismic ambient noise tomography’, *Geophysical Journal International* **188**(1), 131–143.
- Li, H., Shen, Y., Huang, Z., Li, X., Gong, M., Shi, D., Sandvol, E. and Li, A. (2014), ‘The distribution of the mid-to-lower crustal low-velocity zone beneath the northeastern Tibetan Plateau revealed from ambient noise tomography’, *Journal of Geophysical Research: Solid Earth* **119**(3), 2013JB010374.
- Li, H., Zhu, L. and Yang, H. (2007), ‘High-resolution structures of the Landers fault zone inferred from aftershock waveform data’, *Geophysical Journal International* **171**(3), 1295–1307.
- Li, Q. and Kim, K.-S. (2008), ‘Micromechanics of friction: effects of nanometre-scale roughness’, *Proceedings of the Royal Society A: Mathematical, Physical and Engineering Sciences* **464**(2093), 1319–1343.
- Li, Q., Popov, M., Dimaki, A., Filippov, A. E., Kürschner, S. and Popov, V. L. (2013), ‘Friction Between a Viscoelastic Body and a Rigid Surface with Random Self-Affine Roughness’, *Physical Review Letters* **111**(3), 034301.
- Li, Y.-G., Chen, P., Cochran, E. S., Vidale, J. E. and Burdette, T. (2006), ‘Seismic Evidence for Rock Damage and Healing on the San Andreas Fault Associated with the 2004 M 6.0 Parkfield Earthquake’, *Bulletin of the Seismological Society of America* **96**(4B), S349–S363.

- Li, Y.-G., Vidale, J. E., Day, S. M., Oglesby, D. D. and Team, t. S. F. W. (2002), ‘Study of the 1999 M 7.1 Hector Mine, California, Earthquake Fault Plane by Trapped Waves’, *Bulletin of the Seismological Society of America* **92**(4), 1318–1332.
- Li, Y. N. and Liang, R. Y. (1993), ‘The theory of the boundary eigenvalue problem in the cohesive crack model and its application’, *Journal of the Mechanics and Physics of Solids* **41**(2), 331–350.
- Li, Z., Pastewka, L. and Szlufarska, I. (2018), ‘Chemical aging of large-scale randomly rough frictional contacts’, *Physical Review E* **98**(2), 023001.
- Liu, C., Bizzarri, A. and Das, S. (2014), ‘Progression of spontaneous in-plane shear faults from sub-Rayleigh to compressional wave rupture speeds: Supershear transition of mode II fault’, *Journal of Geophysical Research: Solid Earth* **119**(11), 8331–8345.
- Liu, F. and Borja, R. I. (2009), ‘An extended finite element framework for slow-rate frictional faulting with bulk plasticity and variable friction’, *International Journal for Numerical and Analytical Methods in Geomechanics* **33**(13), 1535–1560.
- Liu, Y. and Lapusta, N. (2008), ‘Transition of mode II cracks from sub-Rayleigh to intersonic speeds in the presence of favorable heterogeneity’, *Journal of the Mechanics and Physics of Solids* **56**(1), 25–50.
- Liu, Y. and Rizzo, F. (1993), ‘Hypersingular boundary integral equations for radiation and scattering of elastic waves in three dimensions’, *Computer Methods in Applied Mechanics and Engineering* **107**(1-2), 131–144.

- Lyashenko, I. A., Pastewka, L. and Persson, B. N. J. (2013), ‘Comment on “Friction Between a Viscoelastic Body and a Rigid Surface with Random Self-Affine Roughness”’, *Physical Review Letters* **111**(18), 189401.
- Lysmer, J. and Kuhlemeyer, R. L. (1969), ‘Finite Dynamic Model For Infinite Media’, *Journal of the Engineering Mechanics Division* **95**(4), 859–878.
- Ma, S. and Archuleta, R. J. (2006), ‘Radiated seismic energy based on dynamic rupture models of faulting’, *Journal of Geophysical Research: Solid Earth* **111**(B5).
- Ma, X. and Elbanna, A. (2015), ‘Effect of off-fault low-velocity elastic inclusions on supershear rupture dynamics’, *Geophysical Journal International* **203**(1), 664–677.
- Ma, X. and Elbanna, A. (2019), ‘Dynamic rupture propagation on fault planes with explicit representation of short branches’, *Earth and Planetary Science Letters* **523**, 115702.
- Ma, X., Hajarolasvadi, S., Albertini, G., Kammer, D. S. and Elbanna, A. E. (2019), ‘A hybrid finite element-spectral boundary integral approach: Applications to dynamic rupture modeling in unbounded domains’, *International Journal for Numerical and Analytical Methods in Geomechanics* **43**(1), 317–338.
- Marone, C. (1998), ‘Laboratory-Derived Friction Laws and Their Application to Seismic Faulting’, *Annual Review of Earth and Planetary Sciences* **26**(1), 643–696.
- McLaskey, G. C. (2019), ‘Earthquake Initiation From Laboratory Observations and Implications for Foreshocks’, *Journal of Geophysical Research: Solid Earth* **124**(12), 12882–12904.

- Mello, M., Bhat, H. S. and Rosakis, A. J. (2016), ‘Spatiotemporal properties of Sub-Rayleigh and supershear rupture velocity fields: Theory and experiments’, *Journal of the Mechanics and Physics of Solids* **93**, 153–181.
- Mizuno, T., Kuwahara, Y., Ito, H. and Nishigami, K. (2008), ‘Spatial Variations in Fault-Zone Structure along the Nojima Fault, Central Japan, as Inferred from Borehole Observations of Fault-Zone Trapped Waves’, *Bulletin of the Seismological Society of America* **98**(2), 558–570.
- Noda, H., Dunham, E. M. and Rice, J. R. (2009), ‘Earthquake ruptures with thermal weakening and the operation of major faults at low overall stress levels’, *Journal of Geophysical Research: Solid Earth* **114**(B7).
- Noda, H., Nakatani, M. and Hori, T. (2013), ‘Large nucleation before large earthquakes is sometimes skipped due to cascade-up—Implications from a rate and state simulation of faults with hierarchical asperities’, *Journal of Geophysical Research: Solid Earth* **118**(6), 2924–2952.
- Okubo, P. G. and Dieterich, J. H. (1984), ‘Effects of physical fault properties on frictional instabilities produced on simulated faults’, *Journal of Geophysical Research: Solid Earth* **89**(B7), 5817–5827.
- Olsen, K. B., Madariaga, R. and Archuleta, R. J. (1997), ‘Three-Dimensional Dynamic Simulation of the 1992 Landers Earthquake’, *Science* **278**(5339), 834–838.

- Palmer, A. C. and Rice, J. R. (1973), ‘The Growth of Slip Surfaces in the Progressive Failure of Over-Consolidated Clay’, *Proceedings of the Royal Society of London A: Mathematical, Physical and Engineering Sciences* **332**(1591), 527–548.
- Passelègue, F. X., Schubnel, A., Nielsen, S., Bhat, H. S. and Madariaga, R. (2013), ‘From Sub-Rayleigh to Supershear Ruptures During Stick-Slip Experiments on Crustal Rocks’, *Science* **340**(6137), 1208–1211.
- Payne, R. M. and Duan, B. (2015), ‘Influence of initial stress and rupture initiation parameters on forbidden zone rupture propagation’, *Geophysical Journal International* **201**(1), 70–77.
- Pei, L., Hyun, S., Molinari, J. F. and Robbins, M. O. (2005), ‘Finite element modeling of elasto-plastic contact between rough surfaces’, *Journal of the Mechanics and Physics of Solids* **53**(11), 2385–2409.
- Pelties, C., Puente, J. d. l., Ampuero, J.-P., Brietzke, G. B. and Käser, M. (2012), ‘Three-dimensional dynamic rupture simulation with a high-order discontinuous Galerkin method on unstructured tetrahedral meshes’, *Journal of Geophysical Research: Solid Earth* **117**(B2).
- Peng, Z., Ben-Zion, Y., Michael, A. J. and Zhu, L. (2003), ‘Quantitative analysis of seismic fault zone waves in the rupture zone of the 1992 Landers, California, earthquake: evidence for a shallow trapping structure’, *Geophysical Journal International* **155**(3), 1021–1041.

- Persson, B. N. J. (2001), ‘Theory of rubber friction and contact mechanics’, *The Journal of Chemical Physics* **115**(8), 3840–3861.
- Pilvelait, T., Dillavou, S. and Rubinstein, S. M. (2020), ‘Influences of microcontact shape on the state of a frictional interface’, *Physical Review Research* **2**(1), 012056.
- Ponson, L. (2009), ‘Depinning Transition in the Failure of Inhomogeneous Brittle Materials’, *Physical Review Letters* **103**(5), 055501.
- Ponson, L. and Pindra, N. (2017), ‘Crack propagation through disordered materials as a depinning transition: A critical test of the theory’, *Physical Review E* **95**(5), 053004.
- Popova, E. and Popov, V. L. (2015), ‘The research works of Coulomb and Amontons and generalized laws of friction’, *Friction* **3**(2), 183–190.
- Puente, J. d. l., Ampuero, J.-P. and Käser, M. (2009), ‘Dynamic rupture modeling on unstructured meshes using a discontinuous Galerkin method’, *Journal of Geophysical Research: Solid Earth* **114**(B10).
- Rabinowicz, E. (1992), ‘Friction coefficients of noble metals over a range of loads’, *Wear* **159**(1), 89–94.
- Rabinowicz, E. (1995), *Friction and wear of materials*, 2nd ed edn, Wiley, New York.
- Ravi-Chandar, K. and Balzano, M. (1988), ‘On the mechanics and mechanisms of crack growth in polymeric materials’, *Engineering Fracture Mechanics* **30**(5), 713–727.

- Ray, S. and Viesca, R. C. (2017), ‘Earthquake Nucleation on Faults With Heterogeneous Frictional Properties, Normal Stress’, *Journal of Geophysical Research: Solid Earth* **122**(10), 8214–8240.
- Ray, S. and Viesca, R. C. (2019), ‘Homogenization of fault frictional properties’, *Geophysical Journal International* **219**(2), 1203–1211.
- Rempe, M., Mitchell, T., Renner, J., Nippress, S., Ben-Zion, Y. and Rockwell, T. (2013), ‘Damage and seismic velocity structure of pulverized rocks near the San Andreas Fault’, *Journal of Geophysical Research: Solid Earth* **118**(6), 2813–2831.
- Rice, J. R. (1978), ‘Thermodynamics of the quasi-static growth of Griffith cracks’, *Journal of the Mechanics and Physics of Solids* **26**(2), 61–78.
- Rice, J. R. (1980), The mechanics of earthquake rupture, in ‘Physics of the Earth’s Interior’, Proceedings of the International School of Physics Enrico Fermi, Course 78, Elsevier, New York, pp. 555–649.
- Rice, J. R. and Ruina, A. L. (1983), ‘Stability of Steady Frictional Slipping’, *Journal of Applied Mechanics* **50**(2), 343–349.
- Richart, N. and Molinari, J.-F. (2015), ‘Implementation of a parallel finite-element library: test case on a non-local continuum damage model’, *Finite Elements in Analysis and Design* **100**, 41–46.
- Ripperger, J., Ampuero, J.-P., Mai, P. M. and Giardini, D. (2007), ‘Earthquake source characteristics from dynamic rupture with constrained stochastic fault stress’, *Journal of Geophysical Research: Solid Earth* **112**(B4).

- Ripperger, J., Mai, P. M. and Ampuero, J.-P. (2008), ‘Variability of Near-Field Ground Motion from Dynamic Earthquake Rupture Simulations’, *Bulletin of the Seismological Society of America* **98**(3), 1207–1228.
- Ritchie, R. O. (2011), ‘The conflicts between strength and toughness’, *Nature Materials* **10**(11), 817.
- Rosakis, A. J., Samudrala, O. and Coker, D. (1999), ‘Cracks Faster than the Shear Wave Speed’, *Science* **284**(5418), 1337–1340.
- Rosakis, A. J. and Zehnder, A. T. (1985), ‘On the dynamic fracture of structural metals’, *International Journal of Fracture* **27**(3-4), 169.
- Roux, S. and Hild, F. (2006), ‘Stress intensity factor measurements from digital image correlation: post-processing and integrated approaches’, *International Journal of Fracture* **140**(1), 141–157.
- Roux, S., Vandembroucq, D. and Hild, F. (2003), ‘Effective toughness of heterogeneous brittle materials’, *European Journal of Mechanics - A/Solids* **22**(5), 743–749.
- Rubin, A. M. and Ampuero, J.-P. (2005), ‘Earthquake nucleation on (aging) rate and state faults’, *Journal of Geophysical Research: Solid Earth* **110**(B11).
- Rubino, V., Rosakis, A. J. and Lapusta, N. (2017), ‘Understanding dynamic friction through spontaneously evolving laboratory earthquakes’, *Nature Communications* **8**(1), 15991.

- Rubinstein, S. M., Cohen, G. and Fineberg, J. (2007), ‘Dynamics of Precursors to Frictional Sliding’, *Physical Review Letters* **98**(22).
- Ruina, A. (1983), ‘Slip instability and state variable friction laws’, *Journal of Geophysical Research: Solid Earth* **88**(B12), 10359–10370.
- Sahli, R., Pallares, G., Ducottet, C., Ali, I. E. B., Akhrass, S. A., Guibert, M. and Scheibert, J. (2018), ‘Evolution of real contact area under shear and the value of static friction of soft materials’, *Proceedings of the National Academy of Sciences* **115**(3), 471–476.
- Savio, D., Pastewka, L. and Gumbsch, P. (2016), ‘Boundary lubrication of heterogeneous surfaces and the onset of cavitation in frictional contacts’, *Science Advances* **2**(3), e1501585.
- Scheibert, J., Guerra, C., Célerié, F., Dalmas, D. and Bonamy, D. (2010), ‘Brittle-Quasibrittle Transition in Dynamic Fracture: An Energetic Signature’, *Physical Review Letters* **104**(4).
- Schär, S., Albertini, G. and Kammer, D. S. (2020), ‘Nucleation of frictional sliding by coalescence of microslip’, *arXiv:2010.04343 [cond-mat]*.
- Sharon, E. and Fineberg, J. (1999), ‘Confirming the continuum theory of dynamic brittle fracture for fast cracks’, *Nature* **397**(6717), 333–335.
- Silverberg, J. L., Evans, A. A., McLeod, L., Hayward, R. C., Hull, T., Santangelo, C. D. and Cohen, I. (2014), ‘Using origami design principles to fold reprogrammable mechanical metamaterials’, *Science* **345**(6197), 647–650.

- Siéfert, E., Reyssat, E., Bico, J. and Roman, B. (2019), ‘Bio-inspired pneumatic shape-morphing elastomers’, *Nature Materials* **18**(1), 24.
- Sokoloff, J. B. (2001), ‘Static Friction between Elastic Solids due to Random Asperities’, *Physical Review Letters* **86**(15), 3312–3315.
- Spencer, N. D. and Tysoe, W. T. (2015), *The cutting edge of tribology: a decade of progress in friction, lubrication, and wear*, World Scientific, [Hackensack], New Jersey.
- Spudich, P. and Cranswick, E. (1984), ‘Direct observation of rupture propagation during the 1979 Imperial Valley earthquake using a short baseline accelerometer array’, *Bulletin of the Seismological Society of America* **74**(6), 2083–2114.
- Svetlizky, I., Albertini, G., Cohen, G., Kammer, D. S. and Fineberg, J. (2020), ‘Dynamic fields at the tip of sub-Rayleigh and supershear frictional rupture fronts’, *Journal of the Mechanics and Physics of Solids* **137**, 103826.
- Svetlizky, I. and Fineberg, J. (2014), ‘Classical shear cracks drive the onset of dry frictional motion’, *Nature* **509**(7499), 205–208.
- Svetlizky, I., Kammer, D. S., Bayart, E., Cohen, G. and Fineberg, J. (2017), ‘Brittle Fracture Theory Predicts the Equation of Motion of Frictional Rupture Fronts’, *Physical Review Letters* **118**(12), 125501.
- Svetlizky, I., Pino Muñoz, D., Radiguet, M., Kammer, D. S., Molinari, J.-F. and Fineberg, J. (2016), ‘Properties of the shear stress peak radiated ahead of rapidly accelerating rupture fronts that mediate frictional slip’, *Proceedings of the National Academy of Sciences* **113**(3), 542–547.

- Tago, J., Cruz-Atienza, V. M., Virieux, J., Etienne, V. and Sánchez-Sesma, F. J. (2012), ‘A 3D hp-adaptive discontinuous Galerkin method for modeling earthquake dynamics’, *Journal of Geophysical Research: Solid Earth* **117**(B9).
- Tape, C., Liu, Q., Maggi, A. and Tromp, J. (2010), ‘Seismic tomography of the southern California crust based on spectral-element and adjoint methods’, *Geophysical Journal International* **180**(1), 433–462.
- Thomas, T. R. (1999), *Rough surfaces*, 2. ed edn, Imperial College Press, London.
- Uenishi, K. and Rice, J. R. (2003), ‘Universal nucleation length for slip-weakening rupture instability under nonuniform fault loading’, *Journal of Geophysical Research: Solid Earth* **108**(B1).
- Vasudevan, A., Grabois, T. M., Cordeiro, G. C., Morel, S., Filho, R. D. T. and Ponson, L. (2021), ‘Adaptation of the tapered double cantilever beam test for the measurement of fracture energy and its variations with crack speed’, *arXiv:2101.04380 [cond-mat]*.
- Virieux, J. and Madariaga, R. (1982), ‘Dynamic faulting studied by a finite difference method’, *Bulletin of the Seismological Society of America* **72**(2), 345–369.
- Wang, D., Mori, J. and Uchide, T. (2012), ‘Supershear rupture on multiple faults for the Mw 8.6 Off Northern Sumatra, Indonesia earthquake of April 11, 2012’, *Geophysical Research Letters* **39**(21), L21307.
- Wang, N. and Xia, S. (2017), ‘Cohesive fracture of elastically heterogeneous materials: An integrative modeling and experimental study’, *Journal of the Mechanics and Physics of Solids* **98**, 87–105.

- Weertman, J. (2014), ‘Transonic gliding edge dislocations/slip pulse near and on an interface/fault’, *Journal of Geophysical Research: Solid Earth* **119**(1), 530–548.
- Weng, H., Huang, J. and Yang, H. (2015), ‘Barrier-induced supershear ruptures on a slip-weakening fault’, *Geophysical Research Letters* **42**(12), 2015GL064281.
- Williams, M. L. (1956), ‘On the Stress Distribution at the Base of a Stationary Crack’, *Journal of Applied Mechanics* **24**, 109–114.
- Xia, K., Rosakis, A. J. and Kanamori, H. (2004), ‘Laboratory earthquakes: The sub-Rayleigh-to-supershear rupture transition’, *Science* **303**(5665), 1859–1861.
- Xu, S., Ben-Zion, Y., Ampuero, J.-P. and Lyakhovskiy, V. (2015), ‘Dynamic Ruptures on a Frictional Interface with Off-Fault Brittle Damage: Feedback Mechanisms and Effects on Slip and Near-Fault Motion’, *Pure and Applied Geophysics* **172**(5), 1243–1267.
- Yang, H. and Zhu, L. (2010), ‘Shallow low-velocity zone of the San Jacinto fault from local earthquake waveform modelling’, *Geophysical Journal International* **183**(1), 421–432.
- Yang, H., Zhu, L. and Cochran, E. S. (2011), ‘Seismic structures of the Calico fault zone inferred from local earthquake travel time modelling’, *Geophysical Journal International* **186**(2), 760–770.
- Yang, Y., Ritzwoller, M. H., Zheng, Y., Shen, W., Levshin, A. L. and Xie, Z. (2012), ‘A synoptic view of the distribution and connectivity of the mid-crustal low velocity zone beneath Tibet’, *Journal of Geophysical Research: Solid Earth* **117**(B4), B04303.

- Yastrebov, V. A., Anciaux, G. and Molinari, J.-F. (2015), ‘From infinitesimal to full contact between rough surfaces: Evolution of the contact area’, *International Journal of Solids and Structures* **52**, 83–102.
- Yin, Z., Hannard, F. and Barthelat, F. (2019), ‘Impact-resistant nacre-like transparent materials’, *Science* **364**(6447), 1260–1263.
- Yue, H., Lay, T., Freymueller, J. T., Ding, K., Rivera, L., Ruppert, N. A. and Koper, K. D. (2013), ‘Supershear rupture of the 5 January 2013 Craig, Alaska (Mw 7.5) earthquake’, *Journal of Geophysical Research: Solid Earth* **118**(11), 2013JB010594.
- Zhan, Z., Helmberger, D. V., Kanamori, H. and Shearer, P. M. (2014), ‘Supershear rupture in a Mw 6.7 aftershock of the 2013 Sea of Okhotsk earthquake’, *Science* **345**(6193), 204–207.
- Zigone, D., Ben-Zion, Y., Campillo, M. and Roux, P. (2015), ‘Seismic Tomography of the Southern California Plate Boundary Region from Noise-Based Rayleigh and Love Waves’, *Pure and Applied Geophysics* **172**(5), 1007–1032.